Development of the Module Back End Electronics for the Large Area Detector of the Enhanced X-ray Timing and Polarimetry Mission

Dissertation

der Mathematisch-Naturwissenschaftlichen Fakultät

der Eberhard Karls Universität Tübingen

zur Erlangung des Grades eines

Doktors der Naturwissenschaften

(Dr. rer. nat.)

vorgelegt von

Hao Xiong

aus Shanxi/China

Tübingen

2025

Gedruckt mit Genehmigung der Mathematisch-Naturwissenschaftlichen Fakultät der Eberhard Karls Universität Tübingen.

Tag der mündlichen Qualifikation:	05.06.2025
Dekan:	Prof. Dr. Thilo Stehle
1. Berichterstatter/-in:	Prof. Dott. Andrea Santangelo
2. Berichterstatter/-in:	Prof. Dr. Yupeng Xu

Kurzfassung

Die Besonderheit der kosmischen Umgebung bietet uns ein unvergleichliches Experimentallabor zur Untersuchung des Materiezustands unter extremen Bedingungen wie extrem hohen Dichten, extrem starken Gravitationsfeldern und extrem starken Magnetfeldern. Unter diesen extremen Bedingungen treten verschiedene komplexe physikalische Prozesse auf, die mit der Erzeugung hochenergetischer Strahlung einhergehen. Diese Strahlung ist zu einem wichtigen Medium zur Erforschung des Materiezustands und seiner Entwicklungsmechanismen unter extremen Bedingungen geworden. Röntgenstrahlen (elektromagnetische Strahlung mit einer Energie von etwa 100 eV bis 100 keV) sind ein wichtiger Bestandteil der kosmischen Strahlung und kommen in verschiedenen hochenergetischen Himmelsumgebungen weit verbreitet vor. Am Endpunkt der Sternentwicklung entstehen kompakte Objekte. Abhängig von der anfänglichen Masse kann sich ein Stern zu einem Weißen Zwerg, einem Neutronenstern oder einem Schwarzen Loch entwickeln. Diese kompakten Himmelskörper und die von ihnen gebildeten Systeme (wie Doppelsternsysteme) oder ihre Umgebung zeichnen sich durch extrem hohe Materiedichten, extrem starke Gravitationsfelder und Magnetfelder aus, in denen intensive Energieaustausch- und physikalische Prozesse ablaufen, die üblicherweise mit einer starken Röntgenstrahlung verbunden sind. In diesen extremen Umgebungen können einige physikalische Phänomene und Wechselwirkungen nicht nur die Quelle der Röntgenstrahlung sein, sondern auch die Ausbreitungseigenschaften der Röntgenstrahlen beeinflussen. Durch die präzise Detektion des Energiespektrums, der Zeitcharakteristika, der Positionsinformationen und der Polarisationsinformationen von Röntgenstrahlen können physikalische Mechanismen unter extremen Bedingungen erschlossen und rekonstruiert werden, wodurch ein tieferes Verständnis hochenergetischer astrophysikalischer Prozesse ermöglicht wird. Dies erlaubt uns, mehr über den Ursprung, die Eigenschaften und die Entwicklung des Universums zu erfahren. Die Erdatmosphäre absorbiert den größten Teil der eintreffenden Röntgenstrahlung, weshalb deren Detektion auf Weltraumobservatorien angewiesen ist. Dies macht die Röntgenastronomie zu einem bedeutenden Forschungsfeld der Astronomie.

Die Enhanced X-ray Timing and Polarimetry (eXTP)-Mission ist eine neue Generation von Röntgenobservatorien, die vom Institut für Hochenergiephysik der Chinesischen Akademie der Wissenschaften geleitet und von chinesischen und europäischen Wissenschaftlern vorangetrieben wird. In ihrer ursprünglichen Konfiguration bietet sie mit vier wissenschaftlichen Nutzlasten einzigartige Eigenschaften im Vergleich zu anderen aktiven Röntgenobservatorien. Das Spectroscopic Focusing Array (SFA) und der Large Area Detector (LAD) bilden zusammen ein Röntgen-Zeit-Spektrometer für den Energie-

bereich von 0,5 keV bis 30 keV, wobei der LAD auf einen Energiedynamikbereich von bis zu 80 keV erweitert werden kann. Das Polarimetry Focusing Array (PFA) ist für die Messung der Röntgenpolarisation ausgelegt, während der Wide Field Monitor (WFM) als Überwachungslast mit großem Sichtfeld dazu dient, interessante Beobachtungsobjekte zu entdecken und Trigger-Signale für nachfolgende Beobachtungen der drei vorgenannten Nutzlasten bereitzustellen.

Als Zeit-Spektrometer für den Energiebereich von 2 bis 30 keV zeichnet sich der LAD durch eine große effektive Detektionsfläche, eine hohe Energieauflösung und eine hohe Zeitauflösung aus. Die Verwirklichung dieser Leistungsmerkmale hängt von der koordinierten Arbeit von 640 großflächigen, mehrkanaligen Silizium-Driftdetektoren ab, von denen jeder 224 Anoden enthält. Um eine so große Anzahl von Detektoren effizient zu verwalten und die Signale aus so vielen Anodenkanälen geordnet auszulesen, setzt der LAD auf ein modulares Detektionskonzept und eine hierarchische digitale Schaltungsarchitektur, um die Stabilität und Bedienbarkeit des Systems zu verbessern. Jedes Detektionsmodul enthält 16 großflächige, mehrkanalige Silizium-Driftdetektoren, die jeweils mit einer speziellen Front-End-Elektronik (FEE) integriert sind. Zwei identische FPGA-basierte digitale Schaltungen, die als Module Back-End Electronics (MBEE) bezeichnet werden, sind als erste digitale Verarbeitungsstufe im Detektionsmodul verbaut. Jeweils zehn Detektionsmodule sind mit einer Panel Back-End Electronics (PBEE) verbunden, die die zweite digitale Verarbeitungsstufe bildet. Der LAD besteht aus vier PBEEs und den zugehörigen 40 Detektionsmodulen, die zentral von der Instrument Control Unit (ICU) verwaltet und gesteuert werden.

Das Thema dieser Arbeit ist die Entwicklung des MBEE, einschließlich der Hardware- und FPGA-Programmgestaltung und -Implementierung. Die Hardware-Entwicklung umfasst das Schaltungsdesign, die Auswahl der Chips, die Topologieplanung der Leiterplatte (PCB), die Layout- und Routing-Strategie sowie die Fertigung. Gleichzeitig ist das MBEE als zentrales Steuerelement der Modulelektronik für die Steuerung, Konfiguration und Überwachung des Detektionsmoduls verantwortlich, registriert die Ankunftszeit der Röntgenstrahlen und rekonstruiert die Energie der Röntgenphotonen auf Basis der digitalisierten Signaldaten. Die Umsetzung dieser Funktionen ist untrennbar mit der Gestaltung des FPGA-Programms verbunden. Das MBEE-Programm wird entsprechend den Aufgabenanforderungen in bestimmten Betriebsmodi entwickelt. Der Betrieb des MBEE basiert auf der Dekodierung der Telecommands, die von der PBEE gesendet werden, um Aufgaben wie das Umschalten der Betriebsmodi, das Abrufen von Betriebsdaten und das Anpassen der Parameter der Modulelektronik durchzuführen. Diese Arbeit beschreibt den Implementierungsprozess dieser Operationen im Detail. Im Beobachtungsmodus ist das MBEE für die Verarbeitung der digitalisierten Signale aus den FEEs zuständig, um Röntgenereignisse aufzuzeichnen und zu rekonstruieren. Basierend auf dem Pipeline-Konzept führt es in einer sequenziellen Verarbeitungskette eine Pedestal-Subtraktion, eine Subtraktion des gemeinsamen Modus-Rauschens, eine Energiewiederherstellung, eine Energiediskriminierung und die Generierung wissenschaftlicher Datenpakete durch, um die Ankunftszeit und die Energieinformationen der Röntgenstrahlen zu extrahieren.

Um die Schnittstellen des MBEE in der frühen Entwicklungsphase besser zu messen und zu verifizieren, wurden der PBEE-Simulator, der MPSU-Simulator und der FEE-Simulator entwickelt, um eine vollständige Detektionskette vorläufig aufzubauen. Besonders kritisch ist dabei der FEE-Simulator, der nicht nur für Schnittstellentests genutzt wird, sondern auch die Entwicklung der Datenverarbeitungspipeline in dieser frühen Phase unterstützt. Der FEE-Simulator und eine zugehörige grafische Benutzeroberfläche können die Energiedistribution auf den Anodenkanälen simulieren, nachdem eine Detektorhälfte ein Röntgenphoton mit einer bestimmten Energie an einer bestimmten Einfallsposition absorbiert hat, und das digitale Ausgangssignal nach der Energieablagerung, Ladungsumwandlung im Detektor, Verstärkung und Analog-Digital-Wandlung in der FEE darstellen. Basierend auf den Schnittstellen und Ausgaben des FEE-Simulators werden Rohdaten für die Entwicklung der Datenverarbeitungspipeline bereitgestellt. Die Arbeit beschreibt die ersten Funktionstests des MBEE sowie die Testergebnisse der auf dem MBEE und diesen Simulatoren aufgebauten Detektionskette. Die Tests zeigen, dass das MBEE die Steuerung, Konfiguration und Zustandsüberwachung der Modulelektronik realisieren und erfolgreich die Zeit extrahieren sowie die Energie der Röntgenereignisse rekonstruieren kann, die vom FEE-Simulator erzeugt werden. Damit wird die Wirksamkeit der Kernfunktionen des MBEE verifiziert.

Abstract

The particularity of the cosmic environment provides us with an unparalleled experimental laboratory for studying the state of matter under extreme conditions such as extremely high densities, extremely strong gravities, and extremely strong magnetic fields. Under these extreme conditions, various complex physical processes occur, accompanied by the generation of high-energy radiation. This radiation has become an important medium for exploring the state of matter and its evolution mechanism under extreme conditions. X-rays (electromagnetic radiation with energy from around 100 eV to around 100 keV) are an important component of cosmic radiation and are widely present in various high-energy celestial environments. At the endpoints of stellar evolution, compact objects are formed. Depending on the initial mass, a star may evolve into a white dwarf, a neutron star, or a black hole. These compact celestial bodies and the systems they form (such as binary star systems) or their surrounding environments are characterized by extremely high material densities, extremely strong gravities, and magnetic fields, where intense energy exchange and physical processes occur, usually accompanied by strong X-ray radiation. In these extreme environments, some physical phenomena and interactions may not only become the source of X-rays but also affect the propagation characteristics of X-rays. By accurately detecting the energy spectrum, time characteristics, position information, and polarization information of X-rays, physical mechanisms under extreme conditions can be inferred and inverted, thereby gaining a deeper understanding of high-energy astrophysical processes, enabling us to understand more about the origin, features, and evolution of the Universe. The Earth's atmosphere absorbs most of the incident X-rays, so the detection of X-rays must rely on the space observatory. This makes X-ray astronomical observations an important field in astronomical research.

The enhanced X-ray Timing and Polarimetry (eXTP) mission is a new generation of X-ray observatories, led by the Institute of High Energy Physics of the Chinese Academy of Sciences and promoted by Chinese and European scientists. In its original configuration, four scientific payloads provide unique characteristics compared to other operating X-ray observatories. The Spectroscopic Focusing Array (SFA) and the Large Area Detector (LAD) together constitute an X-ray timing spectrometer from 0.5 keV to 30 keV, of which the LAD can be extended to an energy dynamic range of up to 80 keV. The Polarimetry Focusing Array (PFA) is designed for X-ray polarization measurement, while the Wide Field Monitor (WFM), a survey payload with a wide field of view, is used to discover observation sources of interest and provide trigger signals for subsequent observations of the above three payloads.

As a timing spectrometer covering the energy from 2 to 30 keV X-rays, the LAD has

the characteristics of a large effective detection area, a good energy resolution, and a good time resolution. The realization of these performances depends on the coordinated work of 640 large area multi-channel silicon drift detectors, each of which contains 224 anodes. In order to efficiently manage such a large number of detectors and read out the signals from so many anode channels in an orderly manner, the LAD adopts a modular detection concept and a hierarchical digital circuit architecture to improve the stability and operability of the system. Each detection module contains 16 large area multi-channel silicon drift detectors, and each detector is integrated with a dedicated Front End Electronics (FEE). Two identical FPGA-based digital circuits — Module Back-End Electronics (MBEEs), are assembled in the detector module as the first-level digital circuit. Every 10 detection modules are connected to a Panel Back-End Electronics (PBEE), which is the second-level digital circuit. The LAD consists of 4 PBEEs and their corresponding 40 detection modules and is uniformly managed and controlled by the Instrument Control Unit (ICU).

The topic of this thesis is to present the development process of the MBEE, including the hardware and FPGA program design and implementation. In terms of hardware design, it includes circuit structure design, chip selection, Printed Circuit Board (PCB) topology planning, layout and routing strategy, and manufacturing. As the hub of the module electronics, the MBEE is responsible for controlling, configuring, and monitoring the detection module, recording the arrival time of the X-ray, and reconstructing the energy of the X-ray photon based on the data of the digitized signal. The realization of these functions is inseparable from the design of the FPGA program. The MBEE's program is developed for task requirements in specific operation modes. The operation of the MBEE depends on the decoding of the telecommand sent by the PBEE to complete tasks such as switching operation modes, obtaining housekeeping data, and adjusting the parameters of the module electronics. This thesis describes the implementation process of these operations in detail. In observation mode, the MBEE is responsible for processing the digitized signals from the FEEs to record and reconstruct the X-ray event. Based on the concept of the pipeline, it performs pedestal subtraction, common mode noise subtraction, energy reconstruction, energy discrimination, and science data packet generation in sequence to get the X-ray arrival time and energy information.

In order to better measure and verify the circuit interfaces of the MBEE in the early phase of development, the PBEE simulator, MPSU simulator, and FEE simulator were designed to preliminarily build a complete detection chain. Among them, the FEE simulator is particularly critical, not only for interface testing but also to provide support for the development of the data processing pipeline in this early phase. The FEE simulator with a Graphical User Interface can simulate the distribution of the energy on the anode channels after a single detector half receives an X-ray photon with a certain energy in a certain incident position, and present the digital output after the energy deposition, charge conversion on the detector, the amplification and analog-to-digital conversion on the FEE. Based on the interface and output of the FEE simulator, raw data for the development of the data processing pipeline are provided. The thesis describes the preliminary

functional tests of the MBEE and the test results of the detection chain built based on the MBEE and these simulators. The tests show that the MBEE can realize the controlling, configuration, and status monitoring of the module electronics, and successfully extract the time and reconstruct the energy of the X-ray event generated by the FEE simulator, verifying the effectiveness of the MBEE core functions.

Contents

Chapter 1

Introduction

The enhanced X-ray Timing and Polarimetry (eXTP) mission (Zhang *et al.*, 2017, 2019; Santangelo *et al.*, 2022) is a large innovative observatory in the field of X-ray astronomy, derived from China's XTP (X-ray Timing and Polarimetry) mission and Europe's LOFT (Large Observatory for X-ray Timing) mission (Feroci *et al.*, 2016). The eXTP mission is developed by an international cooperation group led by the Institute of High Energy Physics (IHEP) of the Chinese Academy of Sciences (CAS).

The eXTP mission in its original configuration features four primary payloads, including Spectroscopic Focusing Array (SFA), Polarimetry Focusing Array (PFA), Wide Field Monitor (WFM), and Large Area Detector (LAD) (Feroci *et al.*, 2018). The LAD is a spectral-timing instrument designed specifically to observe X-rays in the energy range from 2 to 30 keV based on the large area multi-channel Silicon Drift Detector (SDD). The large effective detection area requires a significant number of detectors and the integration of the electronic readout systems.

To address these technical challenges, a modular detection concept is applied in the LAD (Xiong *et al.*, 2022). The fundamental unit of the LAD is the detection module, each of which contains sixteen large area multi-channel SDDs and sixteen Front-End Electronics (FEEs) that interface with the two identical Module Back-End Electronics (MBEEs). The FEE amplifies and digitizes the current signals generated by the interaction of X-rays with the detector, while the MBEE is responsible for extracting timing information and reconstructing the X-ray photon's energy by processing the digitized signal. This thesis details the design and implementation of the MBEE hardware, as well as the development of the Very High-Speed Integrated Circuit Hardware Description Language (VHDL)-based Field-Programmable Gate Array (FPGA) program. Additionally, an FEE simulator consisting of an evaluation board with a Graphical User Interface (GUI) and a Module Power Supply Unit (MPSU) simulator are presented for joint testing of the detection chain.

The thesis is organized into six chapters. Chapter 1 begins by introducing the generation of X-ray radiation and detection principles, specifically emphasizing the critical information to be obtained from X-ray detection, that is, energy, timing, imaging, and polarization.

In Chapter 2, the scientific objectives of the eXTP mission are outlined, accompanied

by a detailed discussion of the mission's features and its advantages over other X-ray observatories that aim to achieve similar research goals. This chapter will also describe the specific roles of the four payloads — the SFA, the PFA, the WFM (Ceraudo *et al.*, 2024b), and the LAD, and their contributions to the detection of X-rays in the eXTP mission. Additionally, a brief overview of the US-based Spectroscopic Time-Resolving Observatory for Broadband Energy X-rays (STROBE-X) mission (Ray *et al.*, 2024) will be provided. The STROBE-X mission is also equipped with two payloads, the WFM and LAD, whose functions are the same as those in the eXTP mission, and incorporates some of the electronics from the eXTP mission payloads.

In Chapter 3, a detailed description of the LAD payload is presented, focusing on its target performance and structure as a highly time-resolved spectrometer designed for observing relatively hard X-rays. The chapter will also provide a comprehensive description of the detection chain based on the detector module, along with a detailed presentation of the hierarchical structure of the LAD electronics, consisting of FEE, MBEE, Panel Back-End Electronics (PBEE), Instrument Control Unit (ICU), and MPSU of the detection module. We focus on large area multi-channel SDD and FEE, especially on the key elements of this detector and the FEE that need to be considered when designing the FEE simulator.

The design of the MBEE hardware, with a particular emphasis on the interfaces between the MBEE and other circuits, will be discussed in Chapter 4. The application of radiation-hardened chips based on European technology is a highlight of the MBEE design. Additionally, the design and implementation of the FPGA program will be thoroughly explained. Finally, preliminary tests have been conducted to verify the fundamental functionality of both the MBEE hardware and its associated programs.

The FEE, PBEE, and MPSU, or their simulators, are crucial for testing the interfaces between the MBEE and these circuits. In addition, the MBEE is the key circuit responsible for extracting timing information and reconstructing the energy of the X-ray event from the digitized signals. A complete detection chain is required to test its function and performance thoroughly. As such, Chapter 5 will focus on the design and implementation of these simulators, establishing the necessary hardware foundation for testing the MBEE interfaces and detection chain. This will pave the way for the joint testing of the detection system. We also present the energy reconstruction process using the detection chain based on the MBEE and the simulators.

1.1 X-ray Radiation in Astronomy

X-rays are electromagnetic waves with extremely short wavelengths, typically ranging from 0.01 to 10 nm, corresponding to an energy range of 100 eV to 100 keV, although the upper limit is somewhat arbitrary. In the electromagnetic spectrum, X-rays are located between UV (Ultraviolet) rays and gamma rays. X-rays possess strong penetrating power, however, the photons of the X-rays are subject to absorption and scattering during

the interaction with the atmosphere. The Earth's atmosphere is almost opaque to X-rays originating from the universe, therefore, only an extremely small fraction of X-rays from the universe will penetrate the Earth's atmosphere and enter the Earth's surface, so X-ray detection relying on space-based satellites has become an important and unique part of cosmic radiation detection. In this section, we will introduce several X-ray sources in the field of astronomical research based on (Seward and Charles, 2010; Rybicki and Lightman, 2024; Longair, 2011; Arnaud *et al.*, 2011; Knoll, 2010). X-ray sources in astronomy are often associated with high-energy processes and extreme environments such as extreme conditions of densities, gravities, and magnetic fields. These sources provide valuable information about the universe.

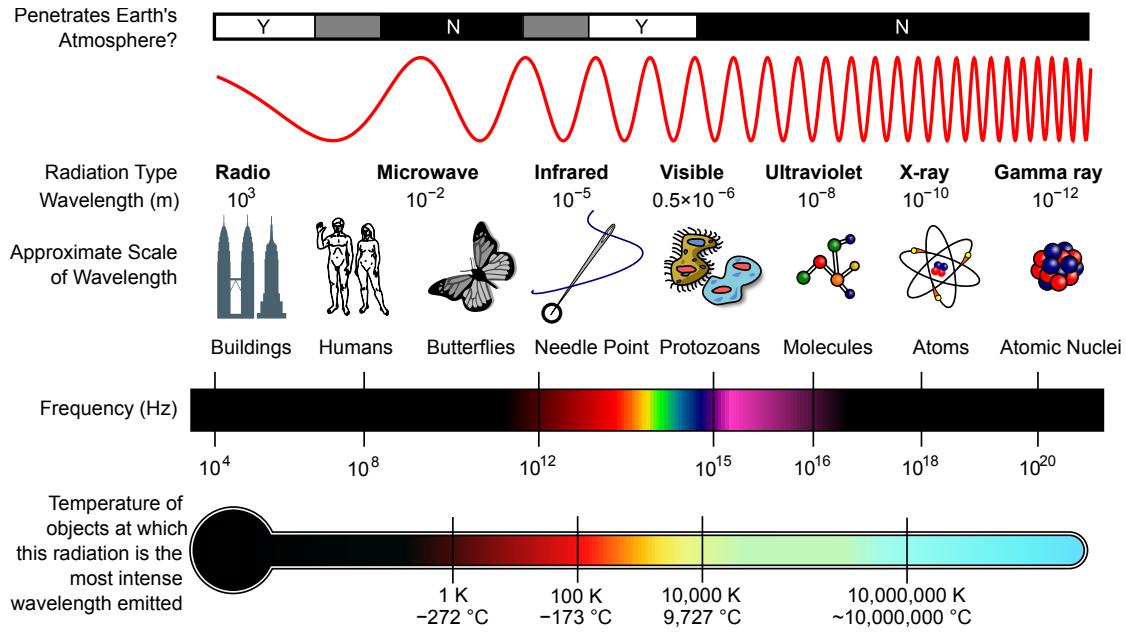

Figure 1.1: Properties of the electromagnetic spectrum. (Inductiveload and NASA, 2007)

1.1.1 Thermal Radiation

High-temperature objects are characterized by radiation in equilibrium in the form of blackbody radiation. Blackbody radiation is the electromagnetic radiation emitted by a blackbody in thermodynamic equilibrium. The continuous spectrum of blackbody radiation depends on the temperature of the blackbody and is described by Planck's law, as shown in Equation (1.1):

$$I(\nu,T) = \frac{2h\nu^3}{c^2} \cdot \frac{1}{\exp\left(\frac{h\nu}{kT}\right) - 1} \tag{1.1}$$

where $I(\nu,T)$ is the radiation intensity, ν is the electromagnetic wave frequency, T is the blackbody temperature, h is Planck constant, k is Boltzmann constant and c is light speed. As shown in Figure 1.2, it can be seen that as the temperature increases, the peak of the radiation spectrum will move towards a smaller wavelength. Wien's displacement law reveals the relationship between the peak position and temperature more precisely, as shown in Equation (1.2):

$$\lambda_{\max} = \frac{b}{T} \tag{1.2}$$

where b is Wien's displacement constant, whose value is $2.8977 \times 10^{-3}\,\mathrm{m{\cdot}K}$.

When the blackbody temperature exceeds 10^6 K, the energy of electromagnetic radiation is primarily concentrated in the X-ray band (Tucker, 1975).

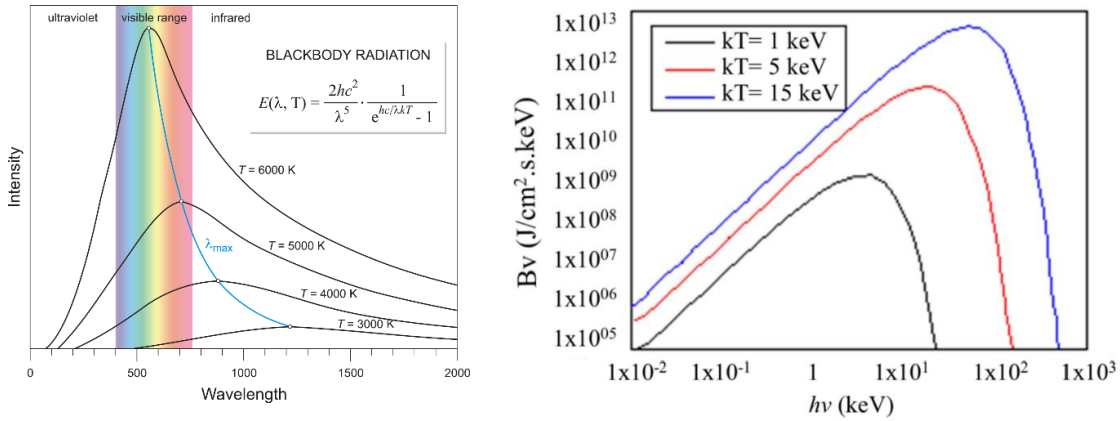

Figure 1.2: Left (Kule, 2010) shows the blackbody radiation spectrum at different temperatures. With increasing temperature, the spectral peak shifts progressively toward shorter wavelengths (higher frequencies). Right (Wang *et al.*, 2021) shows that the energy range of blackbody radiation is concentrated in the X-ray band, and the temperatures corresponding to the three curves from bottom to top are: $1.16 \times 10^7\,\mathrm{K}, 5.80 \times 10^7\,\mathrm{K}$, and $1.74 \times 10^8\,\mathrm{K}$.

1.1.2 Thermal Bremsstrahlung Radiation

Bremsstrahlung radiation (Free-free radiation) is generated when high-speed charged particles, such as electrons, lose part of their kinetic energy due to the Coulomb force, and this part of the energy is released in the form of electromagnetic radiation. Bremsstrahlung

radiation produces a continuous energy spectrum. In astronomy and astrophysics, the research object is thermal bremsstrahlung, which refers to the electromagnetic radiation released by the interaction between electrons and ions in high-temperature plasma. Its intensity can be calculated using:

$$I_\nu \propto Z^2 n_e n_i g_\nu e^{-\frac{h\nu}{k_B T}} \nu^{-1} \tag{1.3}$$

where $I(\nu, T)$ is the radiation intensity, ν is the photon frequency, T is the plasma temperature, Z is the charge of the ions, n_e the electron density, n_i the ion density, h is Planck constant, k is Boltzmann constant, and $\tilde{g}_\nu$ is Gaunt factor (Brussaard and Van de Hulst, 1962). It can be seen that the radiation intensity approximately follows a power law relationship in the low frequency band, while it exhibits an exponential decay in the high frequency band. Thermal bremsstrahlung is the main cooling process at temperatures above 10^7 K; at this temperature, photons released are mainly donated to the X-ray energy range (Sarazin, 1986).

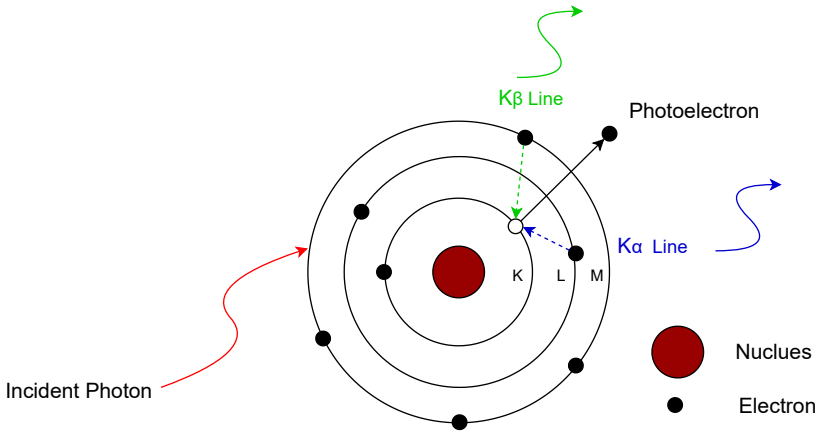

Figure 1.3: The principle of fluorescent X-ray generation. After absorbing the energy of the incident photon, the target material atom emits a photoelectron. A transition of an electron from a higher shell into the vacant state will happen, and at the same time, an X-ray photon with a certain energy is emitted, which is equal to the energy difference between the two involved states.

1.1.3 Characteristic X-ray Lines

Characteristic X-rays are produced when high-energy charged particles, usually high-energy electrons or high-energy photons, collide with the nucleus of the material. When the energy of electrons or photons is large enough, they can ionize the electrons in the

inner shell (usually the K shell or L shell) of the target atom, resulting in a vacancy in the inner shell, and now the atom is unstable and in an excited state. The electrons in the outer shell (usually the L shell and the M shell) with higher energy levels will transition to fill vacancies in the inner shell. During the transition, energy will be released in the form of photons, and the value of the energy is equal to the difference between the two electron energy levels. Since the energy of these photons falls within the X-ray range, they are known as characteristic X-rays. The characteristic X-rays produced when electrons transition from the L shell to the K shell are K_α X-rays, and the X-rays produced when electrons transition from the outer M shell to the K shell are K_β X-rays. The former has a higher intensity, and the latter has a higher energy. Figure 1.3 illustrates the principle of the characteristic X-ray generation. According to its definition, it can be inferred that characteristic X-rays can be produced in the process of bremsstrahlung radiation. This is why some isolated peaks often appear in the energy spectrum of thermal bremsstrahlung radiation. A well-known example is the Fe K_α line, which has an energy of 6.4 keV. Figure 1.4 shows an energy spectrum of bremsstrahlung radiation accompanied by characteristic X-rays.

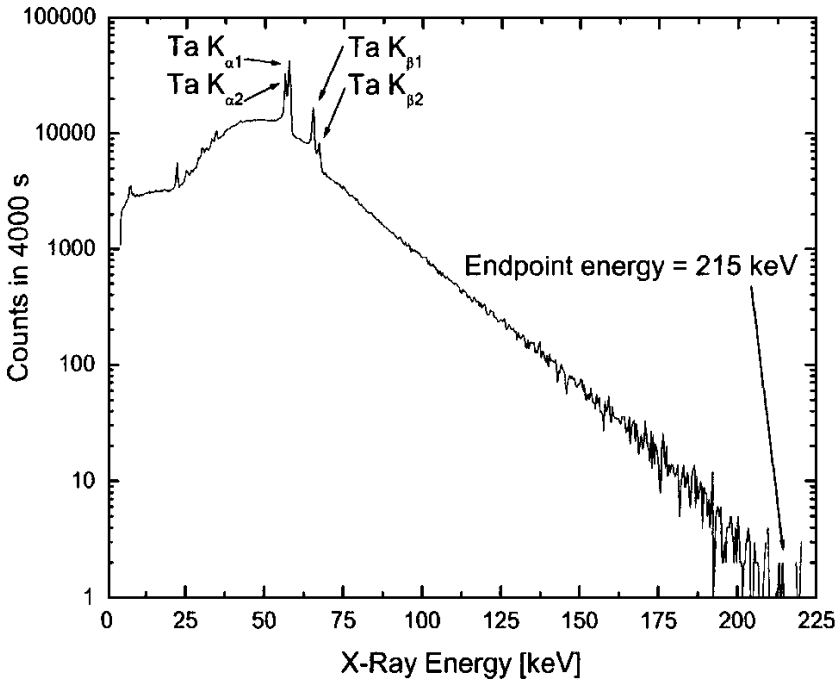

Figure 1.4: A typical X-ray spectrum showing the production of bremsstrahlung and characteristic X-rays. As the energy increases, the intensity of the bremsstrahlung radiation gradually decreases, and four characteristic X-rays of tantalum (Ta) atoms are clearly visible (Geuther and Danon, 2005).

1.1.4 Synchrotron Radiation

Charged particles, such as electrons, do a circular motion in a magnetic field under the Lorentz force. As a result of their acceleration, they emit electromagnetic waves, a process known as cyclotron radiation. The frequency of this radiation is given by Equation (1.4):

$$\nu_c = \frac{qB}{2\pi m} \tag{1.4}$$

where q is the charge of the particle, m is the mass of the particle, B is the magnetic field. This indicates that cyclotron radiation has discrete spectrum characteristics, as the frequency depends directly on the magnetic field and particle properties. When the electrons' speed approaches the speed of light (relativistic speeds), the emission becomes highly directional, concentrated along the tangential direction of the particle's trajectory. This produces intense radiation with notable polarization characteristics, known as synchrotron radiation. Figure 1.5 presents the process of synchrotron radiation generation. Unlike cyclotron radiation, synchrotron radiation exhibits a continuous spectrum due to the extremely high energy of the particles and relativistic effects.

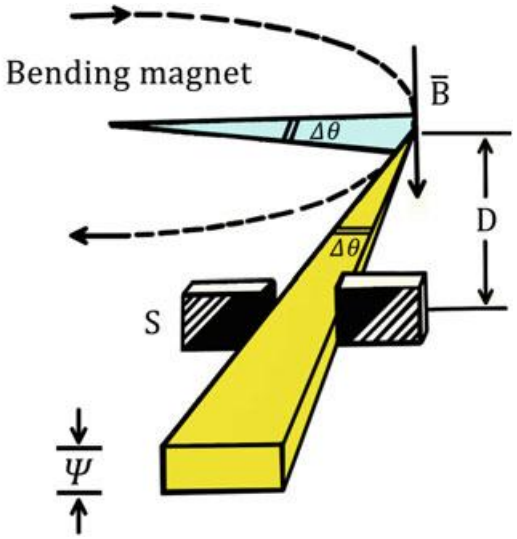

Figure 1.5: Synchrotron radiation emitted by a relativistic electron traveling along a curved trajectory. The dotted line indicates the trajectory of relativistic electrons as they are deflected by the magnetic field, and the magnetic field is perpendicular to the plane of the electron's orbit. When an electron is deflected, it will emit X-rays along the tangent direction of the trajectory, which is synchrotron radiation. The yellow area in the figure is the distribution of synchrotron X-rays. (Mobilio *et al.*, 2016).

The spectrum emitted by a single particle has a characteristic frequency, known as the critical frequency, as shown in Equation (1.5):

$$\nu_c = \frac{3}{2}\gamma^3 \frac{eB}{2\pi m_e c} \tag{1.5}$$

where e is the electron charge, m_e is the electron mass, B is the magnetic field, and c is the speed of light, and γ is the relativistic factor of the particle:

$$\gamma = \frac{E}{m_e c^2} \tag{1.6}$$

where E is the electron energy. Combining Equation (1.5) and Equation (1.6), we can get the relationship between critical frequency and electron energy:

$$\nu_c = \frac{3}{4\pi} \frac{eB}{m_e^4 c^7} E^3 \tag{1.7}$$

In the low frequency region, the spectrum shows a gentle power law growth; near the critical frequency, the spectrum reaches a peak; in the high frequency region, the spectrum shows a rapidly decaying exponential curve, as shown on the left of Figure 1.6.

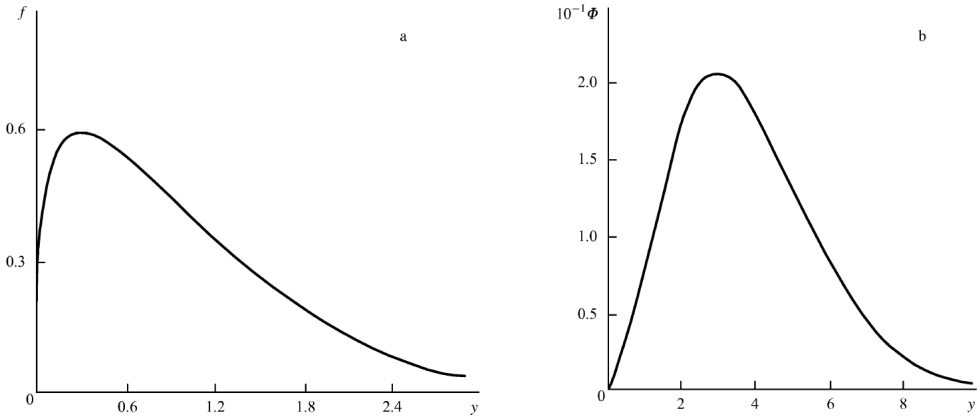

Figure 1.6: Comparison of the universal spectral distribution curves of synchrotron radiation power (left) and the blackbody radiation spectrum (right) (Ternov, 1995).

1.1.5 Compton Scattering

When a high-energy photon collides with an electron, part of the photon's energy is transferred to the electron, causing the photon's direction to change and lose part of its

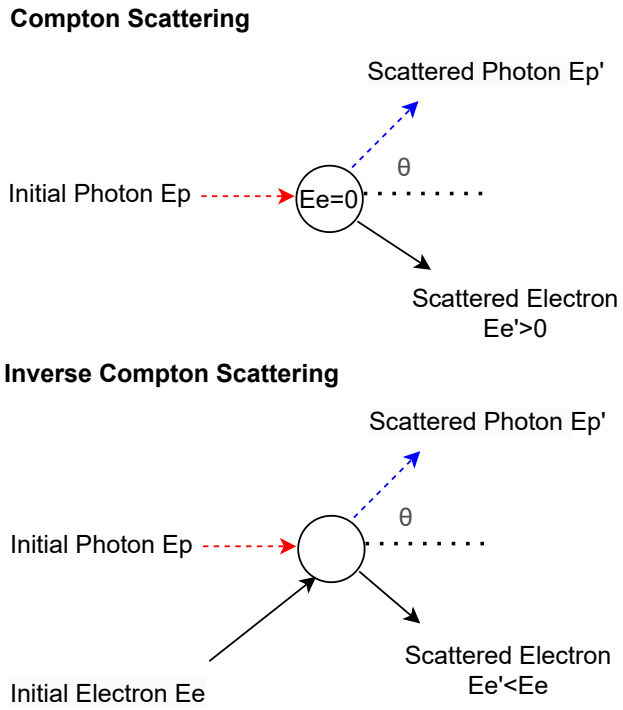

Figure 1.7: Compton scattering and inverse Compton scattering. In the former, photons lose energy, while in the latter, photons capture energy.

energy. This process is called Compton scattering. The relationship between the energy of the scattered photon E' and the initial photon energy E is expressed as Equation (1.8):

$$E' = \frac{E}{1 + \frac{E}{m_e c^2}(1 - \cos\theta)} \tag{1.8}$$

where m_e is the electron mass, c is the speed of light, and θ is the scattering angle. Due to variations in scattering angles, photons with identical initial energies exhibit a continuous energy distribution after scattering. This phenomenon explains the reason besides a full energy peak, a Compton scattering plateau appears when detecting photons with a specific energy. In high-energy astrophysics, there is a special phenomenon that when a low-energy photon collides with high-energy charged particles (usually electrons), it will gain energy from the electrons and is then scattered to a higher energy. This phenomenon is called inverse Compton scattering. The relationship between the energy of the scattered photon E' and the energy of the initial photon E can be obtained from Equation (1.9):

$$E' \approx \gamma^2 E(1+\cos\theta) \tag{1.9}$$

where γ is the relativistic factor of the electron as shown in Equation (1.6) and θ is the inverse scattering angle.

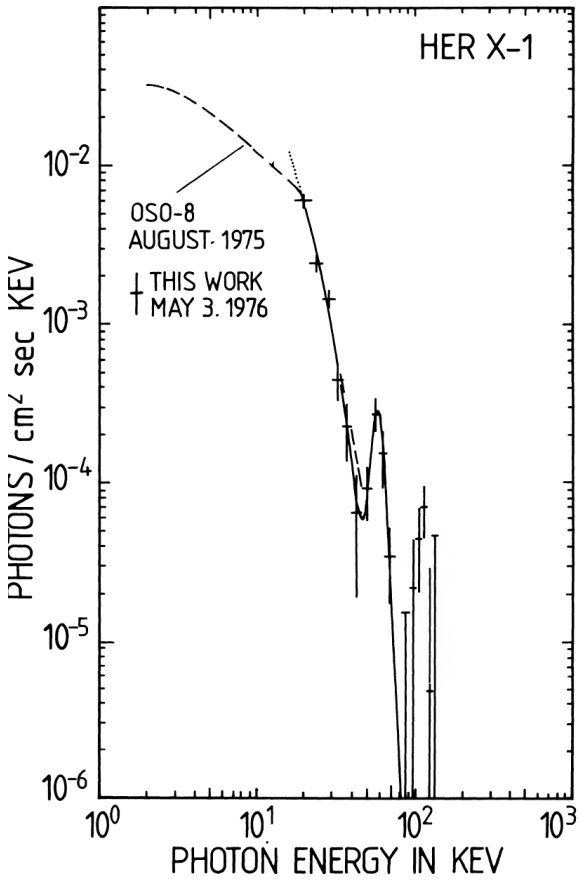

Figure 1.8: *Her X-1* spectrum, showing clear cyclotron absorption lines (Trümper *et al.*, 1978).

1.1.6 Cyclotron Absorption Lines

Cyclotron absorption lines are characteristic spectral lines produced when charged particles (usually electrons) absorb photons due to the cyclotron motion in a strong magnetic field. Specifically, when electrons move in a magnetic field driven by the Lorentz force, their trajectory is circular or spiral with a certain cyclotron frequency:

$$\nu_c = \frac{eB}{2\pi m_e} \tag{1.10}$$

In a strong magnetic field (such as on the surface of a neutron star), electrons may move at speeds close to the speed of light, and relativistic effects need to be considered:

$$\nu_c' = \frac{eB}{2\pi\gamma m_e} \tag{1.11}$$

where $\gamma = \frac{1}{\sqrt{1-\frac{v^2}{c^2}}} = \frac{E}{mc^2}$ is Lorentz factor in relativistic effects.

When the energy of the incident photon is equal to the energy corresponding to the cyclotron frequency of the electron or is an integer multiple of the energy, the electron will absorb the photon energy. This will lead to the continuous energy spectrum that was originally presented having a significant depression at some frequencies. Figure 1.8 shows the spectrum of *Her X-1*, where clear cyclotron absorption lines are visible. The magnetic field information can be obtained based on the energy of the absorption line, so cyclotron absorption lines play a significant role in the research about compact stars with strong magnetic fields.

1.2 Multi-Dimensional Insights: Energy, Timing, Imaging, and Polarization Analysis

This section introduces the process of X-ray interaction with matter and the key information sought during the X-ray detection. When detecting X-rays, the goal is to measure their energy and arrival time. Additionally, in certain scenarios, detecting the incident position and direction is also desired (Wilson and Yang, 2002). The phenomenology observed can be diverse. For example, the accretion process of an X-ray binary composed of a compact star and its companion star holds significant implications for comprehending the properties and evolution of compact objects. Due to the differences in compact stars (mainly neutron stars and black holes) and companion stars (high-mass and low-mass), different physical processes will occur (Van der Klis, 2006). For a High-Mass Neutron Star X-ray Binary (HM-NSXRB), the neutron star will absorb the material of the companion star through wind accretion. Due to the extremely large magnetic field and hard surface of the neutron star, the particles move to the polar cap of the neutron star along the magnetic field line (Becker *et al.*, 2012). Subsequently, soft X-rays are continuously emitted via black body radiation, then harder X-rays will be produced through the inverse Compton scattering process (Nelson *et al.*, 1993) and potentially accompanied by the emergence of cyclotron absorption lines (Staubert *et al.*, 2019), which requires the satellite payloads to have a wide energy response range and good energy resolution to research these phenomena. On the other hand, in a Low-Mass Black Hole X-ray Binary (LM-BHXRB), the black hole tends to attract material from its companion star via

the Roche lobe, forming an accretion disk around the black hole (Shakura and Sunyaev, 1973). When the temperature of the accretion disk reaches a sufficiently high level (10^4-10^5 K), the accretion disk enters a hot state and triggers an X-ray outburst (Lasota, 2001; Done *et al.*, 2007). During this process, Quasi-Periodic Oscillation (QPO) signals (Belloni and Motta, 2016) can be observed in the power spectral density obtained through the light curve, which requires the satellite payloads to have the capacity to record the time information of the X-ray event accurately. In addition, accurate X-ray source localization and spatial structure mapping are crucial to understanding the distribution and environment of high-energy astrophysical objects, which is why obtaining the incident position of X-ray photons and imaging of X-ray sources are crucial in X-ray astronomy. X-ray polarization measurement provides important insights into the underlying radiation mechanisms and the physics of extreme environments by revealing the geometry and magnetic field structure of the emission region. It is therefore an important component of the new generation of X-ray observatories.

1.2.1 X-ray Interactions with Matter

The interaction between high-energy electromagnetic radiation and matter includes the photoelectric effect, Compton scattering, electron-positron pair production, and a special type of elastic scattering without energy transfer, called Rayleigh Scattering. There are many factors related to the cross section of the reaction (reaction probability) between the photon and matter. In general, the energy of the photons (E) and the atomic number (Z) of the target material are two very important factors. Figure 1.9 shows the dominant interaction types under different photon energies and different target material atomic numbers: when the photon energy is low, the photoelectric effect is dominant. When the photon energy is very high, the electron-positron pair production is dominant, and Compton scattering is in a transitional state. As the atomic number increases, the width of the energy region where Compton scattering is dominant is compressed. Since the energy of X-rays cannot reach the minimum energy required to produce a positron-electron pair, the photoelectric effect and Compton scattering are the main forms of interaction between X-ray photons and the matter in the detector.

Photoelectric Effect

The photoelectric effect, also known as photoelectric absorption, is the process in which the photon interacts with the atom of the target material, transferring the energy to the electron outside the nucleus, causing the electron to break away from the atom and become a photoelectron. The energy of a photoelectron $E_{\text{photoelectron}}$ is equal to the initial photon energy E_{photon} minus the binding energy of the electron E_{binding}:

$$E_{\text{photoelectron}} = E_{\text{photon}} - E_{\text{binding}} = h\nu - E_{\text{binding}} \tag{1.12}$$

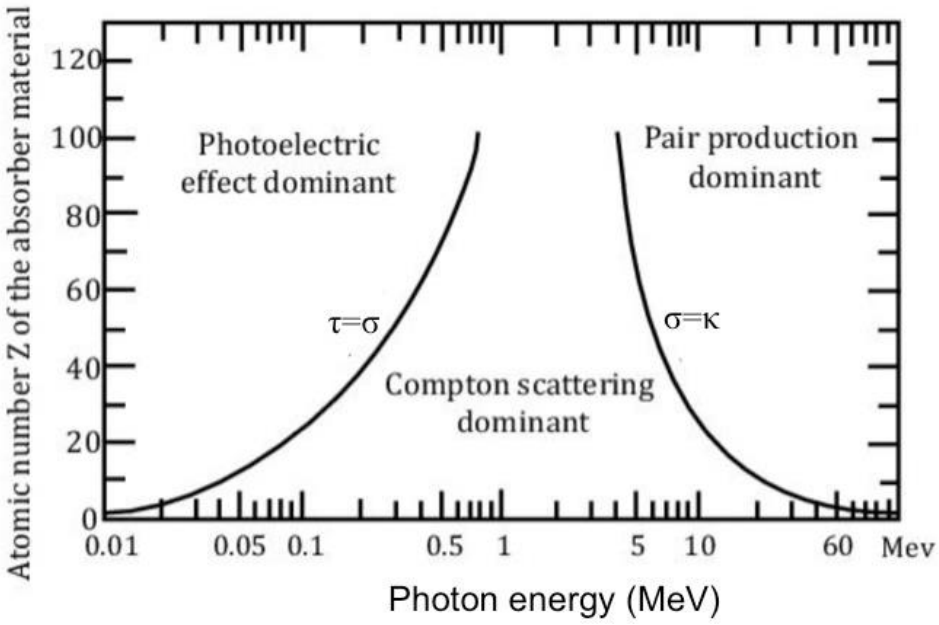

Figure 1.9: The dominant interaction type in different regions with different photon energies (E) and different atomic numbers (Z). The photoelectric effect is dominant in the low energy region, while pair production is the main type in the high energy region. As the atomic number increases, the energy region where the photoelectric effect and electron pair production are dominant increases respectively (Knoll, 2010).

The cross section of photoelectric absorption σ is related to the atomic number of the absorbing material Z and the photon energy E:

$$\sigma \propto \frac{Z^5}{E^{7/2}} \tag{1.13}$$

As the atomic number of the target material Z increases and the photon energy E decreases, the probability of photoelectric absorption increases. Photoelectric absorption is the predominant mode of interaction for X-rays, especially at low energies, which forms the theoretical basis for X-ray energy detection. Since the atom emits a photoelectron after the photoelectric effect, the existence of a vacancy may produce characteristic X-rays and Auger electrons.

Compton Scattering

Compton scattering takes place extensively in the interaction between the incident photon and the absorbing material. For the theory of Compton scattering, see Section 1.1.5.

Pair Production

If a high-energy photon with energy larger than the sum of the rest energy of an electron and a positron (1.022 MeV), the photon may annihilate under the influence of the Coulomb field of the nucleus or electron, producing a pair of positron and electron. The reaction process is as follows:

$$\gamma + Z \rightarrow e^- + e^+ + Z \tag{1.14}$$

where Z is the nucleus that interacts with the photon, as the photon energy E increases and the atomic number of the material Z increases, the probability of the pair being produced will greatly increase. Due to the positron's instability, it often annihilates with an electron, releasing a photon with an energy of 0.511 MeV.

1.2.2 X-ray Energy Spectrum Measurement

X-ray energy spectrum measurement is one of the most important measurements in X-ray astronomy. By analyzing the distribution of X-ray radiation in different energy ranges, the physical properties and radiation mechanism of astronomical sources can be revealed. The detailed characteristics of the energy spectrum, such as continuum model, spectral line (emission and absorption lines) distribution (Schwarm *et al.*, 2017), peak broadening or shift effect (Doppler effect and gravitational redshift) (Molin *et al.*, 2023), and high energy tail, often reflect the special physical processes under extremely high temperature, extremely strong density extremely strong gravities, and extremely strong magnetic fields in the universe. The X-ray energy spectrum is the distribution of photon number or density as the energy changes, usually with energy (keV) as the horizontal axis and photon count rate (or radiation intensity) as the vertical axis. X-ray energy spectrum measurement relies on the photoelectric effect generated by the interaction between photons and matter. Let's focus on the solid-state detector. During this process, the X-ray photon transfers its energy to an electron within an atom of the detector material, ejecting it as a photoelectron, whose energy can be calculated by Equation (1.12). This high-energy photoelectron moves rapidly through the detector material, further exciting surrounding electrons. These electrons gain sufficient energy to transition into the conduction band, leaving behind corresponding holes in the valence band and generating electron-hole pairs. The number of electron-hole pairs produced is directly proportional to the energy of the incident X-ray photon E_{photon} and is inversely related to the average ionization energy ω of the detector material. Thus, a photon's energy can be quantified by counting the number of electron-hole pairs generated:

$$N = \frac{E_{\text{photon}}}{\omega} \tag{1.15}$$

where N is the number of electron-hole pairs generated, E_{photon} is the incident photon energy, and ω is the average ionization energy, which refers to the energy consumed for each electron-hole pair produced. Average ionization energy ω depends on the type of material. For silicon material, ω is about 3.6 eV, while for gas detectors, this value is about tens of electron Volts. Generally, the smaller the average ionization energy, the larger the number of electron-hole pairs generated at the same energy, and the better the energy resolution will be. In practical detection scenarios, several factors contribute to variations in the number of electron-hole pairs generated by photons of a specific energy. These factors include:

- Interaction mechanisms: Although photoelectric absorption is the primary interaction mechanism for low-energy X-ray photons in the detector, some photons undergo Compton scattering. If scattered photons escape the detector, not all the photon energy is absorbed, leading to the formation of a Compton scattering plateau.

- Statistical fluctuations: The interaction between photons and detector material is inherently a random process. Variations in energy deposition and transfer efficiency result in statistical fluctuations in the number of generated electron-hole pairs. The number of electron-hole pairs generated by photons in semiconductors does not completely follow the Poisson distribution. This fluctuation is smaller than the Poisson process. To characterize this deviation, the Fano factor (Fano, 1947) is introduced, which is defined as the ratio of the actual variance to the Poisson variance. For silicon, the Fano factor is about 0.12, which means that the fluctuation of the number of electron-hole pairs is about 12 % of the Poisson case.

- System noise: Noise in the detector and associated electronics also affects the measurements. This noise arises from both the intrinsic performance of the detector and external environmental factors, further contributing to variations in the number of electron-hole pairs.

Due to the influence of the above factors, when measuring the energy of X-ray photons with a certain energy, there is a fluctuation in the measurement results, which is manifested in the energy spectrum as a certain broadening of the peak. Full Width at Half Maximum (FWHM) is introduced to quantify the width of the distribution. In X-ray detection, FWHM is often used to measure the energy resolution of the detector system. The energy resolution of the detector system for a certain energy is defined as:

$$R = \frac{\text{FWHM}}{E_0} \times 100\% \tag{1.16}$$

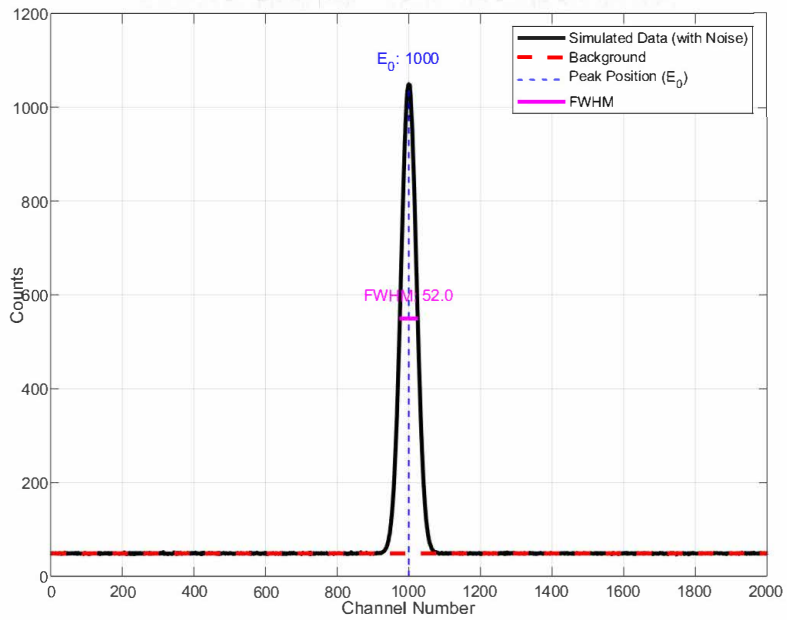

Figure 1.10: An energy spectrum featuring a full-energy peak. The center of the peak, denoted as E_0, corresponds to the peak energy, and the FWHM is highlighted in the figure.

Figure 1.10 shows the energy spectrum with a full energy peak. The center of the full energy peak represents the energy E_0, and the FWHM is marked in Figure 1.10. These two values can be used to calculate the resolution of the full energy peak based on Equation (1.16).

In an X-ray energy spectrum measurement, the collimator increases measurement accuracy and signal quality by limiting the direction of incident X-rays and restricting the Field of View (FoV). The wall of the collimator selectively absorbs off-axis photons with energies below a specified threshold, effectively reducing low-energy background noise from non-target directions and minimizing the impact of scattering. By filtering out irrelevant signals, the collimator significantly improves the Signal-to-Noise Ratio (SNR). In addition, it also mitigates the probability of invalid events, consequently reducing dead time and the probability of event pile-up.

1.2.3 X-ray Timing Measurement

The time-related study of X-ray events plays an important role in astronomy because it provides us with a unique perspective to study the dynamic processes of high-energy celestial bodies in the universe. Through time-related observations and analysis, the properties and behaviors of celestial bodies such as pulsars, black holes, and X-ray binary

systems, and the physical mechanisms behind them can be deeply revealed.

Light Curve

Light curve measurement is the most basic method for X-ray dynamic research. Light curve refers to the curve of the number of photons changing with time. Since the number of photons has a certain proportional relationship with the flux and brightness, it shows the brightness fluctuation of the star and its time evolution characteristics. The number of photons usually means the total number of photons received by a detector in a given time in a specific wavelength range. And flux refers to the number of photons that pass through a specific wavelength range per unit area per unit time. The number of photons received by the detector N can be calculated from the flux F and the detector area A:

$$N = F \cdot A \cdot \Delta t \tag{1.17}$$

The relationship between flux F and luminosity L is shown in Equation (1.18):

$$F = \frac{L}{4\pi d^2} \tag{1.18}$$

where d is the distance between the source and the observer. The flux changes with time on different timescales. Light curves are crucial for capturing transient phenomena such as Gamma-Ray Bursts (GRB) (Meszaros, 2006), periodic phenomena such as the rotation signals of pulsars (Caballero and Wilms, 2012) or QPOs (Belloni and Motta, 2016) of compact star accretion disks.

Power Spectral Density

By applying a Fourier transform, the time domain light curve is converted into the frequency domain, then we get the Power Spectral Density (PSD) (Youngworth *et al.*, 2005), which reveals the power of various frequency components. The PSD is a powerful tool for identifying periodic signals, like those from pulsars or QPO, which appear as distinct peaks, as shown in Figure 1.11. This approach also facilitates the analysis of the energy distribution of GRBs across different time scales, linking rapid variability to high-frequency features and gradual changes to low-frequency components.

Time resolution is a critical parameter for evaluating the accuracy of time measurement. It describes the accuracy of the system in measuring the time when an event occurs, that is, how accurately it can determine the moment when an event occurs. Several factors influence time resolution, including the detector's response speed, clock frequency, clock stability, and electronic noise levels. A faster detector response, a higher clock frequency, a lower jitter, and a lower electronic noise level contribute to improving time resolution.

Another important concept is dead time. It is defined as the smallest time interval that a system can reliably distinguish between two consecutive events. During this period, the

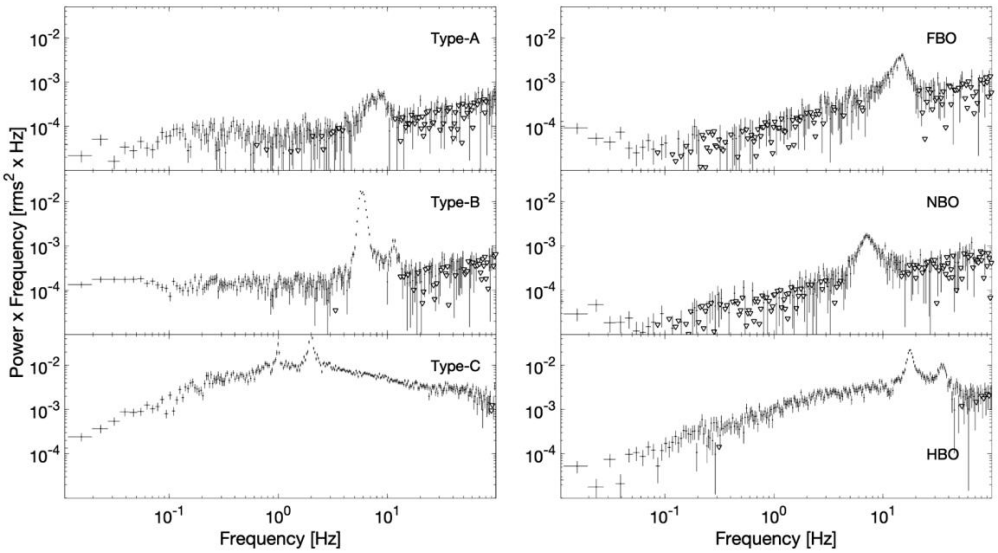

Figure 1.11: Left panels: examples of low-frequency QPOs from BH XRBs. From top to bottom, QPOs are taken from XTE J1859+226, GX 339-4, and again GX 339-4. Right panels: examples of QPOs from NS XRBs. From top to bottom, QPOs are taken from GX17+2, again GX17+2 and Cyg X-2. Some isolated peaks can be seen in the PSD (Ingram and Motta, 2019).

system is unresponsive to external input signals and unable to record new events. Dead time significantly impacts a system's event rate measurement. Dead time typically consists of contributions from both the detector and the electronic system. Dead time caused by electronic systems can be minimized by optimizing data processing methods, such as applying pipeline architectures, adopting parallel data processing and transmission techniques, and increasing processing speed using technologies like high-speed networks (e.g., Gigabit Ethernet). The evaluation of dead time is relative and closely related to the source flux. When the source flux is high, meaning that events occur at a higher rate, the system must have a shorter dead time to avoid event loss. Conversely, with a lower source flux, a longer dead time may be tolerable. This relationship emphasizes the importance of detector systems with appropriately minimized dead time to handle varying source flux conditions effectively, particularly in high event rate scenarios. Dead time can be minimized, but can not be eliminated. A well-designed detector system should avoid paralyzable dead time. Paralyzable dead time means that events occurring during the dead time will extend the system's dead time. This cumulative effect will cause the entire detection system to collapse. Considering the case without paralyzable dead time, the count rate can be calibrated, and the count rate can be accurately corrected based on the dead time τ, as described by Equation (1.19):

$$R_{\text{measured}} = \frac{R_{\text{real}}}{1 + R_{\text{real}} \cdot \tau} \tag{1.19}$$

where R_{real} and $R_{measured}$ are the real count rate and the measured count rate, respectively.

Accurate timing measurement of X-ray events relies on a system with high time resolution. To effectively obtain count rate in energy spectrum measurements and light curves, fast response detectors and a data acquisition and processing system with relatively small dead time are required. When an X-ray event occurs, a trigger signal is generated, and the back-end electronics use this signal to record the current time. The time recording process will be introduced in Chapter 4.

1.2.4 X-ray Imaging Measurement

X-ray imaging provides unique insights into phenomena that cannot be observed in other bands. It enables the study of special physical processes, such as the distribution and evolution of the high-temperature plasma following a supernova explosion, and reveals intricate structures of objects, like the cluster of galaxies. Moreover, X-ray imaging offers precise two-dimensional positional accuracy, which is crucial for locating cosmic energy sources and transient events (Hernanz *et al.*, 2018). This capability also enables the generation of trigger signals for subsequent, more detailed observations.

Since X-rays cannot be refracted and imaged through ordinary lenses like visible light, multi-layer grazing incidence (X-rays are incident at a very small incident angle) (Joensen *et al.*, 1993) will reflect the X-rays step by step and focus them on the detector to form an image. The detector arranges sensitive elements on the surface of the detector to form pixels or units or combines them with special optical devices to achieve multi-channel signal collection and high-resolution imaging, showing remarkable performance in high-precision imaging demand scenarios. For instance, multi-anode SDDs (Campana *et al.*, 2011) achieve high spatial resolution through the precise arrangement of sensitive elements, while coded-aperture silicon photomultipliers (SiPMs) enable high-sensitivity imaging of complex radiation sources through specialized optical designs (Zhao *et al.*, 2021). The mechanism that multi-anode SDDs extract two-dimensional information from a one-dimensional signal readout array will be detailed in Chapter 3.

Spatial resolution and angular resolution are important parameters to evaluate the performance of X-ray imaging. Spatial resolution describes the system's ability to distinguish adjacent positions in space, usually in millimeters or micrometers, and directly affects the clarity of the image. Angular resolution describes the system's minimum angular difference in distinguishing targets in adjacent directions, usually expressed in radians, arcmin, or arcsec, and is mainly used in long-distance imaging scenarios. Therefore, in X-ray astronomy, angular resolution is a more commonly used physical quantity to evaluate the accuracy of imaging or positioning. Angular resolution is calculated by Equation (1.20):

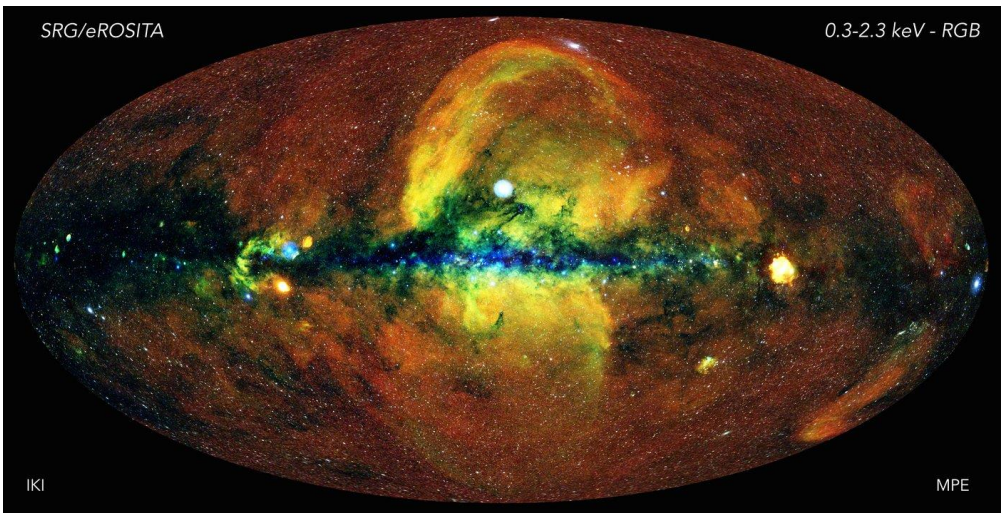

Figure 1.12: An all-sky X-ray image taken by the eROSITA X-ray telescope, showing the intensity of X-ray radiation in the energy range 0.3–2.3 keV (Jeremy Sanders and Hermann Brunner and the eSASS team (MPE) and Eugene Churazov and Marat Gilfanov (on behalf of IKI), 2020).

$$\theta = \frac{1.22 \cdot \lambda}{D} \tag{1.20}$$

where θ is the angular resolution in radians, λ is X-ray wavelength, and D is the effective aperture diameter of the collimator. During calculations, wavelength and aperture diameter should be expressed in the same unit.

However, Equation (1.20) represents the diffraction limit of angular resolution. Current technologies are far from reaching this limit in x-ray optics. The angular resolution based on Half-Energy Width (HEW) is an important indicator of the practical imaging system's resolving power for imaging systems by X-ray telescopes or other high-energy imaging systems. A point source, such as a very distant star, will not become an ideal point after being imaged by the optical system, but will spread into a spot, which is called the Point Spread Function (PSF). HEW represents the angular diameter corresponding to half of the energy contained in this point spread spot, therefore, it is expressed in angular units, such as arcsec or arcmin. In some cases, Half Power Diameter (HPD) is also used. Basically, it has a similar meaning to HEW. The angular resolution of x-ray focusing mirrors is primarily determined by surface figure accuracy and alignment precision of the multi-shell.

1.2.5 X-ray Polarization Measurement

X-rays are transverse waves, and one of the most important properties of transverse waves is that they are polarized. According to Maxwell's laws, the electric field and magnetic field directions of X-rays are perpendicular to each other, and the propagation direction is perpendicular to the plane formed by the electric field and the magnetic field. The direction of the X-ray electric field is regarded as the polarization direction. Based on the plane swept by the polarization direction, polarization can be divided into linear, circular, and elliptical polarization. The angular distribution of the trajectory of the photoelectron, generated by polarized X-ray interaction with the detector through the photoelectric effect, is directly related to the polarization direction. Therefore, the polarization direction can be obtained by detecting the angular distribution of the trajectory of photoelectrons (Hill *et al.*, 2006). Figure 1.13 presents the relationship between the angular distribution of the trajectories of photoelectrons and the polarization direction (Kaaret, 2021). The right part is the projection of the left part on the horizontal plane. The scattered photoelectrons present the highest density distribution along the X-ray polarization direction. Combined with the incident direction of the X-rays, the relevant information about the electric field and magnetic field of the incident X-rays can be obtained. Taking K-shell electrons as an example, the differential cross section of the photoelectric effect is shown as Equation (1.21):

$$\frac{\partial \sigma}{\partial \Omega} = r_0^2 \frac{z^5}{137^4} \left(\frac{mc^2}{E} \right)^7 \cdot \frac{4\sqrt{2}\sin^2(\theta)\cos^2(\phi)}{(1-\beta\cos(\theta))^4} \tag{1.21}$$

In the non-relativistic regime, the differential cross section for the K-shell photoelectric effect, projected onto the horizontal plane, is simplified as Equation (1.22):

$$\frac{\partial \sigma}{\partial \Omega} \propto \cos^2(\phi) \tag{1.22}$$

where ϕ is the angle between the photoelectron path and the polarization direction. The probability of photoelectrons emitting in a certain direction is proportional to the cosine square of the angle between that direction and the polarization direction, which means photoelectrons tend to emit in the polarization direction, and along this direction, the probability of emission is the highest. When the emission direction is perpendicular to the polarization direction, the probability of emission is lowest. The light blue ellipse shows the distribution intensity of photoelectrons in different directions. Therefore, obtaining the trajectories of photoelectrons and their distribution is the key to obtaining the polarization direction and then the direction of the electromagnetic field.

The degree of polarization reflects the non-uniformity of the distribution and is calculated from the maximum light intensity (along the polarization direction) and the minimum light intensity (perpendicular to the polarization direction) in the distribution (Ertugrul *et al.*, 2001), as shown in Equation (1.23):

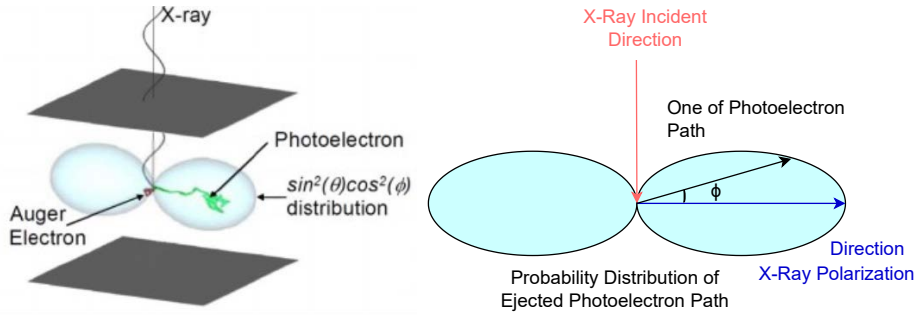

Figure 1.13: The relationship between the polarization direction of X-rays, the emission direction distribution of photoelectrons generated after photoelectric absorption, and the incident direction of X-rays. The emission direction that is collinear with the polarization direction has the largest photoelectron intensity, while the emission direction that is perpendicular to the polarization direction has the smallest photoelectron intensity.

$$P = \frac{I_{max} - I_{min}}{I_{max} + I_{min}} \tag{1.23}$$

1.3 X-ray Detector

Gas detectors, scintillator detectors, and semiconductor detectors are common X-ray detectors used in the astronomical field. Each kind of detector has unique characteristics that make it suitable for certain specific detection occasions.

Gas detectors (Sauli, 1998) use the ionization effect of X-rays in gases to generate electrons and ions and record the events through electrical signals formed by the generated electrons and ions. Some gas detectors have the ability to track the trajectories of the photoelectrons generated by the interaction between X-rays with the gas detector, which makes them suitable for measuring X-ray polarization. However, the energy resolution of gas detectors is typically poor, mainly due to their high average ionization energy, as well as the sensitivity of the ionization process and electron drift process to environmental factors. The stability of gas detectors is significantly affected by environmental factors such as temperature and pressure, which have limited their promotion and use, especially in the complex environment of astronomical research. Scintillator detectors (Moses, 2002) use materials that emit light (scintillation) under radiation, and these light signals are received and converted into electrical signals via photomultiplier tubes (PMTs) or Silicon photomultiplier tubes (SiPMs). Their high atomic numbers enable strong absorption efficiency of high-energy X-rays, making them suitable for high-energy X-ray measurements. For example, the high-energy X-ray telescope of the Hard X-ray Modulation Telescope (HXMT) uses NaI(Tl)/CsI(Na) composite crystal detectors (Zhang *et al.*,

2018). Scintillators also offer fast time responses; among them, fast-response scintillation detectors have response times as short as a few nanoseconds, making them ideal for time measurement and count rate measurement. However, they have relatively poor energy resolution due to fluctuations in scintillation photon yields. In addition, similar to gas detectors, scintillator detectors are easily affected by environmental factors.

Semiconductor detectors (Spieler, 2005), made from materials like silicon and germanium, are highly sensitive detectors to detect rays (such as X-rays and gamma rays) or charged particles. Semiconductor detectors have high sensitivity, good resolution performance, and compact size, therefore, semiconductor detectors are particularly suitable for X-ray satellite payloads. In addition, due to their fast response, whose value can be less than 1 ns, they are suitable for applications with high time resolution requirements. Based on pixelated design, semiconductor detectors can achieve high-precision two-dimensional imaging, supporting applications that require recording X-ray position information and imaging. This section provides a brief introduction to the two common types of detectors used in X-ray detection.

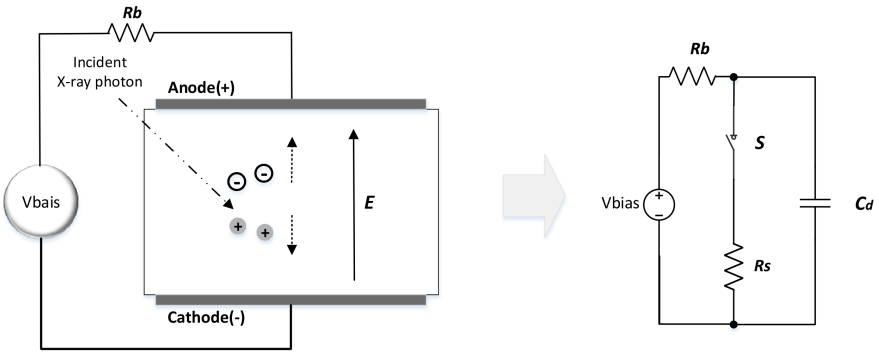

Figure 1.14: The smallest unit of the photoelectric conversion device, the PN junction and its equivalent circuit. C_d denotes the capacitance of the PN junction, while R_s represents its resistance. R_b is a bias resistor connected between the external bias voltage source (V_{bias}) and the detector anode. When an X-ray photon hits the PN junction, the PN junction absorbs the X-ray photon, inducing the ionization of silicon atoms and the generation of electron-hole pairs. These secondary charged particles migrate toward the electrode under the electric field. This process can be regarded as the process of charging the junction capacitor with a charging constant of $C_d R_b$.

1.3.1 Silicon Drift Detector

The Silicon Drift Detector (SDD) is widely used in X-ray astronomy and astrophysics due to its compact size, high detection efficiency, excellent energy resolution, and inde-

pendence from liquid nitrogen cooling. The SDD's fundamental operational principle closely resembles that of conventional photoelectric conversion devices based on silicon semiconductor technology (Xiong *et al.*, 2019), as shown in Figure 1.14.

However, unlike the traditional silicon photodiode with a pair of facing planar cathode and anode, the structure of the SDD is cylindrically symmetric, and a very small anode is centrally positioned on one surface and surrounded by a series of concentric annular electrodes, and the opposite surface is a planar cathode, as shown in Figure 1.15. After the electron-hole pairs are generated, the holes are absorbed by adjacent electrodes, and the electrons gather to form an electron cloud with a charge proportional to the incident X-ray photon's energy. The anode has the highest potential, causing the electron cloud to drift there and ultimately be absorbed by the anode. The detector structure design cleverly reduces parasitic capacitance, including SDD electric field design, the presence of annular drift electrode structure, and a smaller anode area, whose value can be as low as the order of several hundred femtofarads (fF), which will lead to:

- The output signal has a shorter rise time (collection time), which means the SDD has a fast response speed. Therefore, SDD is suitable for high count rate detection (Lechner *et al.*, 2001).

- The extremely short rise time of the output signal in SDD contributes to reducing the ballistic deficit effect. Moreover, the SDD's low capacitance results in decreased noise levels because of a low anode leakage current, thereby improving the SNR. Consequently, SDDs exhibit better energy resolution. For example, Amptek® FAST SDD and Vortex® SDD can provide a resolution less than 130 eV FWHM at the Mn K_α line.

1.3.2 Gas Pixel Detectors

X-ray polarimetric detectors must have two-dimensional imaging capability, with sufficiently small pixel sizes to accurately capture photoelectron trajectories.

The Gas Pixel Detector (GPD) is an advanced device designed for imaging and polarization detection in the X-ray energy band (Bellazzini *et al.*, 2007). The left part of Figure 1.16 shows key elements of the GPD and its response to a photo-absorbed X-ray. Its working principle has been described in the previous section, and the essence is to measure the trajectory distribution of photoelectrons. The incident photon reacts with gas atoms to produce a photoelectric effect, releasing a photoelectron. This photoelectron will further ionize when passing through the gas, forming a charge trajectory with a specific spatial distribution characteristic. The electrons generated by ionization are drifted to the Gas Electron Multiplier (GEM), forced by the electric field, achieving charge multiplication. The multiplied electron cloud is collected by a circuit with a 2-dimensional pixel signal readout function to form an "image" of the photoelectron trajectory. The

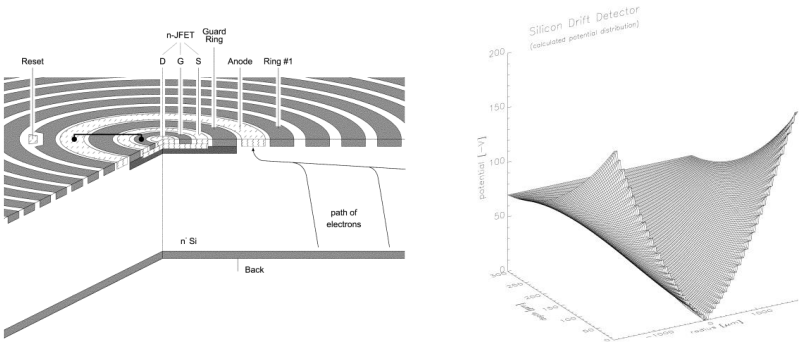

Figure 1.15: Left: Visualization of the central region of a cylindrical silicon drift detector. A small point anode is located in the center and maintained at the highest electrical potential. Surrounding this central anode is a series of concentric ring electrodes, each set to incrementally lower potentials with increasing radius; Right: its potential energy distribution in an SDD (Strüder *et al.*, 1998).

right part of Figure 1.16 presents a tracking measurement result of the absorption of an X-ray with 5.9 keV energy, including the energy and track information of the photoelectron, from which the polarization of the incident X-ray can be reconstructed. For the details, please refer to (O'Dell *et al.*, 2019; Costa *et al.*, 2001; Bellazzini *et al.*, 2006, 2007). The pixel size of the anode array in a GPD critically influences the spatial resolution and the accuracy of photoelectron track reconstruction. Smaller pixel sizes allow for finer sampling of ionization trails, which can improve the determination of the initial emission direction and thus increase the precision in X-ray polarization measurements.

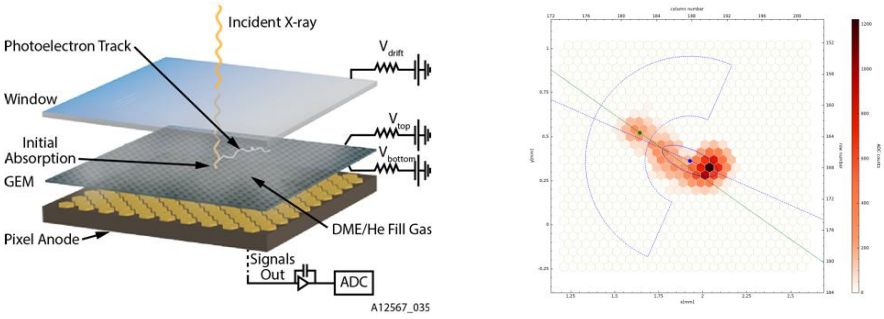

Figure 1.16: The structure of the GPD for X-ray polarization measurement and an ionization track measured from the absorption of a 5.9-keV X-ray with a 300×352 array of hexagonal pixels at 50 µm pitch (O'Dell *et al.*, 2019).

In this chapter, we discussed the generation mechanism of X-rays. We elaborated on the key information required for X-ray detection, including energy, time, imaging, and polarization, and briefly introduced two commonly used detectors in astronomical X-ray detection. This content will help us gain a deeper understanding of the importance of X-rays and their detection in astronomy and astrophysics, which lays the foundation for our subsequent study of celestial bodies and physical phenomena in the universe through X-ray detection, and further research of the origin, properties, and evolution of the universe.

Chapter 2

The eXTP Mission

The enhanced X-ray Timing and Polarimetry (eXTP) mission is a scientific space mission with the primary purpose of studying matter under extreme conditions of densities, gravities, and magnetic fields (Zhang *et al.*, 2017, 2019; Santangelo *et al.*, 2022). Specifically, the following three key questions will be studied thoroughly:

- What is the state of matter at supra-nuclear densities?
- What are the properties of space-time under extreme gravity?
- What are the laws of physics and astronomy in ultra-strong magnetic fields?

The compact objects in the universe, such as neutron stars and black holes, provide such an extreme physical environment characterized by extremely high densities, strong gravitational fields, and strong magnetic fields. The density of a neutron star can reach up to 10^{14} to 10^{15} grams per cubic centimeter — equivalent to hundreds of billions of tons in a single cubic centimeter, and the matter is compressed to the limit at such a high density, forming a quark-gluon plasma (Fortov and Fortov, 2016). The gravitational field of the black hole is among the strongest found in nature. A black hole with a mass equal to that of the Sun has a gravitational acceleration of approximately $1.5 \times 10^{13}\,\mathrm{m/s^2}$ at its event horizon, which is about ten trillion times (10^{13}) stronger than the gravitational acceleration on Earth's surface. Additionally, the magnetic field surrounding the neutron star is extraordinarily intense, and the magnetic field of the former can reach 10^{12} to 10^{15} Gauss (Romani, 1990), which is billions of times that of the Earth's magnetic field. In these extreme environments, X-rays are persistently emitted through a series of different kinds of mechanisms, as detailed in Chapter 1. These X-rays carry a large amount of information that reveals the state of matter and the form of physical laws in extreme conditions, thus providing evidence for scientists to answer the three questions.

The eXTP mission in its original configuration (see Figure 2.1) represents the newest generation of X-ray explorers with advanced "spectral-timing-polarimetry" measurement capabilities. It is designed to focus on the X-ray energy range across the 0.5–30 keV (up to 80 keV in extended mode), capitalizing on the mission's good timing precision and energy resolution, relatively large spectral coverage, and X-ray polarization measurement capabilities. As a new generation X-ray observational mission, the

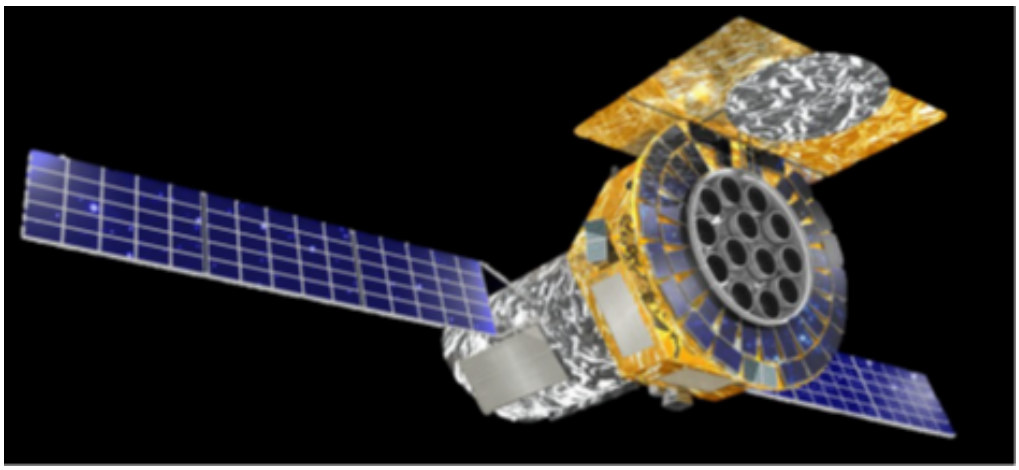

Figure 2.1: Artistic concept of the eXTP mission based on the current configuration (eXTP Collaboration).

eXTP not only inherits and integrates the strengths of existing observational missions but also introduces several innovative features: firstly, its largest effective detection area among current missions makes it particularly well-suited for the detection of weak X-ray sources; secondly, its unique capability for X-ray polarization measurement provides unprecedented insights into the radiation mechanism and magnetic field structure of these sources. In this chapter, we will present the scientific objective of the eXTP mission and the characteristics of the eXTP mission to achieve these science goals.

2.1 Scientific Objective

In this section, a lot of content comes from (in't Zand *et al.*, 2019; Zane *et al.*, 2012; Zhang *et al.*, 2019; Santangelo *et al.*, 2022; Watts *et al.*, 2019; Rosa *et al.*, 2019; Santangelo *et al.*, 2019), which presents details about the scientific goals of the eXTP mission. In particular, the scientific objectives of the eXTP mission are effectively introduced from the perspective of X-ray astronomy, in conjunction with the discussion of X-ray astronomy in Chapter 1. To achieve this, we will go deep into the physical phenomena and scientific objects tied to these extreme environments and present the X-ray generation processes as well as the corresponding mechanisms within them.

2.1.1 Physical Phenomena and Observed Objects at Supra-nuclear Densities

Supra-nuclear density phenomena (Lalit *et al.*, 2019) are mainly concentrated in neutron stars and other compact objects. When the original mass of a star is greater than about

8 times the mass of the Sun, its core mass at the end of its evolution usually exceeds 1.4 times the mass of the Sun (Chandrasekhar Limit (Thorsett, 1996)). In this case, the electron degeneracy pressure can no longer support the gravitational collapse of the core. The electrons are forced to combine with protons, forming neutrons through reverse beta decay. Then, the ultra-compact objects with neutrons as the main component will be generated, called neutron stars. Neutron stars are the densest known celestial objects in the universe (Lattimer, 2015), and the densities of their core matter can reach several times the saturation density of nuclear matter or even higher. This high-density environment provides a unique platform for exploring the equation of state (EOS) of nuclear matter under such extreme conditions, including the characteristics and evolution. The relationship between the mass (M) and radius (R) of a neutron star is an important clue to explore the state of matter inside it. By observing the spectrum and time characteristics of X-ray radiation, the distribution of matter and the degree of compression of a neutron star can be inferred. The relationship between neutron star mass (M) and radius (R) can be accurately measured and constrained through the method of pulse profile modeling, spectral modeling of bursts, and X-ray polarization measurement, and then the EOS of dense matter can be modeled (Steiner *et al.*, 2013). The polarization measurement capability of the eXTP mission is a highlight that eliminates the degradation of geometric parameters and improves the M-R relation measurement accuracy. Figure 2.2 presents different EOS predicted by different microphysics and conversion between EOS and M-R relations.

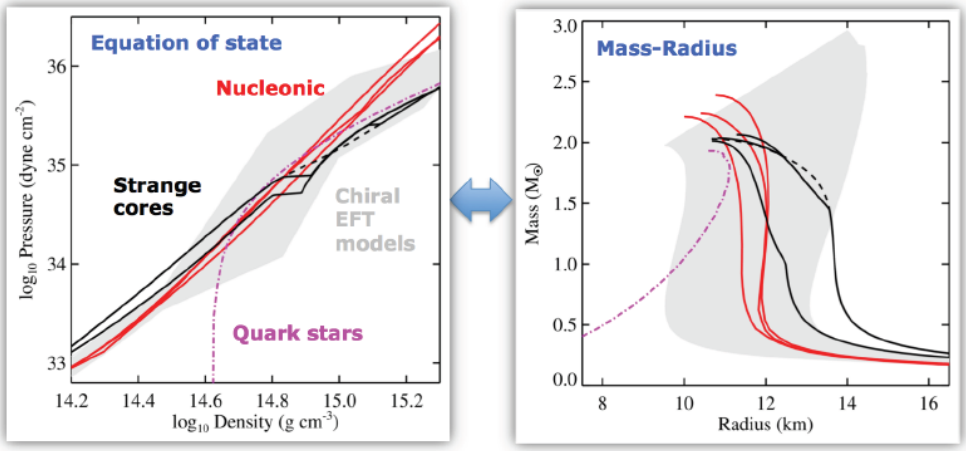

Figure 2.2: Different EOS predicted by different microphysics and converted to different M-R relations. Please refer to (Zhang *et al.*, 2017; Watts *et al.*, 2014) for a detailed description of this figure.

In low-mass X-ray binaries (LMXBs), the matter from the companion star is gravitationally attracted to the neutron star due to Roche-lobe overflow (Caballero and Wilms,

2012). Due to the law of conservation of angular momentum, matter cannot fall directly into the neutron star, but forms an accretion disk around the neutron star. During the accretion process, the matter in the accretion disk releases X-ray radiation due to viscous heating. When the material reaches the innermost part of the accretion disk, its speed is much faster than the rotation speed of the neutron star, so it must experience a severe loss of angular momentum and slowdown in the process of its falling to the surface of the neutron star, forming a dense boundary layer, especially when the magnetic field is not extremely strong. These boundary layers emit strong X-rays as the accreting material decelerates and releases gravitational energy, providing a direct method of observing high-density matter and acquiring important information on the surface of neutron stars (Paul, 2017). In this region, soft X-rays are inversely Compton scattered, and the high-energy X-ray component increases (Poutanen, 2006). Hard X-rays interact with the accretion disk, triggering fluorescence emission from iron, forming a broad and asymmetric iron K_α line (Bhattacharyya, 2011). The eXTP measures the innermost boundary of the accretion disk by observing kHz QPOs (Yu and van der Klis, 2002) and iron K_α reflection lines, which can constrain the relation between mass and radius, thus helping us deepen our understanding of the properties of dense matter.

When the star collapses, the radius decreases sharply, and the rotational inertia decreases synchronously. Due to the conservation of angular momentum, the rotational angular speed must increase significantly, which causes the neutron star to spin very fast. High-density matter allows neutron stars to maintain extremely high stiffness, and their spin periods can reach the order of milliseconds (Ott *et al.*, 2006). Pulsar is a special type of neutron star, and there is a certain angle between the direction of its magnetic field and the direction of rotation. The observatory can observe the light curve that changes with the period. By measuring the pulsar period, we can obtain its rotation rate and deceleration rate, and thus infer the pulsar's age and surface magnetic field (Ruderman, 1972).

The white paper of (Watts *et al.*, 2019) presents the first scientific goal of the eXTP mission — determining the characteristics of dense matter.

2.1.2 Physical Phenomena and Observed Objects under Extreme Gravities

Phenomena under extreme gravity are usually associated with compact objects such as black holes and neutron stars. Especially for the black holes, the spacetime around them is highly curved due to their strong gravity, creating special physical phenomena predicted by Einstein's theory of general relativity (Poisson *et al.*, 2011). In particular, near the event horizon of a black hole, the behavior of both light and matter follows the rules of strong gravity. Similarly, X-ray astronomy plays a critical role in research about the extremely strong gravity environment.

The gravitational redshift effect is a basic prediction of general relativity, which states

that the wavelength becomes larger because photons lose energy in an extremely strong gravitational field. The black holes provide such a proper environment that can be used to verify the correctness of general relativity. The accretion disk around a black hole is formed by the surrounding matter moving toward the center of the black hole under the action of gravity, converting gravitational potential energy into heat energy and radiation energy. Due to its extremely high temperature, the blackbody radiation at the inner edge has an X-ray band. The iron K_α line emitted from the black hole accretion disk will broaden and move to the long-wavelength band due to this effect when approaching the inner edge of the disk. Figure 2.3 demonstrates how iron spectral lines are progressively broadened and skewed due to various physical effects: the classical Doppler broadening caused by orbital motion, the relativistic Doppler shift caused by near-light speed rotation, and finally the gravitational redshift caused by the strong space-time curvature near compact objects as described by general relativity.

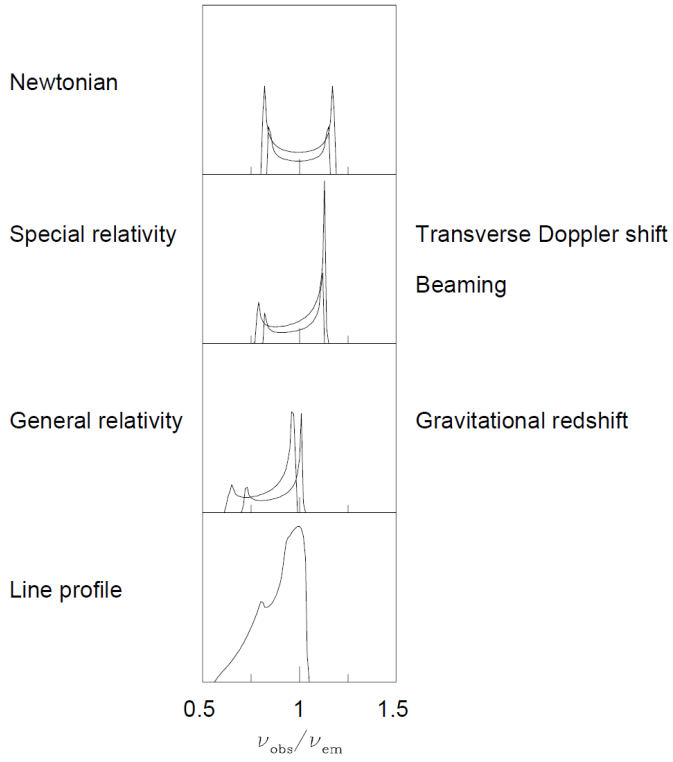

Figure 2.3: The upper panel presents the symmetric double peaks from a nonrelativistic disk, showing a classic Doppler shift; In the second panel, the effects of transverse Doppler shifting and relativistic beaming are shown; In the third panel, red shifted effect due to the gravitational redshift is presented; The lowest panel shows the integration of these effects into an energy spectrum (Fabian *et al.*, 2000).

For black holes, the timing, energy spectrum, and polarization of X-rays emitted from this region of the accretion disk extending to the innermost stable circular orbit (ISCO) can be used to infer two basic parameters of black holes: mass and spin (Miller and Miller, 2015). In particular, precise measurements of the iron K_α line and Compton reflection spectra in X-ray binaries (XRBs) and Active Galactic Nucleus (AGNs), combined with their polarization measurement results, enable the determination of the inner disk radius. Since the ISCO radius depends directly on the black hole's spin, this provides a powerful method for estimating the spin parameter. (Tanaka *et al.*, 1995; Jovanović, 2012; Fabian *et al.*, 2000; Rosa *et al.*, 2019). In addition, low-frequency and high-frequency QPOs can be commonly observed, which is an important probe for studying relativistic dynamics and offering another avenue for constraining black hole mass and spin (Rosa *et al.*, 2019). These observations, especially when combined in the spectral, temporal, and polarization domains, form a powerful tool for verifying general relativity in the strong gravitational field.

The white paper by (Rosa *et al.*, 2019) introduces the second scientific goal in detail — studying the state of matter and laws of physics in the strong field gravity regime, thereby enhancing our understanding of black holes and their gravitational fields.

2.1.3 Physical Phenomena and Observed Objects in Ultra-strong Magnetic Fields

Neutron stars have extremely high magnetic fields (Cardall *et al.*, 2001). Generally speaking, the magnetic field of the neutron star can be as high as 10^{12} G. Near the poles of neutron stars, strong magnetic fields dominate the emission of both radio and high-energy radiation. Specifically, high-energy particles move in a spiral motion along magnetic field lines, generating synchrotron radiation or curvature radiation due to acceleration. The rotation axis and magnetic axis of the neutron star are usually not aligned, and the emission from the polar regions sweeps across space as the star rotates. The radiation from the magnetic pole direction reaches the observatory periodically, therefore, we observe periodic pulse signals (Tauris and Manchester, 1998), as mentioned earlier, as shown in Figure 2.4

For some special neutron stars, the magnetic field around them can reach as high as 10^{14} G, called magnetars (Mereghetti *et al.*, 2015). Anomalous X-ray Pulsars (AXPs) and Soft Gamma-ray Repeaters (SGRs) are regarded as magnetars (Mereghetti, 2008). The phenomenon of magnetar outbursts, their timing properties, the accompanying X-ray spectral characteristics, and the existence of magnetars in binary systems are very worthy of study. The extremely strong magnetic field environment significantly impacts matter and radiation. By studying X-rays, the state of matter and its motion in such environments can be investigated. For instance, magnetic reconnection and ruptures in magnetars generate bursts of high-energy X-rays and gamma rays, along with intense pulse radiation in magnetars (Lyutikov, 2003).

Strong magnetic fields polarize X-rays, and analyzing the polarization properties of X-rays provides valuable insights into the magnetic field's structure (Fischer, 2011). The eXTP mission can verify theories of the magnetic field through X-ray polarization measurements and distinguish different types of radiation, such as "fan beam" and "pencil beam", based on their generation mechanism, and can also provide measurements of magnetic field direction and geometric parameters. Extremely strong magnetic fields provide excellent conditions for studying quantum electrodynamics (QED) effects (Akhiezer and Berestetskii, 1953), especially vacuum birefringence, which means that in a strong magnetic field, photons with different polarizations travel at different speeds — an effect similar to the light propagating in a birefringent crystal (Hattori and Itakura, 2013). The eXTP mission can use X-ray polarization detection to verify the vacuum birefringence effect and then provide observational evidence for the magnetic field structure independent of light curve and spectral line analysis for the magnetic field structure of neutron stars.

The white paper by (Santangelo *et al.*, 2019) introduces the third scientific goal in detail — studying the strongly magnetized objects, the state of matter, and physical laws under strong magnetic fields.

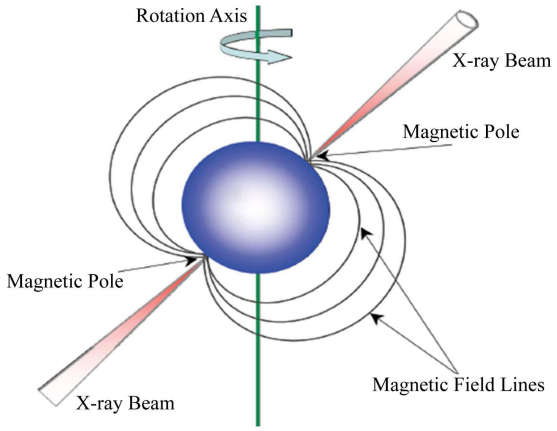

Figure 2.4: Schematic diagram of the reason why periodic signals can be detected from the pulsar (Rad *et al.*, 2014). Pulsars emit beams of radiation from their magnetic poles, which are misaligned with their rotation axis. As the star spins, these beams sweep across space, and when they point toward the X-ray observatory, they will be detected.

2.2 The eXTP Mission Overview

At the moment of writing this thesis, the payload was in the process of being restructured. However, it is not excluded that the older configuration could be considered again.

In addition, the instruments discussed can be used on other missions being designed. In what follows, we discuss the eXTP mission as it has been studied in the last 10 years. The scientific payload of the eXTP mission consists of four primary instruments: the Spectroscopic Focusing Array (SFA), the Polarimetry Focusing Array (PFA), the Large Area Detector (LAD), and the Wide Field Monitor (WFM). Together, these four payloads determine the characteristics of the eXTP mission. In this section, we will provide a concise overview of the features and structures of these payloads. Following this, a comparison between the eXTP mission with existing X-ray observatories currently in operation will be presented. The content of this section is largely derived from the literature (Zhang *et al.*, 2017, 2019; Feroci *et al.*, 2018; Hernanz *et al.*, 2018; Santangelo *et al.*, 2022; Ray *et al.*, 2024).

2.2.1 Spectroscopic Focusing Array (SFA)

The SFA consists of an array of nine identical X-ray telescopes and is mainly used as a spectral and timing observatory for the X-ray in the energy range of 0.5-10 keV. These Wolter-I grazing incidence X-ray telescopes, based on electroforming replication optics technology (Gale *et al.*, 2005), are equipped with a thermal shield, optical system, electron deflector, filter wheel, and a Silicon Drift Detector (SDD) based camera, as shown in Figure 2.5. The total effective area reaches up to 0.74 m^2 at 2 keV, achieved by multiple optics with short focal length. The angular resolution is better than 1 arcmin (HEW), and the FoV is limited to 12 arcmin (FWHM) in diameter, which means the instrument's observational sensitivity drops to half within 6 arcmin from the center of the FoV. The SDD ensures that SFA has an excellent energy resolution, less than 180 eV at 6 keV (FWHM), and a short dead time, which is expected to be less than 5 % at 1 Crab, which means when detecting a source with a brightness of 1 Crab, the event loss due to dead time will not exceed 5 %. Additionally, as a time spectrometer, the SFA holds a time resolution of less than 10 µs, underscoring its capability for precise time measurements.

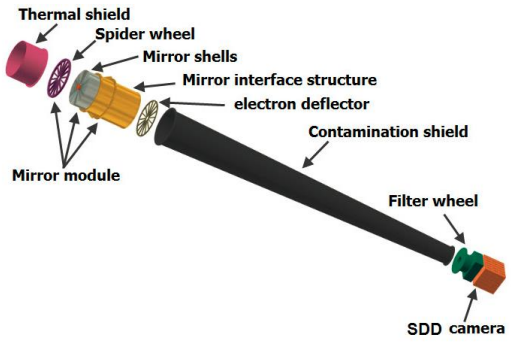

Figure 2.5: The schematic structure of one of the SFA telescopes (Zhang *et al.*, 2019).

2.2.2 Large Area Detector (LAD)

The LAD, in conjunction with the SFA, forms a comprehensive spectral-timing instrument. The LAD is specifically designed for photon-by-photon observations of X-ray sources within the 2 to 30 keV range, with the capability to extend to 80 keV in extended mode to record bright X-ray events. The architecture of the LAD and its basic structure — detector module will be presented in Chapter 3 in detail. One of the most significant features of the LAD is its large effective detection area, which reaches 3.4 m² at 8 keV. The key innovation of the LAD relies on the application of large area multi-channel SDDs and capillary plate collimators. The SDD leads the LAD to achieve an energy resolution of 260 eV at 6 keV (FWHM) and a timing resolution of less than 10 μs, respectively, which enables unprecedented spectral-timing studies by precise energy and timing measurements of X-ray photons. The capillary plate collimator will limit the detector's FoV to within 1° in the energy range from 2 keV to 30 keV, which reduces the background noise and unrelated events out of view.

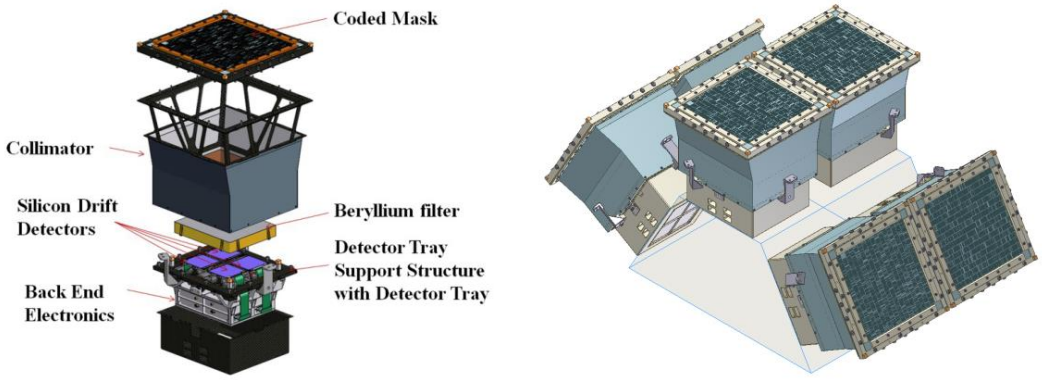

Figure 2.6: WFM camera and the layout of the three pairs of WFM cameras (Zhang *et al.*, 2019).

2.2.3 Wide Field Monitor (WFM)

The WFM is configured with three pairs of identical coded-mask cameras. One pair is aligned with the LAD's orientation, while the other two pairs are positioned at right angles on the vertical structure beneath the LAD plane to achieve a wide observation FoV of 4.1 steradians, equivalent to 33 % of the sky, as shown in the right part of Figure 2.6. This arrangement is crucial for the WFM's role: monitoring sky sources daily to provide long-term records of their variability and spectroscopic evolution, detecting transient and bursting targets, capturing unexpected events, and providing trigger signals for follow-up

observations by the SFA, PFA, and LAD. The detector (large area multi-channel SDD) with the ability to capture incident location information is applied and offers a location accuracy better than 1 arcmin. The WFM covers X-rays from 2 to 50 keV and delivers an energy resolution of approximately 300 eV at 6 keV (FWHM) and an absolute time accuracy of 1 μs, with a sensitivity of 4 mCrab for a 1-day exposure. Each camera comprises a code-mask, collimator, Beryllium filter, detector, electronics system, and mechanical tray, as shown on the left of Figure 2.6. The detectors and electronic systems of the WFM are similar to those of the LAD. The key difference is that, to enable 2D imaging, the detector's adjacent anodes in the WFM have a narrower spacing.

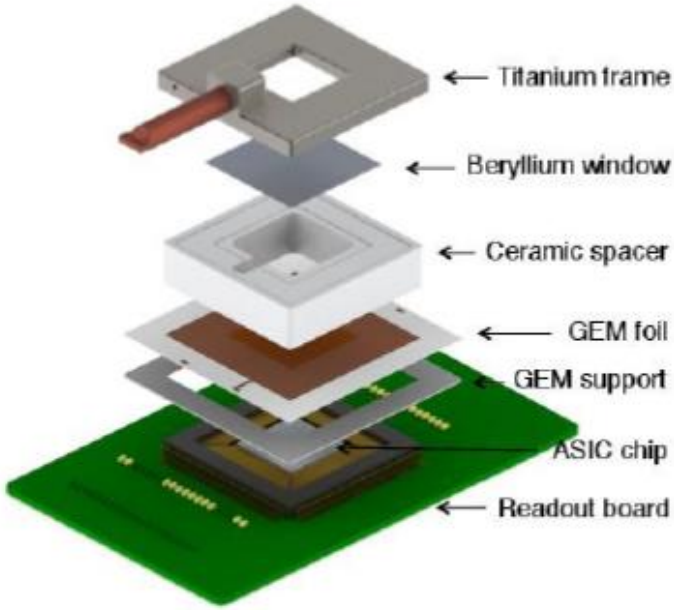

Figure 2.7: GPD prototype from Tsinghua University (Li *et al.*, 2015).

2.2.4 Polarimetry Focusing Array (PFA)

The PFA consists of 4 identical telescopes optimized for X-ray polarimetry, sensitive in the energy range of 2-8 keV, and has an angular resolution better than 30 arcsec (HPD) and a total effective area of around 900 cm^2 at 2 keV. The telescope used for the PFA is similar to that of the SFA. The ability to perform X-ray polarization measurement with high sensitivity is one of the most significant advantages of the eXTP mission based on the Gas Pixel Detector (GPD) used in the PFA. The GPD measures the linear polarization of absorbed photons by reconstructing the emission direction of the ejected photoelectron. The GPD applied in the PFA (Figure 2.7) consists of a gas cell with a thin 50 μm

Beryllium entrance window, a GEM that amplifies the charge of the electron tracks without changing the track shape, and a charge collection plane with the electronics system. More details about the PFA detectors are given in Section 1.3 of Chapter 1. The energy resolution is less than 18 % at 6 keV (FWHM), and the time resolution is 500 µs.

Table 2.1 outlines the key features of the four payloads of the eXTP mission. The combination of these advanced instruments allows the eXTP mission to provide detailed insights into high-energy astrophysical phenomena, making it a powerful tool for scientific discovery. Their complementary advantages will significantly influence the overall success and scientific output of the mission.

Table 2.1: Main Specifications of eXTP Payloads(Part 1)

Parameters	SFA	LAD
Energy range (keV)	0.5-10	2-30 (up to 80)
Effective area	0.74 m^2 at 2 keV	3.4 m^2 at 8 keV
Energy resolution (FWHM,6 keV)	180 eV	260 eV
Field of View	12 arcmin	1°
Time resolution	10 µs	10 µs
Dead time	5 % at 1 Crab	0.5 % at 1 Crab
Angular resolution	1 arcmin	-
Location accuracy	-	-
Minimum detectable polarization	-	-

Table 2.1: Main Specifications of eXTP Payloads(Part 2)

Parameters	WFM	PFA
Energy range (keV)	2-50	2-8
Effective area	-	900 cm^2
Energy resolution (FWHM,6 keV)	300 eV	18 %
Field of View	$\geq$ 3.2 Sr 20% response	8 arcmin
Time resolution	300 s for images/10 µs for event data	500 µs
Dead time	-	-
Angular resolution	4.3 arcmin	30 arcsec
Location accuracy	1 arcmin	-
Minimum detectable polarization	-	1.6 % (10^6, 1 mCrab)

2.2.5 The eXTP Mission Profile Summary

The eXTP mission will operate in a 550 km low Earth orbit with an inclination close to 0° to ensure minimal interference and consistent observing conditions. It will be launched from Wenchang, China, on a Long March 7 (LM7) rocket with a launch mass of 4500 kg. The mission will transmit data at a rate of 3.2 Tb/day, using ground stations in Sanya, China, and Malindi, Italy. The mission is expected to last 5 years, with the goal of being extended to 8 years. For more details on the eXTP spacecraft, launch, and orbit, please see (Zhang *et al.*, 2019; Santangelo *et al.*, 2022).

The Rossi X-ray Timing Explorer (RXTE), Chandra X-ray Observatory (Chandra), the X-ray Multi-Mirror Mission (XMM-Newton), the Extended Roentgen Survey with an Imaging Telescope Array (eROSITA), the Hard X-ray Modulation Telescope (HXMT), and Neutron star Interior Composition Explorer (NICER) represent a range of currently operational X-ray observatories. Compared with the eXTP mission, each has its characteristics and is suitable for different astronomical research fields. Table 2.2 shows the comparison of these X-ray observatories, including the characteristics and suitable fields.

Table 2.2: Comparison of X-ray Observatories

Observatory	Energy Range (keV)	Spatial Resolution	Energy Resolution	Time Resolution	Effective Area	Unique Capabilities
RXTE	2–250	Non-imaging, FoV ~1° (FWHM)	18% at 6 keV	1 μs	~6500 cm^2 at 6 keV(Proportional Counter Array)	Wide energy range, excellent time resolution
Chandra	0.1–10	0.5 arcsec	~100-200 eV at 6 keV	16 μs	~400 cm^2 at 1 keV	High spatial resolution, high sensitivity
XMM-Newton	0.1–15	15 arcsec (HPD); 6 arcsec (FWHM)	150 eV at 6 keV	0.03 ms (The European Photon Imaging Camera)	~1500 cm^2 at 1 keV	Spectral analysis, wide-field observations
eROSITA	0.2–10	~15 arcsec	140 eV at 6.4 keV	50 ms	~2400/1400 cm^2 at 1 keV	Wide-area surveys, high sensitivity in soft X-ray
HXMT	1–250	Non-imaging	2.5 % at 6 keV	Microsecond level(High Energy X-ray telescope)	~5000 cm^2 at 20 keV (High Energy X-ray telescope)	Wide-field high-energy X-ray observations
NICER	0.2–12	Non-imaging	~100 eV at 1 keV	~100 ns	~1900 cm^2 at 1.5 keV	Study the internal structure of neutron stars, support X-ray pulsar navigation (SEXTANT)
eXTP	0.5–30	1 arcmin (SFA); Fov 1°(LAD)	180 eV at 6 keV	10 μs(SFA, LAD)	~3.4 m^2 at 8 keV(LAD)	X-ray polarization measurement, high sensitivity, spectral and timing analysis

RXTE (Bradt *et al.*, 1990), despite lacking spatial resolution capabilities, is known for its wide energy range of 2-250 keV and time resolution of 1 μs. These characteristics make RXTE particularly effective for investigating rapidly variable X-ray sources.

Chandra (Weisskopf *et al.*, 2000) is famous for its unparalleled spatial resolution of 0.5 arcsec and high sensitivity, with an energy resolution of approximately 150 eV at 6 keV, which is very suitable for high precision imaging. However, Chandra's energy range

is relatively narrow, covering only 0.1–10 keV, which limits its application in studying high-energy X-ray sources.

XMM-Newton (Jansen *et al.*, 2001) is widely used in spectral analysis and wide field observations with an energy range of 0.1-15 keV, an energy resolution of 2.5 % (at 6 keV), and a spatial resolution of 6 arcsec, and it has a large effective area which is around 4 times larger than that of Chandra. Similar to Chandra, its energy coverage is somewhat limited.

eROSITA (Predehl *et al.*, 2007) offers wide-field X-ray survey capabilities with high detection sensitivity in the soft X-ray energy range from 0.2 to 10 keV. However, its energy coverage is not large, and its angular resolution, approximately 15 arcsec, is worse than that of XMM-Newton and Chandra.

HXMT (Zhang *et al.*, 2020) shares a similar energy range with RXTE (1–250 keV), making it well-suited for wide field high-energy X-ray observations. However, it doesn't have the imaging capacity. However, it is China's first space X-ray astronomical satellite mission, therefore, it has a milestone significance.

NICER (Arzoumanian *et al.*, 2014; Gendreau *et al.*, 2012) has high-precision X-ray timing, a large effective area (around 1900 cm^2 at 1.5 keV), and a 100-nanosecond time resolution. It can accurately measure the structure of neutron stars and support the SEXTANT (Station Explorer for X-ray Timing and Navigation Technology) task to achieve autonomous navigation of pulsars. Its advantages lie in its sensitive X-ray detection and timing capabilities, however, its disadvantages are its lack of imaging capabilities and its limited observation window due to the orbit of the International Space Station (ISS).

The eXTP mission covers an energy range of 0.5–30 keV, with an energy resolution of less than 180 eV at 6 keV and a time resolution better than 10 µs. The LAD has an effective area of 3.4 m^2 at 6 keV, which makes the eXTP mission the X-ray observatory with one of the largest effective areas, leading the detector to capture a significant number of X-ray events, thus offering a high observational sensitivity. In addition, the eXTP mission includes the unique capability of X-ray polarization measurement, which positions it as a critical tool for comprehensive X-ray astrophysical studies, together with its spectral and timing analysis capabilities.

2.3 The LAD and WFM in STROBE-X Mission

The WFM and the LAD concepts are integral to the Spectroscopic Time-Resolving Observatory for Broadband Energy X-rays (STROBE-X) mission (Figure 2.8) led by NASA. The Institut für Astronomie und Astrophysik of Eberhard Karl University of Tübingen (IAAT) participates in the STROBE-X mission and is responsible for the development of the back-end digital circuit systems for both the WFM and LAD of the STROBE-X mission (Hutcheson *et al.*, 2024). In light of this involvement, the following section provides an overview of the STROBE-X mission, more details are provided in (Ray *et al.*, 2018, 2024).

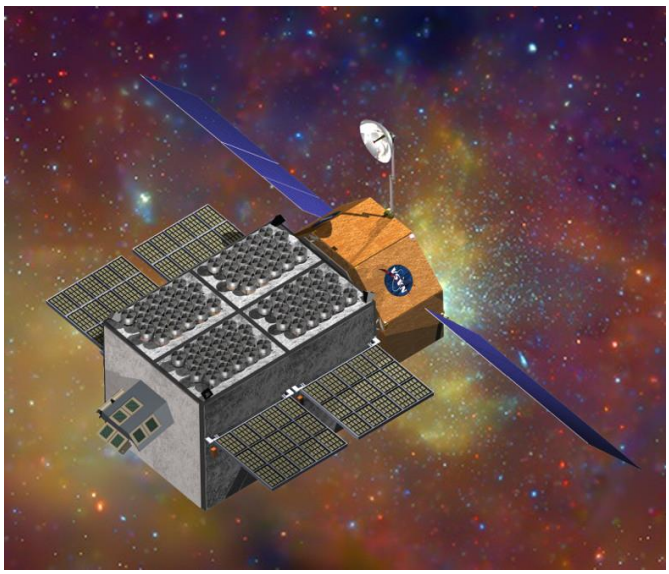

Figure 2.8: The artistic concept of the STROBE-X mission (Ray *et al.*, 2019).

The X-ray Concentrator Array (XRCA), the WFM, and the LAD constitute the instruments of the STROBE-X mission. Table 2.3 shows the parameters of these payloads in the STROBE-X mission.

Table 2.3: Parameters for XRC, LAD, and WFM in the STROBE-X Mission

Parameter	XRC	LAD	WFM
Energy Range (keV)	0.2–12	2–30	2–50
Effective Area	21,760 cm² (at 1.5 keV)	51,000 cm² (at 10 keV)	N/A
Time Resolution	100 ns	10 µs	0.1 ms
Energy Resolution (FWHM)	85–175 eV	200–300 eV	300 eV
Focal Length	3.0 m	N/A	N/A
Angular Resolution	2 arcmin	1° FWHM	4.3 arcmin
Detector Type	Silicon Drift Detectors (SDD)	Silicon Drift Detectors (SDD)	N/A
Quantum Efficiency	50% (at 15 keV)	N/A	N/A
Cooling System	Thermoelectric Coolers (TECs)	N/A	N/A
Field of View (FoV)	4 arcmin diameter	1° FWHM	4.1 sr
Sensitivity	N/A	N/A	600 µCrab (1 sec), 2 µCrab (1 day)
Position Accuracy	N/A	N/A	1 arcmin

The XRCA, a modular collection of identical X-ray Concentrator (XRC) units, is designed to cover the soft X-ray band (0.2–12 keV) by applying lightweight optical components that focus incoming photons onto solid-state detectors. This design achieves an energy resolution ranging from 85 to 175 eV and a time resolution of 100 ns. In addition, the effective area of the XRC can reach 21,760 cm² at 1.5 keV, representing an order of magnitude improvement over the previous NICER mission of NASA. The XRC instrument comprises several critical components, including a series of parabolic X-ray concentrator units based on grazing incidence reflection to focus X-rays; High-

precision SDDs are equipped, which feature aluminized film windows to ensure optimal energy and time resolution; and electronics systems. The properties and functionalities of the LAD and WFM in the STROBE-X mission are consistent with those in the eXTP mission. The WFM of the STROBE-X mission incorporates four pairs of coded-mask cameras, resulting in a significantly wider FoV. Additionally, the LAD in the STROBE-X mission benefits from an increased effective area, which enhances its detection sensitivity. Collectively, these three instruments establish a unique observatory characterized by a broad energy response (0.2–30 keV), fast response speed, and high sensitivity, making it exceptionally well-suited for spectral analysis, time-resolved studies, and all-sky monitoring.

In this chapter, we introduced the scientific objectives of the eXTP mission, explained its importance in studying the state of matter and its evolution under extreme conditions (such as extremely high densities, extremely strong gravities, and extremely strong magnetic fields), and established the connection between these research objectives and X-ray detection. In addition, we introduced the structure and characteristics of the eXTP mission in detail, especially its four core payloads. Finally, by comparing with existing X-ray observatories, we analyzed the advantages of the eXTP mission.

Chapter 3

The Large Area Detector

The Large Area Detector (LAD) (Feroci *et al.*, 2018) is designed to be a sensitive spectral-timing instrument for X-rays ranging from 2-30 keV. This chapter presents a comprehensive introduction to the LAD payload, including its structure and the composition designs of its detector and electronics. Due to the extensive number of detectors within the LAD, the modular design concept is applied to integrate multiple detectors to process high numbers of signals, which enhances the flexibility and efficiency of the installation and reuse of the electronics components. Consequently, this chapter will systematically describe each segment of the LAD detection chain, providing a detailed exploration of the functions and interconnections of the detector and each part of the electronics. Special emphasis will be placed on the large area multi-channel Silicon Drift Detector(SDD) (Campana *et al.*, 2011) and its associated Front-End Electronics (FEE). A thorough understanding of the detector and its FEE is essential for developing a reliable simulator, which replicates the behavior of the detector and its FEE by generating the corresponding output data. This simulator is a critical component of the preliminary testing system to evaluate and validate the MBEE in the primary phase. Some of part in this chapter is based on the content presented in the journal article authored by me as the first author. For further details, please refer to (Xiong *et al.*, 2025).

3.1 The LAD Payload Overview

The LAD payload on the eXTP mission is based on the concept earlier developed for a similar LAD instrument on the LOFT mission concept (Feroci *et al.*, 2012; Zane *et al.*, 2012). The main specifications of the LAD are presented in Section 2.2.2 and Table 2.1 in Chapter 2. The detector module is the basic detection unit of the LAD. The LAD instrument consists of an annular baseplate with a total number of 40 detector modules, forming a ring around the SFA and PFA (Xiong *et al.*, 2022). Figure 3.1 shows the position of the LAD in the eXTP mission, and each yellow rectangle represents a detector module in the LAD. Each detector module consists of large area multi-channel SDDs, capillary plate collimators, and a dedicated FEE equipped for each of the detector, MBEEs, and Module Power Supply Units (MPSUs). The mechanical frame supports all of these components. The structure and the assembly sequence of the LAD detector

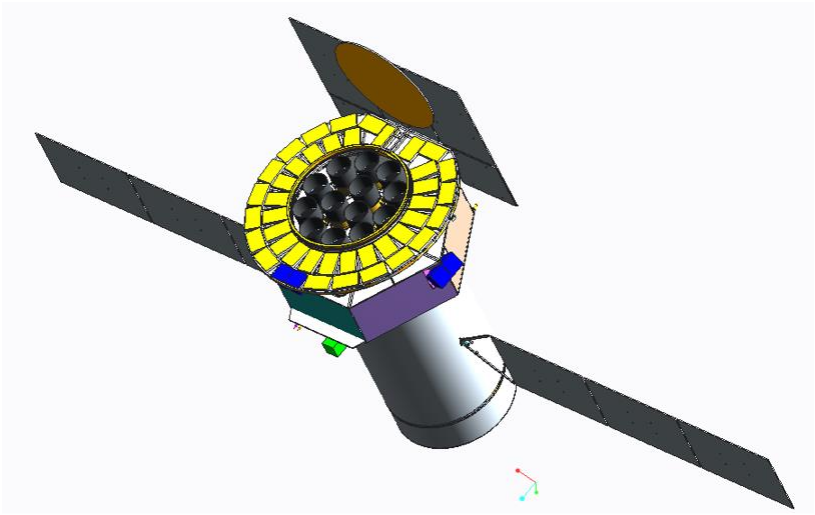

Figure 3.1: Schematic diagram of the eXTP mission. The yellow boxes indicate the LAD detector modules, which surround the SFA and the PFA at the center. The blue boxes represent the WFM, positioned to provide broad sky coverage for detecting transient and variable X-ray sources (eXTP Collaboration).

module are shown in Figure 3.2. The detector module consists of:

- Large area multi-channel SDDs: There are 16 large-area multi-channel SDDs in one detector module.

- Capillary plate collimators: The capillary plate collimator, a specialized lead-glass tile structure, incorporates thousands of microscale pores to effectively constrain the FoV to approximately 1°. Each detector has one collimator, therefore, there are 16 collimators in one detector module. Low-energy X-rays with incident angles outside the FoV are absorbed by the lead walls of the collimator. By selecting an optimal lead wall thickness, it is possible to absorb all X-rays below 30 keV that fall outside the FoV, thereby achieving effective collimation within the targeted energy range.

- FEE: As the first stage of the readout electronics, each detector has a dedicated FEE which is responsible for amplifying, shaping, and digitizing the X-ray signals in the anode channels of the detector, therefore, there are 16 FEEs in one detector module.

- MBEE: The MBEE in the LAD includes two identical boards, and each board interfaces with eight FEEs. The MBEE reads out the digitized event signals from the FEEs and provides a time stamp for each event, reconstructs the energy of the

X-ray event. In addition, it manages the module's electronics, generates housekeeping data, and transmits the processed data to the PBEE.

- MPSU: The MPSU is the power supply for module electronics and the voltage provider for the detector during operation. There are three types of voltages: Low Voltages (LVs) for module electronics, Medium Voltage (MV), and High Voltage (HV) for detectors.

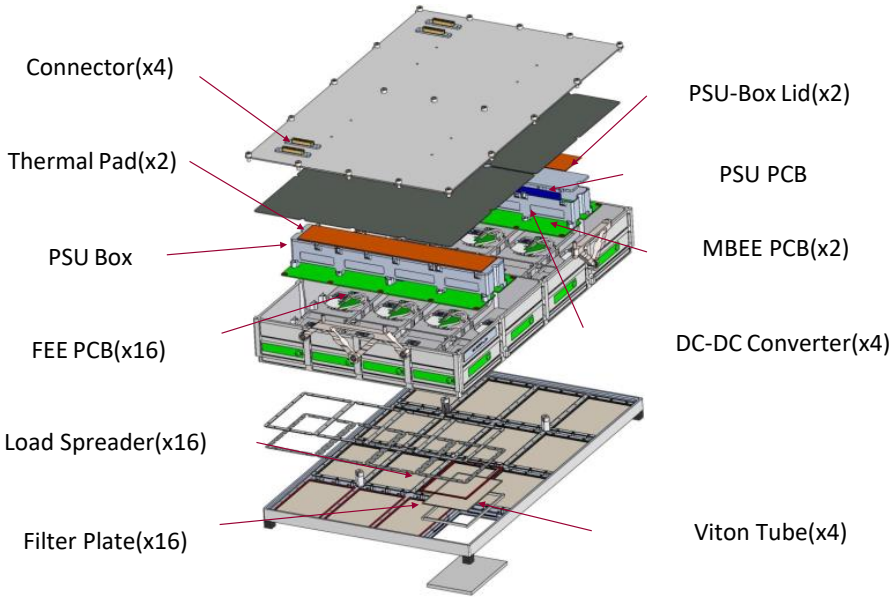

Figure 3.2: Structure and assembly sequence of the LAD detector module (G. Lombardi, INAF/IAPS).

The LAD instrument incorporates 640 large area multi-channel SDDs, offering a large detection area and a high sensitivity. However, managing such a large number of detectors is a difficult task, and the use of large detection arrays increases the complexity of data processing. To address these difficulties, the detection module is applied to serve as the LAD detection unit, and the back-end circuit, as the core circuit of data processing, is also divided into two different levels, the first of which is the MBEE mentioned above. Forty detector modules are supported through an annular detector panel, which hosts the second level of back-end electronics— Panel Back End Electronics (PBEE). The PBEE acts as an intermediary between the MBEE and the central Instrument Control Unit (ICU) of the LAD. In general, the telecommands are assigned by the ICU and transmitted through the PBEE to the MBEE. The MBEE will decode the telecommand and notify the electronics of the detector module to execute the corresponding operation.

On the other hand, data such as science data and housekeeping data will be generated in MBEE and transmitted to the ICU through PBEE. Figure 3.3 illustrates the electronics architecture of the LAD.

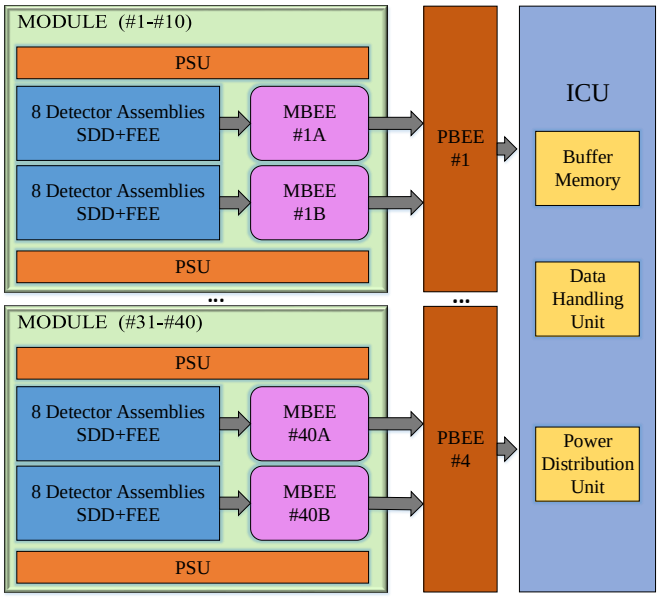

Figure 3.3: The electronics architecture shows the different hierarchical levels of electronics of the LAD: module's electronics (FEE, MBEE, and MPSU), PBEE, and ICU. The electronic structure of a detector module is shown in the black dotted box (Xiong *et al.*, 2025).

Besides the electronics design, many other elements should be taken into consideration in the LAD instrument design and implementation to optimize the performance. A robust array of mechanical frames ensures the precise alignment and stability of the instrument assembly. A lead shell is integrated to shield against the background radiation. An aluminum radiator facilitates effective heat dissipation from the detector modules, preventing thermal buildup and preserving optimal operating conditions. The reference provides details on the LAD instrument design and implementation (Zhang *et al.*, 2019).

3.2 Large Area Multi-Channel Silicon Drift Detector

The detector used in the LAD is the large area multi-channel SDD, specifically, it is called the ALICE-D4 SDD, originally developed for particle tracking in the ALICE experiment at the LHC (Campana *et al.*, 2011), and features 2-D imaging capability in a 1-D anode distribution detector, the principle of this kind of detector is shown in the

center Figure 3.4. The sensitive area of one detector is 11 cm × 7 cm with a thickness of 450 µm. Two series of 112 read-out anodes are located symmetrically at the two edges of the sensitive area. A negative high voltage of -1300 V is applied on its symmetry axis in the middle, which generates the electric field towards the symmetry axis. The distance between two adjacent anodes is called pitch, which is a critical parameter for the anode charge distribution, affecting the incident position reconstruction. The difference in this parameter of the detector between the LAD and WFM represents a key distinction between the two instruments. This difference dictates their respective functionalities: the WFM, with its incident position reconstruction ability, is well-suited for monitoring purposes, while the LAD is only applied for precise measurements of X-ray energy and timing.

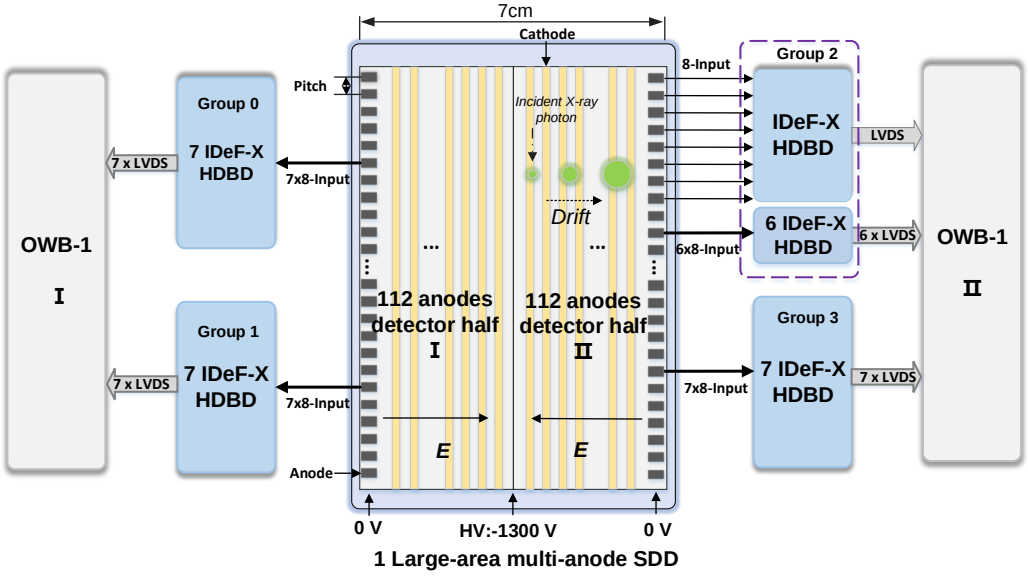

Figure 3.4: A large area multi-channel SDD is divided into two detector halves. In each half, two groups of 14 IDeF-X HDBD ASICs are used to process signals from the 112 anodes, sharing a single OWB-1 ADC. A negative high voltage of -1300 V is applied on the symmetry axis, creating the electric field from the edge where the anodes are located toward the axis (Xiong *et al.*, 2025).

For the large area multi-channel SDD and FEE simulator, the preliminary functionality is the ability to simulate the detection of single photon events. This process involves two key aspects: charge generation from energy deposition and charge distribution on the anodes after the electron drifts. Based on the capability to simulate single photon event detection, the simulator can be further expanded to encompass more complex scenarios like multiple-photon detection, then introduce the influence of the background radiation

and the noise of detector and electronics, enabling the establishment of a large area multi-channel SDD and FEE simulator that is more in line with real physical scenes.

Charge Generation from Energy Deposition

The mechanism of charge generation due to energy deposition has been described in detail in Section 1.2 in Chapter 1. When an X-ray photon interacts with the silicon material of the SDD, its energy is absorbed by the material of the SDD, and then electron-hole pairs are generated through the photoelectric effect. Equation (3.1) calculates the number of electron-hole pairs generated by the absorption of photons of a specific energy, as stated in Section 1.2.2 in Chapter 1.

$$N = \frac{E_{\text{photon}}}{\omega} = \frac{E_{\text{photon}}}{3.6\,\text{eV}} \tag{3.1}$$

Electron Cloud Drift

In the SDD, after generating electron-hole pairs, the holes are collected by the nearest electrode, while the electrons are rapidly focused onto the central plane of the detector and then drift toward the anode with a constant velocity when the temperature is stable. For large area multi-channel SDDs, electrons move along the electric field, drifting toward the anode array located at the edge of the detector.

During this drift, random thermal motion causes the electrons to diffuse, leading to a gradual expansion of the charge cloud. The shape of the electron cloud shows a Gaussian distribution (Crescio and Nouais, 2006; Campana *et al.*, 2011). As the electron cloud drifts, the charge density $\rho(\vec{r},t)$ can be expressed as:

$$\rho(\vec{r},t) = \frac{q}{2\pi\sigma^2(t)} e^{-\frac{(\vec{r}-\vec{r}_0(t))^2}{2\sigma^2(t)}} \tag{3.2}$$

where $\vec{r}_0$ is the cluster centroid of the electron cloud, q is total charge, and $\sigma(t)$ is the standard deviation of the electron cloud Gaussian distribution at time t, representing the size of the electron cloud. As the drift time increases, the size of the electron cloud $\sigma(t)$ also increases. The relationship between the size of the electron cloud $\sigma(t)$ and the drift time t can be expressed as:

$$\sigma(t) = \sqrt{2Dt + \sigma_0^2} \tag{3.3}$$

where D is diffusion coefficient and σ_0 is the initial size of the electron cloud. The diffusion coefficient can be expressed as:

$$D = \frac{k_B T}{q}\mu_e = \frac{k_B T v_D}{qE} \tag{3.4}$$

where k_B is Boltzmann constant, T is environment temperature, q is elementary charge and E is electric field and v_D is drift velocity, then the Equation (3.3) can be expressed as:

$$\sigma(t) = \sqrt{\frac{2k_BT}{qE}\chi_D + \sigma_0^2} \tag{3.5}$$

where χ_D is drift distance. Based on the above theory, it is possible to determine the spatial distribution of the electron cloud after it drifts a certain distance. The following three questions will be explored:

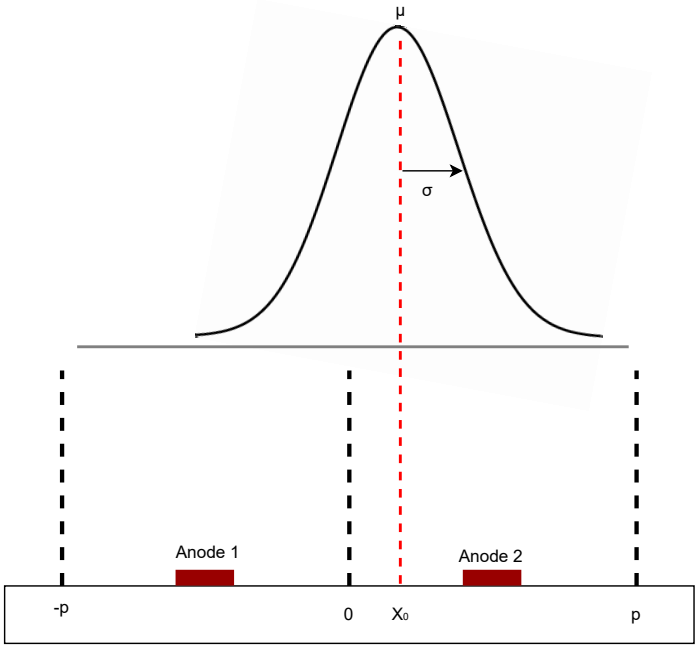

Figure 3.5: Schematic diagram of the drifted electron cloud being absorbed by different anodes. The upper part shows the charge distribution when the electron cloud reaches the anode array, and the lower part represents two adjacent anodes. The anode will absorb the charge drifting to the area between the two dotted lines.

(1) The amount of charge absorbed by different anodes:

Figure 3.5 illustrates a schematic diagram of the Gaussian-distributed electron cloud being absorbed by different anodes. There are two adjacent anodes separated by a pitch distance p. Each anode's "sphere of influence" extends to half of p on either side of its

center. This means that electrons within $p/2$ from the center of an anode will be absorbed by that anode. Therefore, the charge absorbed by **Anode 1** corresponds to the integral of the charge density function from $-p$ to 0:

$$Q_1 = \int_{-p}^{0} \rho(t_0, x)\, dx \tag{3.6}$$

Similarly, the charge absorbed by **Anode 2** is given by the integral of the charge density function from 0 to p:

$$Q_2 = \int_{0}^{p} \rho(t_0, x)\, dx \tag{3.7}$$

$\rho(t_0, x)$ in Equation (3.6) and Equation (3.7) means the charge density when the electron cloud arrives at the anodes, which can be expressed by Equation (3.8)

$$\rho(t_0, x) = \frac{q}{2\pi\sigma^2(t_0)} e^{-\frac{(x-x_0)^2}{2\sigma^2(t_0)}} \tag{3.8}$$

where t_0 represents the total drift time it takes from the electron cloud's generation to its absorption by the anodes. Combining Equation (3.6) - Equation (3.8), the amount of charge absorbed by the two anodes can be calculated separately.

(2) Incident position reconstruction:

According to Figure 3.5, the mean value (μ) of the Gaussian distribution reflects the X-coordinate of the incident position, and the X axis is parallel to the edge where anodes are located. As the electron cloud expands with the drift distance increasing, the size of the electron cloud when reaching the anode array varies depending on the drift distance. By analyzing the distribution of electron clouds absorbed by the anode array, we can obtain the size of the electron cloud at the point of absorption, and then the drift distance can be inferred. Subsequently, the Y-coordinate can be calculated, which lies along the drift direction.

X coordinate: If the Gaussian distribution of the electron cloud at the moment of absorption by the anode array could be accurately determined, the X-coordinate could be calculated with perfect precision. However, obtaining this distribution is highly challenging. Instead, the discrete charge distribution is used to approximate the X-coordinate. This is achieved by weighting the charges collected by different anodes, calculating their centroid coordinates, and using this centroid as an approximation of the X-coordinate (Crescio and Nouais, 2006) as shown in Equation (3.9):

$$x_{\text{incident}} = \frac{(-p/2)Q_1 + (p/2)Q_2}{Q_1 + Q_2}. \tag{3.9}$$

This calculated value differs from the true incident X-coordinate, corresponding to the Gaussian distribution's mean value. Similar to the principle of integration, as the pitch between adjacent anodes decreases, the X-coordinate calculated with this method

becomes increasingly accurate; however, a smaller pitch results in less charge being collected by each anode. Consequently, background noise becomes more significant in the measurement of smaller signals. Additionally, increasing the anode density raises the complexity of the readout circuit, leading to higher costs.

Y coordinate: To obtain the coordinate of the X-ray photon's incident position along the drift direction, it is appropriate to calculate the σ value of the charge distribution at the point of absorption by the anode array based on Equation (3.5). According to Equation (3.6) - Equation (3.8), this requires numerical simulation using modeling software to replicate the charge distribution on the anode array at various drift distances. By analyzing these simulated distributions, the corresponding value can be extracted, allowing the drift distance to be reconstructed. (Campana *et al.*, 2011) provides a comprehensive description of the detailed process of position reconstruction.

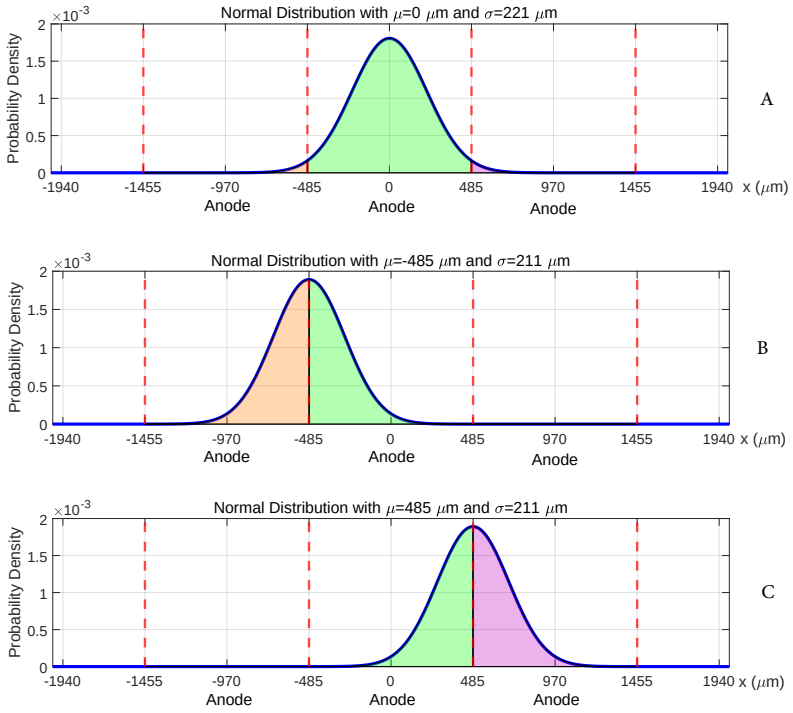

Figure 3.6: The distribution of the electron cloud on the anodes after drifting the maximum distance (3.5 cm) in the LAD at different incident horizontal coordinates (μ). Three anodes are located on the -970 μm, 0 μm, and 970 μm. The orange, green, and pink areas represent the charge absorbed by each of the three anodes. It can be concluded that there are no more than three anodes involved in absorbing the electron cloud (Xiong *et al.*, 2025).

(3) Type of events in LAD detection:

The number of anodes involved in absorbing the electron cloud depends on the size of the electron cloud and the pitch between adjacent anodes. The size of the electron cloud is determined by its drift distance. Therefore, the event type in the LAD, defined by the number of anodes participating in electron cloud absorption, can be inferred by analyzing the maximum drift distance and pitch parameter of the large area multi-channel SDD in the LAD. The length of the sensitive area along the drift direction is 7 cm, which means the maximum drift distance is 3.5 cm. Considering Equation (3.5), the maximum σ of the electron cloud can be calculated. The high voltage applied in the LAD detector is 1300 V, therefore, the electric field can be calculated, yielding $E \approx 370$ V/cm. When $T = 300$ K, $k_B T/q = 0.0259$ V, $\sigma_0 = 20$ µm, which represents the initial size of the electron cloud, and χ_D is the maximum drift distance of 3.5 cm, then the maximum σ can be calculated to be 221 µm, representing the maximum size of the electron cloud. Figure 3.6 illustrates the distribution of the electron cloud on the anodes after completing the maximum drift distance with different incident horizontal coordinates (μ). The pitch of the detector used in LAD is 970 µm, and the areas with different colors mean the charge amount that is aborted by different anodes. It can be inferred that an X-ray event in the LAD involves at most three adjacent anodes.

The primary distinction in the detection chain design between the WFM and LAD is the WFM's requirement for position reconstruction. The WFM applies a detector with a smaller pitch of 294 µm to achieve this. This configuration enables a position resolution of approximately 20 µm along the anode distribution direction (X-coordinate) (Ceraudo *et al.*, 2024a). The difference in pitch between the LAD and WFM results in varying detection channel densities, which leads to different designs for the associated electronics and data processing methods, but the working principle of the detection chain remains consistent across both the LAD and WFM.

3.3 Front End Electronics

The Front-End Electronics (FEE) serves to convert, amplify, shape, and digitize the charge signals collected by the detector anodes. The FEE is implemented by using two Application Specific Integrated Circuits (ASICs): IDeF-X HDBD (Gevin *et al.*, 2012; Baudin *et al.*, 2022) and OWB-1 (Bouyjou *et al.*, 2017). IDeF-X HDBD comprises 32 analog channels, and each channel has an identical structure including a charge sensitive amplifier with a continuous reset system, an adjustable gain stage, a pole-zero cancellation stage, a low-pass filter with an adjustable shaping time, a baseline holder, and a peak detector with a discriminator. OWB-1 is a 13-bit, 32-channel (16-differential channel) Analog-to-Digital Converter (ADC) with a maximum conversion time of 2.56 µs and a 2 V input range, based on an improved Wilkinson architecture (Wilkinson, 1950; Schumann and McMahon, 1956).

To achieve an accurate simulation of the behavior of the detector and FEE, it is essential to make it clear and describe both of them structurally and functionally. This will

enable the design of a simulator that closely replicates the behavior and output of the detector and FEE.

3.3.1 Structure of a Detector and its FEE

Figure 3.4 presents the structure of one large area multi-channel SDD and its dedicated FEE. A detector comprises 224 anodes located on its two side edges, and each detector is divided into two halves referred to as detector halves. Each detector half, containing 112 anodes, requires 112 readout channels. Due to the large anode pitch in the LAD detectors, for a much easier installation and welding, eight channels are selectively chosen and used from the 32 channels in one IDeF-X HDBD. Among these eight channels, the distance between two adjacent channels is basically the same as the pitch of the LAD detector. The unused channels can be disabled without increasing the system's power consumption.

This configuration results in each detector half requiring 14 IDeF-X HDBDs for readout. Based on the IDeF-X HDBD design principles, a slow control interface can be shared by one group of eight IDeF-X HDBDs for ASIC configuration, triggered ASIC map (distribution of triggered IDeF-X HDBDs), and triggered anode map (distribution of triggered anode channels in the triggered IDeF-X HDBDs) acquisition, which will be introduced in detail in Chapter 4. Each IDeF-X HDBD within the same group is assigned a unique address, represented as a three-bit binary code, to distinguish it from others. Since the OWB-1's configurable input can support 16 differential inputs, every two groups of 14 IDeF-X HDBDs share a single OWB-1. All data from this OWB-1 is processed through the same data processing pipeline. This design implies that when certain anodes on a detector half are triggered, the entire detector half enters a state where it cannot detect additional potential events, effectively resulting in a temporary detection dead time. In one IDeF-X HDBD, there is only one analog signal output port, responsible for sequentially outputting signals from all anode channels to the input port of OWB-1 for analog-to-digital conversion; therefore, a critical aspect of the IDeF-X HDBD operation is that the digitization of each anode signal is conducted serially. The implications of this sequential digitization on the system's dead time will be discussed in Chapter 4.

3.3.2 Key Considerations for the Simulation of IDeF-X HDBD

In the IDeF-X HDBD simulation, several key aspects should be considered. The primary focus is to simulate the energy distribution of the anodes involved in charge absorption within the detector, which involves two critical components: the relationship between the incident X-ray photon energy and the signal peak value obtained from the peak extraction circuit, and the position distribution information of the triggered anodes in this detector half, identifying which IDeF-X HDBD is triggered and which specific anodes within it are involved in the electron cloud absorption. Achieving this requires a thorough analysis

of the circuit structure to have a clear understanding of the readout channel's architecture. Furthermore, parameters such as gain and threshold are essential for acquiring this information, and their adjustment requires modifying the corresponding registers, which will be illustrated. IDeF-X HDBD modifies ASIC parameters by changing the value of a certain register through the slow control interface, which is also the interface to generate the triggered ASIC map and triggered anode map. Simulating these processes is important for the detector-FEE simulation. In this part, some of the information comes from the datasheet of IDeF-X HDBD from the French Alternative Energies and Atomic Energy Commission (CEA) team.

Structure of Readout Channel of IDeF-X HDBD

Figure 3.7 shows the structure of the readout channel. The first stage is a charge sensitive amplifier, which is used to collect the charge, convert it to a voltage signal, and perform the first amplification to suppress the relevant noise as much as possible. The gain of the charge sensitive amplifier is usually defined as the ratio of the output voltage to the input charge, as shown in Equation (3.10):

$$A = \frac{V_{\text{out}}}{Q_{\text{in}}} = \frac{1}{C_f} \tag{3.10}$$

where A is the charge sensitive amplifier's gain, with a unit of V/C (volts per coulomb); Q_{in} is input charge, with a unit of C (coulomb); and V_{out} is the output voltage of the charge sensitive amplifier, with a unit of volt.

In the current version of the IDeF-X HDBD, the value of the feedback capacitor of the charge sensitive amplifier is 50 fF (Baudin *et al.*, 2022), therefore, the gain of the charge sensitive amplifier stage can be calculated:

$$A = \frac{1}{C_f} = \frac{1}{50 \times 10^{-15}} = 2 \times 10^{13}\,\text{V/C} \tag{3.11}$$

It describes the relationship between input charge and output voltage: If the input charge is $Q_{\text{in}} = 0.5\,\text{fC}$, the output voltage is:

$$V_{\text{out}} = Q_{\text{in}} \times A = (0.5 \times 10^{-15}) \times (2 \times 10^{13})\,\text{V} = 10\,\text{mV} \tag{3.12}$$

In other words, if a signal generator simulates the detector's output, a 10 mV input signal to the charge sensitive amplifier can be equivalent to a 0.5 fC charge injection.

The second stage is an adjustable gain stage, and the current version of IDeF-X HDBD can achieve three gain settings: 50 mV/fC ,100 mV/fC , and 200 mV/fC.

The pole-zero cancellation stage is a specialized filter designed to eliminate signal overshoot, thereby enhancing the SNR and improving system stability. Following this, an RC^2 low-pass filter is applied to adjust the signal shaping time, effectively suppressing high-frequency noise. The peak time is a parameter that describes the signal shaping

time, reflecting the low-pass filter's configuration characteristics. Generally, increasing the shaping time enhances the filter's ability to suppress high-frequency noise and smooth the signal more effectively. However, it will reduce the amplitude of the signal and increase the width of the signal, therefore increasing the risk of signal pile-up. In the current version, the peak times can be set from 0.73 µs, up to 10.73 µs. Together, these two stages represent the processing of the frequency domain signal within the read-out channel, aiming to reduce the noise and further optimize the SNR.

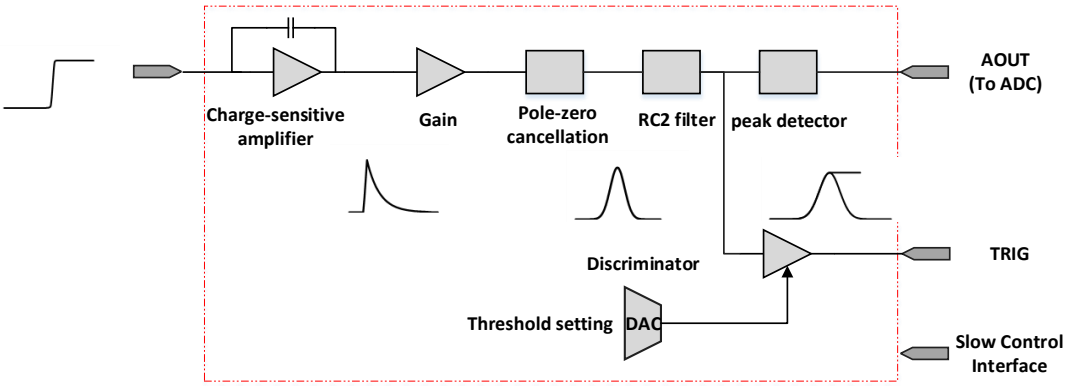

Figure 3.7: This diagram illustrates the signal processing chain of a readout channel in IDeF-X HDBD. The input signal is first processed by the charge sensitive amplifier and converted into a voltage signal. The signal is then amplified by a gain stage, followed by a pole-zero cancellation circuit to suppress overshoot. An RC^2 filter is applied to shape the signal and reduce high-frequency noise, after which the peak detector extracts the signal's maximum value. Simultaneously, a discriminator compares the signal's amplitude to a threshold set by a DAC, generating a trigger signal (TRIGGER) when the threshold is exceeded. The final output (AOUT) is sent to the ADC for digitization. The slow control interface is mainly used for configuration and status monitoring.

Next, the peak extraction circuit is employed to capture the maximum value of the signal. The analog output AOUT of the IDeF-X HDBD does not provide the actual signal waveform but instead outputs its maximum value. Simultaneously, the DAC generates a threshold value based on a preset configuration. The peak value of the signal is then compared with this threshold by the discriminator. If the peak value exceeds the threshold, a trigger signal TRIGGER is generated, initiating subsequent operations in other parts of the module's electronics, which will be described in Chapter 4. The slow control interface is used for the IDeF-X HDBD configuration and gets the current value in the register for a certain parameter. When IDeF-X HDBD detects an event, the triggered ASIC map and the triggered anode map are also transmitted through this interface. The channel baseline is adjusted by the baseline holder to maintain a stable baseline level to

compensate for changes in the detector leakage current. For more details on the features and the principle of the IDeF-X HDBD, please refer to (Gevin *et al.*, 2012; Baudin *et al.*, 2022).

Relationship between X-ray Energy and Output Signal Peak

In this section, we will establish the relationship between incident photon energy and the peak value of the output signal. The calculation consists of two main steps. The first step is converting the energy of the X-ray photon into the charge amount, and the second step maps this charge to the signal amplitude. This process requires a combination of the charge generation from energy deposition in Section 3.2 and the total gain of IDeF-X HDBD mentioned in this section. We use X-ray photons with specific energies as an example to intuitively demonstrate the relationship between the energy of the incident X-ray photon and the output signal peak after energy deposition, charge signal conversion, amplification, and shaping in the readout channel. Assuming an incident photon with an energy of 10 keV interacting with the silicon detector with an average ionization energy of 3.6 eV, the number of electron-hole pairs generated can be calculated using Equation (3.1), which is approximately 2778. This corresponds to an initial electron cloud charge of 0.4448 fC. As previously mentioned, the charge sensitive amplifier converts the charge signal into a voltage signal but does not provide real amplification. The signal gain in the IDeF-X HDBD readout system is entirely determined by the gain stage. With a default gain of 200 mV/fC, the peak amplitude of this signal from the readout channel is calculated to be 89 mV.

Parameters of Readout Channel

The circuit parameters involved in IDeF-X HDBD signal reading will be briefly introduced in this section, and an analysis is provided of which parameters need to be considered in the detector-FEE simulation design process. First, the gain and the peak time have already been discussed above. Another critical parameter for X-ray event identification and energy reconstruction is the threshold of each channel. When the signal peak of a channel exceeds the preset threshold, a trigger signal is generated immediately. To prevent false triggering caused by the dark current or noise, setting an appropriate threshold is necessary. Only anode channels with signal peaks surpassing the threshold are considered triggered, and the presence of triggered channels indicates a triggered ASIC. Additionally, various related parameters can be adjusted, such as the power supply mask, which controls the power on or off of the channels. This feature is particularly necessary for the LAD, as only eight channels are used; the other 24 channels can be powered off. However, in the simulation of the detector-FEE, the gain and threshold are the most critical parameters.

3.3.3 Key Considerations for Simulation OWB-1

In the operation of OWB-1, the main focus is on controlling its workflow and accurately acquiring the sampled data. To achieve this, the following processes need to be considered: configuring the working mode and parameters of OWB-1; managing and controlling its workflow, including precise clock calibration, initiating and ending analog-to-digital conversion, and handling data storage and transmission; and implementing the analog-to-digital conversion process to obtain sampled data. In the initial stage, the primary objective of simulating OWB-1 is to acquire data and use it to develop the data processing pipeline. Thus, our attention will be centered on two key aspects: understanding the relation between input voltage and output data, and how to transmit output data. Therefore, these considerations will be presented in conjunction with an explanation of OWB-1's working principle when simulating the behavior of the OWB-1. In this part, some information comes from the datasheet of the OWB-1 from the CEA team.

Operating Principles and Key Features of OWB-1

OWB-1 is a 32-channel single slope ADC based on an improved Wilkinson architecture, with a 13-bit resolution, a conversion time of 2.56 μs, and a 2 V input range. Figure 3.8 shows the working principle of OWB-1. This working principle is similar to the vernier caliper and the X-ray time recording technique, which will be described in Chapter 4. To increase resolution, a Delay-locked loop (DLL) performs time interpolation, which is a key module in OWB-1 for high-precision measurement of the input voltage. Specifically, it subdivides the master clock cycle (10 ns) into 32 equally spaced time steps through a DLL, each time step corresponds to a resolution of 312.5 ps, and encodes the result in 5-bit binary form for output. This operation increases the ADC resolution by 5 bits compared to the standard single-ramp architecture, without adding to power consumption or conversion time.

There are two counters used to record the value of the input signal. The first one, the Gray counter, is an 8-bit counter driven by a 100 MHz Phase-locked loop (PLL) clock. It starts counting when the ramp voltage (V_{RAMP}) begins to rise from zero, with a ramp duration of 2.56 μs and a clock period of 10 ns. The counter's maximum value is 256, corresponding to an 8-bit range. When the input voltage and ramp voltage are equal, the Gray counter stops, latching the current 8-bit Gray code count. Simultaneously, the DLL encoder is triggered to begin to count, driven by the DLL clock, until the next master clock edge arrives, at which time the DLL encoder latches the current count value, indicating the relative position of the trigger moment within the current master clock cycle. Due to the fine resolution of the DLL encoder, the entire ADC system can add 5 bits of resolution to the 8-bit coarse time measurement of the main counter, thereby achieving a total of 13 bits of time digitization accuracy. In addition, the DLL encoder only works from the moment when the input voltage and the ramp voltage are equal to the moment when the next master clock edge comes, so it has the characteristics of low

power consumption.

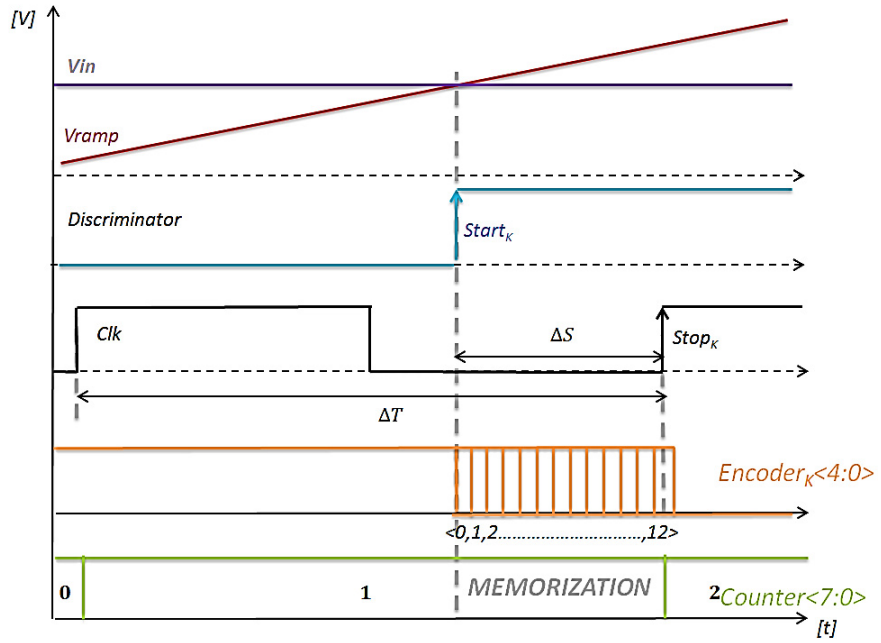

Figure 3.8: The working principle of OWB-1 sampling - two clocks work together to achieve a 13-bit resolution (Bouyjou *et al.*, 2017).

Many features of OWB-1 are determined by its work principle. For example, the initial value and maximum value of the ramp voltage generator determine the dynamic range of the ADC, while the slope of the ramp voltage influences the conversion time, and the relationship between the two counters and the two clocks determines the resolution of the ADC. OWB-1 provides two data reading modes, including serial mode (Low-Voltage Differential Signaling, LVDS) and parallel mode (Complementary Metal-Oxide-Semiconductor, CMOS). The serial mode performs serial data transmission through a single pair of lines, while the parallel mode outputs data simultaneously through 11 CMOS pins, which is suitable for higher data transmission rate requirements. It supports three rates: 25 MHz, 50 MHz, and 100 MHz. In serial mode, data is transmitted through a single LVDS channel, and the rate is limited by the selected clock frequency; in parallel mode, data is transmitted simultaneously through multiple CMOS pins, and the transmission rate is higher. Users can choose the appropriate reading frequency and mode according to the application scenario requirements to achieve a balance between transmission rate, power consumption, and anti-interference ability. For each OWB-1, there are 32 input channels, and these 32 channels can also be configured as 16 pairs of LVDS inputs, which is called differential mode. In differential mode, the input signal of each channel consists of two pins, and the differential voltage determines the final input

value. For detailed information about the working principle of OWB-1, please refer to (Bouyjou *et al.*, 2017).

Relationship between the Input Voltage and the Output Data of OWB-1

As an ADC, its purpose is to convert analog signals into digital signals, so it is very important to make clear the relationship between the input signal and the output data. Factors that affect this relationship include the dynamic range of the ADC, the output data corresponding to the ADC's 0 V input signal, and the resolution of the ADC. According to the datasheet of OWB-1, the dynamic range of the OWB-1 input signal is from 0.84 V to 2.84 V. When the input signal is outside this range, the output data is 0. As mentioned before, the output data consists of two parts: the 8-bit count value of the Gray counter and the 5-bit count value of the DLL encoder. Their results will be stored in the corresponding registers, which will be introduced in the next section. The relationship between the input voltage and the output data is shown as Equation (3.13):

$$V_{\mathrm{IN}} = V_{\mathrm{INIT\_RAMP}} + \text{Digital Output} \times \frac{V_{\mathrm{RAMP}}}{2^{13}} \tag{3.13}$$

where V_{IN} is input voltage, $V_{\mathrm{INIT\_RAMP}}$ is the initial value of the ramp voltage generator, whose value is 0.84 V, V_{RAMP} is the dynamic range of the OWB-1, whose value is 2 V and Digital Output is the output data.

Format and Mode of Transmitted Data

In this section, we will combine the actual use mode of OWB-1 in the FEE of the LAD and the features of OWB-1, especially the characteristics of data transmission, to describe another important consideration in OWB-1 simulation. First, as mentioned before, each OWB-1 is responsible for reading out the output of two groups of 14 IDeF-X HDBDs by using 14 of the 16 LVDS input pairs of OWB-1 (the other 2 pairs of LVDS input ports of OWB-1 are left floating). As for the output, the serial LVDS output mode is used in the data transmission. In the initial design stage, to meet the subsequent timing requirements, the transmission speed is configured to 25 MHz, which will reduce the stress brought by the timing control, however, this configuration will increase the dead time, as will be mentioned in Section 4.3 of Chapter 4. According to the datasheet of OWB-1, for each channel (single-end or LVDS channel), there are two registers to store the values of the Gray counter and DLL encoder, as well as the address of this channel. Top register is an 11-bit register to store the Gray counter value (the lowest 8 bits are used), while another register, called Bottom register, is an 11-bit register to store the value of the DLL encoder (5-bit) and 5-bit channel address (the lowest 10 bits are used). During the transmission process, the transmission is gradually carried out from the large channel to the small channel. For example, the data of Bottom register and Top register of the 16th differential channel are transmitted in sequence first. For each register, the

transmission starts from the highest bit to the lowest bit, and then the 15th differential channel is transmitted. After finishing the transmission of the data of the 16 differential channels, an 11-bit register (the lowest 3 bits are used) is transmitted separately to record the address of OWB-1. For the transmission process, each register is separated by a single bit 0. The data transmission rate is based on the frequency of the output synchronization clock, which is 25 MHz. Similar to Equation (3.13), we use the data of two registers here to accurately represent the corresponding input voltage, as shown in Equation (3.14):

$$V_{\mathrm{IN}} = V_{\mathrm{INIT\_RAMP}} + (\mathrm{GrayToBin}(\mathrm{TOP\_REGISTER}\langle 7:0\rangle), (\mathrm{BOTTOM\_REGISTER}\langle 10:6\rangle)) \times \frac{V_{\mathrm{RAMP}}}{2^{13}} \tag{3.14}$$

The definitions of the relevant parameters are the same as Equation (3.14).

In this chapter, we introduced the structure of the LAD payload in detail and focused on introducing the unique detection unit — the detector module and its electronics architecture to deal with its large number of large area multi-channel SDDs. In addition, we sorted out the detection chain of LAD, focusing on the large area multi-channel SDD and the FEE based on two kinds of ASICs. This content is the theoretical foundation for the construction of the FEE simulator.

Chapter 4

Module Back End Electronics

The Module Back-End Electronics (MBEE), representing the first hierarchical level of the Back-End Electronics system, is responsible for recording time information and performing energy reconstruction from digitized signals of the X-ray event. It is a digital circuit built with an FPGA chip, with interfaces to other circuits on one MBEE board: 8 FEE interfaces, an MPSU interface, and a PBEE interface. Additionally, a specialized housekeeping (HK) circuit is integrated into the MBEE to monitor electronics' parameters. All of these parts make the MBEE play a critical role in the control, configuration, and monitoring of the module's electronics and various types of data transmission. The VHDL-based FPGA program is pivotal in enabling these functionalities. This chapter provides a detailed description of the MBEE's development process, focusing on task requirements, design considerations, and implementation procedures, as well as the architecture and implementation of the FPGA program. Basic functional tests and analyses were conducted to verify the MBEE's operational capabilities, providing a robust foundation for the subsequent system development and testing phases. Some of the parts in this chapter are based on the content presented in the journal article authored by me as the first author. For further details, see (Xiong *et al.*, 2025).

4.1 Development of the MBEE Hardware

4.1.1 MBEE Tasks

The tasks of the LAD MBEE include:

- **Time tagging**: As a timing spectrometer, it is crucial to record the occurrence time of the X-ray event accurately. Once a trigger signal is received, the MBEE tags the time of the event based on its timing system.

- **Energy reconstruction**: X-ray energy reconstruction, as the most important function of the MBEE, is achieved through the data processing pipeline. This process involves pedestal subtraction, common mode noise subtraction, calibration, energy reconstruction, energy identification, and data packaging if the event meets the criteria as a valid event.

- **MPSU control**: MPSU generates High Voltage (HV) and Medium Voltage (MV) for the operation of the large area multi-channel SDDs. The enabling/disabling, setting, and control of ramp-up/ramp-down of these voltages depend on the control of the MBEE.

- **Detector module electronics status monitoring**: The monitoring of the detector module electronics status is dependent on the housekeeping circuit of the MBEE, which measures parameters such as voltages, currents, and the temperatures of the system. When any of these values exceed the predefined safe thresholds, the system automatically switches to safe mode to prevent potential damage.

- **Detector module electronics configuration**: The electronics configuration involves the setup of the IDeF-X HDBD and OWB-1 on the FEE, and the adjustment of MBEE's parameters to accommodate different engineering operation requirements.

4.1.2 MBEE Hardware Structure and Design

The hardware design of the MBEE is driven by the tasks of the MBEE and the requirements of the operating environment, such as mechanical, thermal, and radiation environments.

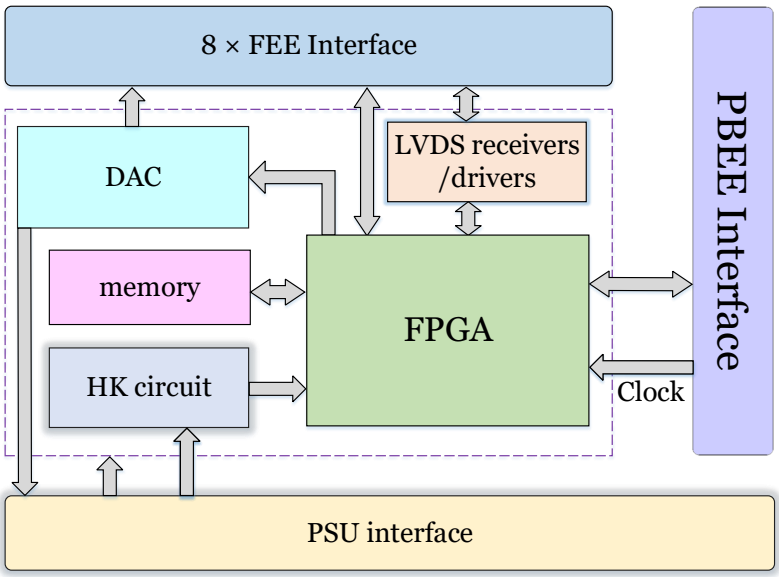

Figure 4.1: The structure of the LAD MBEE (Xiong *et al.*, 2025).

Figure 4.1 illustrates the structure of the MBEE. The MBEE includes several key components: the data processing and electronics control unit — FPGA and its configuration circuit, FEE interfaces, PBEE interface, MPSU interface, and housekeeping circuit. Due to export control restrictions, a strict requirement for every component of the eXTP mission is to demonstrate its feasibility using ITAR (International Traffic in Arms Regulations) -free components to facilitate export to the launch site in China. In addition, key factors in device selection include its radiation resistance, wide operating temperature range, and relatively simple operating interface, all of which contribute to the reliability and stability of the MBEE.

FPGA and its Configuration Circuit

The NG-MEDIUM FPGA NX1H35ASN, a radiation-hardened FPGA manufactured by the European company NanoXplore® specifically for space applications, was selected as the central component of the MBEE. This FPGA features 374 I/O pins, supporting multiple I/O standards, including LVDS and LVCMOS (Low-Voltage Complementary Metal-Oxide-Semiconductor) I/O standards. To conserve I/O resources, the 3.3 V LVCMOS standard was chosen for most I/O operations. However, due to the extensive use of LVDS signals in the FEE ASICs, external LVDS transceivers are required to convert LVDS signals to single-ended signals. For this purpose, quad-channel radiation-hardened drivers (RHFLVDS31A) and receivers (RHFLVDS32A) from STMicroelectronics® are selected for output and input signals, respectively. Both the driver chip and the receiver chip operate at 3.3 V with a power consumption of 55 mW per channel. In addition, transceivers can be disabled when not in use to reduce power consumption. To store bitstream files, the radiation-hardened 128 Mbit PROM 3DFS128M01VS2728 from 3D Plus® was selected, providing a secure and stable repository for the critical configuration data required by the FPGA, leveraging SPI NOR Flash technology for non-volatile storage. More importantly, its TMR (Triple Modular Redundancy) architecture (Lyons and Vanderkulk, 1962) can improve reliability in radiation environments.

Table 4.1: Low Voltages in the Detector Module

Voltage	Description
1.2 V	Core supply of the FPGA
2.5 V	Auxiliary supply for the FPGA
3.3 V(Digital)	Digital I/O supply for the FPGA, the digital supply for the OWB-1 and IDeF-X HDBD
3.3 V(Analog)	Analog supply for the DAC and ADC, the analog supply for the OWB-1 and IDeF-X HDBD

MBEE-MPSU Interface

The MPSU interface establishes the connection between the MBEE and the MPSU, and the latter generates three types of voltages: High Voltage (HV), Medium Voltage (MV), and Low Voltage (LV). As no MCU (Microcontroller Unit) or FPGA will be implemented on the MPSU board, the MBEE will control and configure HV and MV generated on the MPSU. Similarly, there will be no monitoring circuit on the MPSU board, therefore, all parameters of the MPSU will be monitored by the MBEE. The following specifies the electrical interface between MBEE and the MPSU.

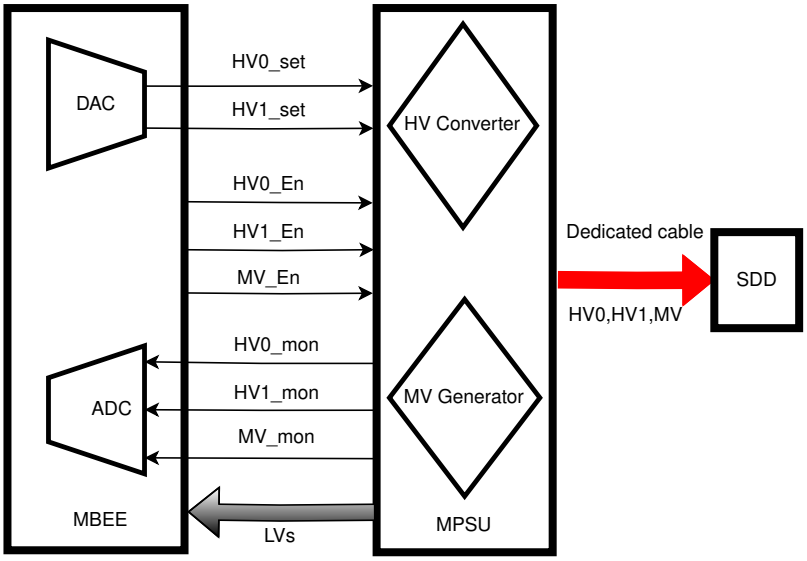

Figure 4.2: The schematic diagram of the MBEE-MPSU interface.

- **LV**: There are a total of four different voltage rails required in the detector module, as shown in Table 4.1.
- **HV**: HV is applied for detector operations. The electrons generated by the interaction between X-rays and the large area multi-channel SDD drift along the electric field, which is produced by the HV, and form an electron cloud. The HV is generated by a dedicated converter on the MPSU and outputs to the detector. The MPSU's HV converter provides a setting line and a monitor line connected to the MBEE. A dedicated cable delivers the HV output directly from the MPSU to the detector, with no routing through the MBEE and FEE.

  HV control (V_{set}): The DAC on the MBEE will generate an analog voltage V_{set} to set the output voltage of the HV converter. Equation (4.1) illustrates the relationship between the HV converter output and the output voltage value of the DAC on the MBEE:

$$HV_{out} = -V_{set} \times 1000 \tag{4.1}$$

It is important to emphasize that when turning on and off the HV, the DAC does not directly output the target value. Instead, a ramp-up/ramp-down process is applied to increase or decrease the voltage gradually. This method minimizes the risk of sudden voltage fluctuations in the MPSU, which could otherwise compromise the system's stability. The ramp-up and ramp-down slopes in the MPSU are set to 50 V/s. This process is implemented through the FPGA program.

HV monitor (V_{mon_HV}): An analog voltage V_{mon_HV} is provided by the MPSU to monitor the value of the HV. This analog voltage will be input to the ADC of the housekeeping circuit, which will be discussed in the following section. Equation (4.2) illustrates the relationship between the HV converter output and the analog voltage input to the ADC:

$$V_{mon\_HV} = -\frac{HV_{out}}{1000} \tag{4.2}$$

HV Enable/Disable (HV_{EN}): The minimum programmable V_{set} may slightly deviate from 0 V. To ensure operational safety, the MPSU enforces protective measures that prevent the MBEE from applying any voltage settings that could potentially damage the detector. To fully disable the HV output and achieve an exact 0 V, the MPSU offers an active-low enable input compatible with LVCMOS 3.3 V. The MPSU ensures that the HV is not inadvertently activated during the power-on phase of the MBEE, particularly when the FPGA has not yet been configured.

- **MV**: The negative MV for the large area multi-channel SDD is a fixed value voltage that doesn't require an analog control signal (Zwart *et al.*, 2022). Similar to the HV, the MPSU provides an analog monitor voltage and a digital enable/disable signal to control the MV. The MV output voltage is supplied directly from the MPSU to the detector via a dedicated cable, bypassing the MBEE and FEE.

  MV monitor (V_{mon_MV}): An analog voltage V_{mon_MV} is provided by the MPSU for the monitor of the MV in the MBEE. Equation (4.3) illustrates the relationship between the MV output and the analog voltage:

$$V_{mon\_MV} = -\frac{MV_{out}}{100} \tag{4.3}$$

  MV Enable/Disable(MV_{EN}): For safety reasons, the MV also requires an enable/disable interface. To completely disable the MV output, the MPSU provides an active-low enable input compatible with LVCMOS 3.3 V. The MPSU ensures that the MV is not inadvertently activated during the power-on phase of the MBEE, particularly when the FPGA has not yet been configured.

Figure 4.2 presents a simplified interface diagram between the MBEE and MPSU.

MBEE-PBEE Interface

Data transmission between the MBEE and PBEE is implemented through the PBEE interface, serving the data exchange such as telecommands, their corresponding responses, and science data. The data exchange is carried out through a Universal Asynchronous Receiver-Transmitter (UART) protocol. Additionally, the clock system is distributed through this interface, with two LVDS clocks provided from the PBEE side. A Micro-D 9-pin connector is used for the PBEE-MBEE interface (see Figure 4.3 and Table 4.2). The electrical properties of each signal are compliant with the LVDS standard, where "P" represents the positive and "N" represents the complementary signal of the differential pair.

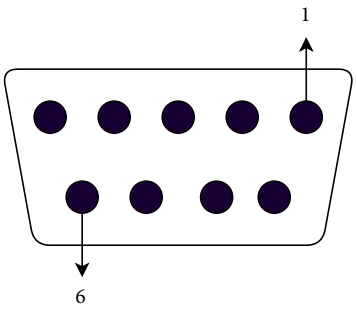

Figure 4.3: The schematic diagram of the MBEE-PBEE interface on the MBEE side.

Table 4.2: Pin Configuration in MBEE-PBEE Interface

Pin	Signal Name	Pin	Signal Name
1	TX_P	6	TX_N
2	RX_P	7	RX_N
3	GND		
4	PPS_P	8	PPS_N
5	10MHz_P	9	10MHz_N

10 MHz High Accuracy Clock (10MHz_P/N): This clock is provided by the ICU and distributed by the PBEE to the MBEEs, serving as the system clock for the MBEE and the microsecond information of the time tagging.

1 Pulse-Per-Second (PPS_P/N): The PPS signal, provided by the ICU and distributed by the PBEE to the MBEEs, has a frequency of 1 Hz with an active-low pulse duration of 1 ms and a rise/fall time of less than 100 ns. The signal jitter is maintained below

1 µs when the Global Navigation Satellite System (GNSS), such as GPS (Global Positioning System) and Beidou System, is available, and the timing error shall not exceed 0.5 seconds per day. The PPS is used for the absolute time record (second information) of time-tagging event timestamps.

Data (RX_P/N, TX_P/N): A full-duplex asynchronous interface has been implemented to simplify the harness and connectors. Data from the MBEE is transmitted through the receive channel (RX_P/N), while data from the PBEE to the MBEE is transmitted via the transmit channel (TX_P/N).

MBEE-FEE Interface

The FEE interface serves as the critical part for data exchange between the FEE and the MBEE, enabling smooth communication and control of various processes. In general, the FEE interface includes the IDeF-X HDBD interface, OWB-1 interface, DAC interface, and power interface for the power supply to the FEE. For the IDeF-X HDBD, an interface similar to the Serial Peripheral Interface (SPI) is used to implement two key functions: slow control and event reading.

- **Slow control of IDeF-X HDBD**: This function allows for the adjustment of IDeF-X HDBD parameters by modifying its internal values of these registers. Through slow control, parameters such as threshold, gain, or timing delay can be fine-tuned, ensuring the IDeF-X HDBD operates optimally for the specific X-ray detection environment. The three LVDS signals STROBE, DOUT, and DIN function similarly to the serial clock (SCLK), data output (MISO), and data input (MOSI) signals in the SPI protocol. In the slow control process, these signals are used to configure (write) and retrieve (read) specific registers in an IDeF-X HDBD:

  STROBE: Acts like the clock signal in SPI, coordinating the timing of data transmission.

  DOUT: Functions as the data output line, transmitting data from the IDeF-X HDBD to the MBEE during read operations.

  DIN: Functions as the data input line, enabling configuration data to be written from the MBEE to the IDeF-X HDBD.

  In the LAD, every seven IDeF-X HDBDs share a common set of slow control signals, and each IDeF-X HDBD is distinguished by assigning a unique address represented by three binary bits. Within each FEE interface, there are four independent sets of slow control signals. This design allows the interface to manage communication with up to 28 IDeF-X HDBDs in total.

- **Event Reading of IDeF-X HDBD**: In the event reading process, besides the three signals mentioned above, a dedicated LVDS signal TRIGGER is used to generate a trigger signal. Every seven IDeF-X HDBDs share a common TRIGGER signal;

therefore, there are four TRIGGER signals in an FEE interface. When a channel surpasses the threshold, TRIGGER signal will be activated, initiating event reading. First, TRIGGER signal will generate a triggered ASIC map to tell the MBEE which IDeF-X HDBD(s) is/are triggered. Then, DOUT signal is responsible for sequentially transmitting the anode trigger status from all triggered IDeF-X HDBDs. The triggered anode map is generated during this process and provides the MBEE with the information on which anodes have been activated.

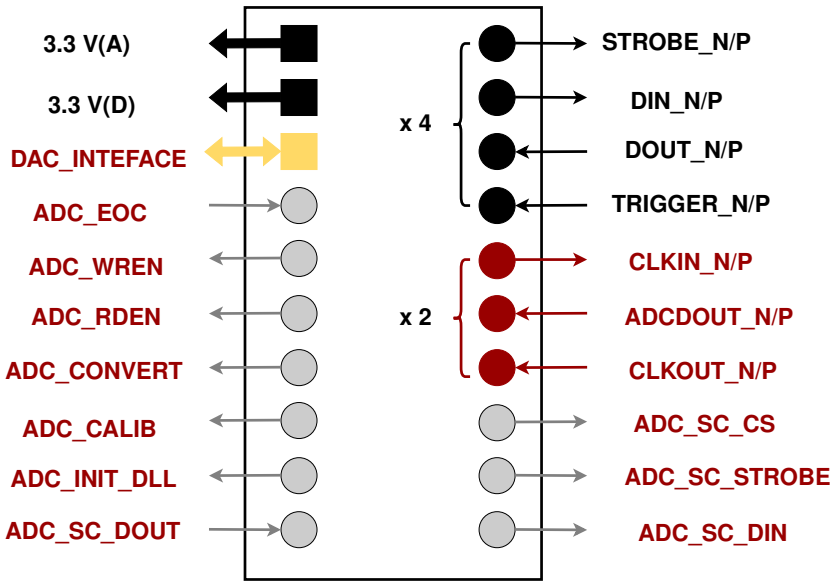

Figure 4.4: The schematic diagram of the MBEE-FEE interface on the MBEE side.

For the OWB-1, an interface similar to the SPI is used for slow control operations. This interface allows the configuration and adjustment of OWB-1 parameters through register access. In addition to the slow control functionality, the interface also includes a series of dedicated signals to manage the workflow of the OWB-1. Due to the limitation of the FEE interface pins, these slow control signals, along with the additional workflow control signals, are shared between two OWB-1 ASICs on a single FEE interface.

- **Slow control of OWB-1**: The slow control in the OWB-1 allows for the configuration of various operational parameters by adjusting its internal values of these registers. For example, it enables the modification to the output clock frequency, the selection of the data transmission mode (either differential serial or single-ended parallel), and the selection of the input mode (whether single-ended or differential input). The key signals involved in this interface include:

  ADC_SC_STROBE: Functions as a clock-like signal, ensuring synchronized data transmission.

ADC_SC_DIN: Acts as the data input line, allowing register configuration data to be sent to the OWB-1.

ADC_SC_DOUT: Acts as the data output line, through which the OWB-1 sends status data back.

ADC_SC_CS (Chip Select): This additional signal selects the OWB-1 for communication, ensuring that commands are directed to the correct device.

- **Control signals of OWB-1**: The control signals are integrated to manage the workflow of the OWB-1. Before the conversion process, a critical step is the calibration of the clock, ensuring accuracy in data handling.

  PLL calibration is performed by applying a 1 MHz clock to the CLKIN input. After calibration, the CLKOUT output provides a clock signal with a selectable frequency of 25 MHz, 50 MHz, or 100 MHz, depending on the system configuration. The calibration is activated through ADC_CALIB signal.

  ADC_CONVERT: This signal initiates the analog-to-digital conversion process.

  ADC_EOC (End of Conversion): Once the conversion is completed, this signal is activated to high, marking the end of the conversion process.

  ADC_WREN (Write Enable): This signal enables the converted data to be written into a specific register for storage or further processing.

  ADC_RDEN (Read Enable): This signal enables the converted data to be read from the specific register, allowing the system to retrieve the digital data generated by the conversion.

- **Sample Signals of OWB-1**: The clock CLKIN is used as the input clock signal for the OWB-1. Once this signal is received, the OWB-1 generates PLL and DLL signals with specific frequencies for sampling purposes. These generated clocks help maintain the timing accuracy needed for reliable data sampling from the FEE. ADCDOUT and CLKOUT are the output signals of the sampling process. CLKOUT serves as the output clock signal synchronized with the sampled data, while ADCDOUT transmits the actual analog-to-digital converted data.

For more details on the operational flow of the IDeF-X HDBD and OWB-1, including the specific function and timing of the control signals involved, please refer to the datasheet from the CEA team and their published papers, such as (Baudin *et al.*, 2018) and (Bouyjou *et al.*, 2017).

- **DAC Interface**: This interface is an SPI protocol, which is responsible for controlling the DAC on the FEE. Through this control, the DAC generates the various voltages needed for the operation of OWB-1.

- **Power Supply for FEE**: FEE is powered by two 3.3 V voltages: 3.3 V(Digital) and 3.3 V(Analog). Both of them are generated on MPSU, and FEE is powered through the power supply part of the FEE interface on the MBEE.

Figure 4.4 shows the schematic diagram of the MBEE-FEE interface on the MBEE side. The FEE interface is implemented by ZA1-Micro-Array-Series from Samtec®.

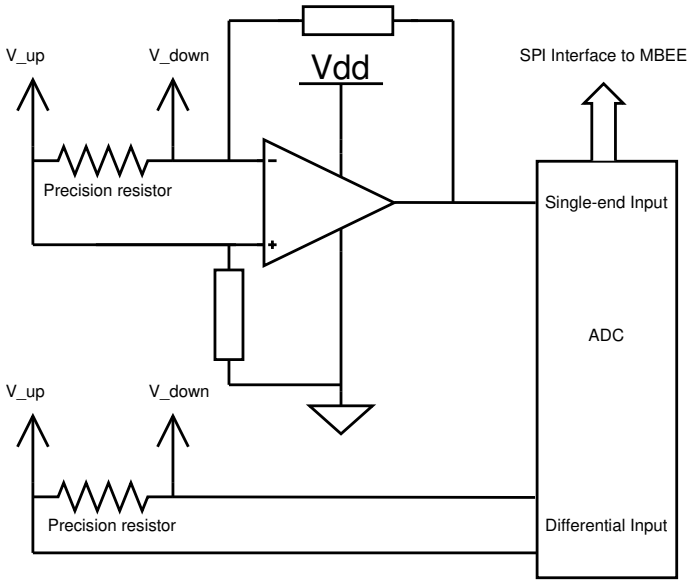

Figure 4.5: The diagrammatic sketch of two different current measurement methods. Upper part: When the voltage drop is too small, an appropriate operational amplifier circuit is applied to adjust the signal before it is sampled by the ADC using a single-ended input. Lower part: When the voltage drop is within an acceptable range, the voltage can be directly input to the ADC using the differential input method.

Housekeeping Circuit

In the current version of the MBEE, the housekeeping circuit is used to monitor the various voltages (HV, MV, and LVs) generated by the MPSU, as well as the currents of the LVs. The monitoring of HV and MV, as introduced in the MPSU section, involves the analog low voltage inputs to the MBEE, proportional to the HV and MV. These analog low voltages, along with the LVs, are sampled by the ADC. The radiation-hardened 8-channel (quad-differential channel) ADC RHFAD128, produced by STMicroelectronics®, was selected for voltage measurement. According to the datasheet, for each input channel, the input voltage range depends on the analog power supply voltage used in the design, which is 3.3 V here. In single-ended mode, this ADC can perform analog-to-digital conversion for eight signals simultaneously, making it suitable for monitoring

all voltages generated by the MPSU. The interface between the ADC and the FPGA is implemented via the SPI protocol.

When an unpredictable error occurs in the circuit, particularly in the case of a short circuit issue, the current often exceeds the preset safety range, which can lead to severe consequences for the system. Therefore, monitoring the currents of the MBEE power supply voltages is necessary. The basic principle for current measurement involves the use of the precision resistor to introduce a voltage drop as the current flows through the resistor. The voltage across the resistor should remain within the dynamic range of the ADC. Figure 4.5 illustrates this measurement method, which consists of three key components: a precision resistor, an operational amplifier circuit, and an ADC. Two compatible methods for measuring the currents of the LVs are implemented in the MBEE, with the appropriate method chosen based on the actual situation: when current flows through a precision resistor, a corresponding voltage drop is generated. Typically, this voltage drop should not be too large, as it may interfere with the normal operation of the MBEE due to insufficient supply voltage. Conversely, if the voltage drop is too small to meet the accuracy requirements of ADC sampling, the operational amplifier circuit can be used to amplify the voltage drop before the ADC samples it. Therefore, evaluation and calculation are required before choosing a proper measurement method.

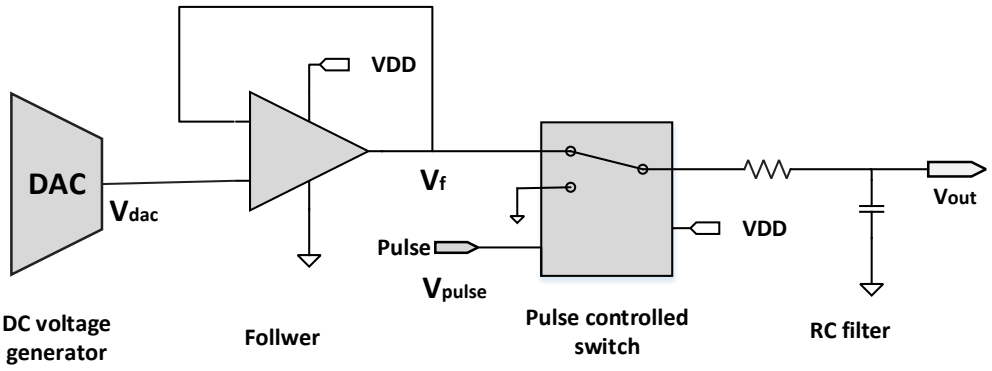

Figure 4.6: The structure of the V-Test circuit, whose prototype was designed by Gianluigi Zampa of INFN (Istituto Nazionale di Fisica Nucleare).

V-Test Circuit

When X-rays interact with the large area multi-channel SDD, a pulse current signal is generated. In an ideal scenario, this signal takes the form of a step function. However, the pulse exhibits a finite rise time, which is influenced by both the response speed and the junction capacitance of the detector. To simulate the current signal produced during an

event, an adjustable square wave generation circuit with a controlled rise time is designed in the MBEE, referred to as the V-Test circuit, as shown in Figure 4.6. The circuit consists of four stages: a DAC, a follower based on an operational amplifier, a pulse-controlled switch, and an RC filter circuit. The DAC and its follower are used to generate step signals with different amplitudes to simulate X-ray photons with different energies, and the RC filter is used to adjust the rise time. The pulse-controlled switch is used to simulate the occurrence of an event. The output of the circuit will serve as the input of IDeF-X HDBD.

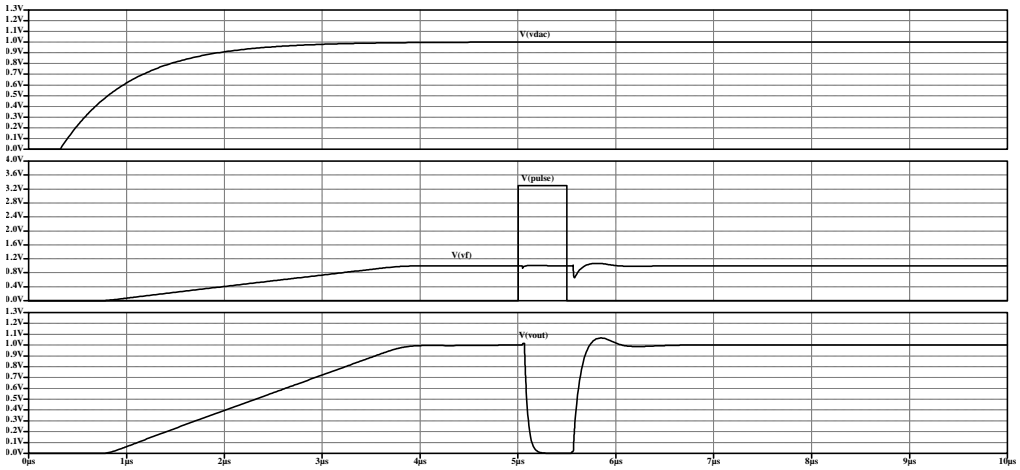

Figure 4.7: It shows the waveform of each critical node of the V-Test circuit to simulate the incidence of an X-ray photon with an energy of 11.25 keV. The top part is the output of DAC-a 1 V DC level; The middle part is the output of the follower and the pulse which is a control switch; The bottom part is the output of the V-Test circuit, which is a pulse with an amplitude of 1 V, its falling edge, representing the charging time of the detector, can be adjusted. According to actual detector experiments in the LAD, the time is about 60-70 ns.

To establish the correlation between the incident X-ray photon's energy and the amplitude of the detector's output step signal, calculations must be conducted based on the characteristics of the large area multi-channel SDD and IDeF-X HDBD used in the LAD, which have been introduced in Chapter 3. The detailed calculation process has been presented in Section 3.3.2 in Chapter 3. Based on the current configuration of IDeF-X HDBD, especially the conversion relationship between the input charge and the output signal of the charge sensitive amplifier, if a signal generator simulates the detector's output, a 10 mV input signal to the charge sensitive amplifier can be equivalent to a 0.5 fC charge injection. In the current MBEE circuit design, the output of the V-Test circuit is first passed through a 1/100 divider before being applied to the input of the charge sensitive amplifier, which does not play a practical role in the V-Test circuit, but only

acts as a voltage divider to generate a suitable input voltage. Therefore, when the DAC stage of the V-Test circuit generates a 1 V voltage, it can be equivalent to 0.5 fC. The incident photon energy E_{photon} corresponding to the charge Q of 0.5 fC can be calculated according to Equation (4.4):

$$E_{\text{photon}} = \frac{Q}{e} \cdot \omega = \frac{0.5 \times 10^{-15}}{1.6 \times 10^{-19}} \times 3.6\,\text{eV} = 11.25\,\text{keV} \tag{4.4}$$

where e is electron charge, and ω is the average ionization energy. For silicon detectors, this value is 3.6 eV. Figure 4.7 demonstrates the output of each stage of the V-Test circuit when subjected to 11.25 keV X-ray photons.

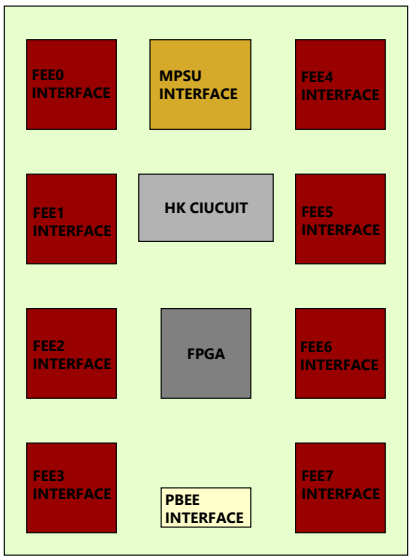

Figure 4.8: Topology of the LAD MBEE.

4.1.3 MBEE Layout and Route

Topology and Layout Design

The layout design of the MBEE is essential for achieving better circuit performance and minimizing electromagnetic interference (EMI). This crucial design phase focuses on systematically organizing the functional blocks of the system to maximize signal integrity while effectively accommodating the spatial constraints imposed by the Printed Circuit Board (PCB) size. The MBEE integrates multiple functional blocks, including digital signal processing blocks, V-Test circuit, housekeeping circuit, and interfaces with other circuits. Among these blocks, V-Test circuit, housekeeping circuit, and the FEE interface are a little bit special, as they handle sensitive analog signals or provide reliable

power supplies for the analog circuits. Proper management, such as shielding and isolation of these analog components, is critical for reducing interference, minimizing noise, and preserving signal integrity across the entire system (Bogatin, 2004).

Figure 4.8 illustrates the topology of the MBEE, showing the strategic partitioning of blocks to limit crosstalk and interference between analog and digital signals, improving the operational stability and efficiency.

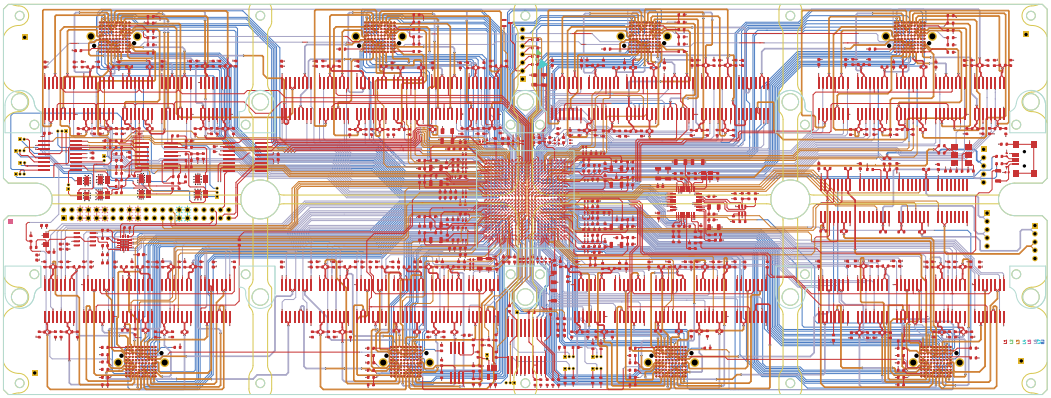

Figure 4.9: The layout and route of the LAD MBEE.

Routing Strategy

MBEE manufacturing fully reflects the strict electrical performance requirements to ensure the stability of power distribution and the integrity of signal transmission. Due to the limitations of the mechanical structure, all components must be laid out on the top layer of the PCB. In addition, the PCB design contains a large number of mounting holes to fix the PCB in the mechanical box of the LAD module. These mounting holes occupy the PCB space, inevitably bringing additional complexity to the layout and routing. The PCB adopts an 8-layer stacking structure with a total thickness of 1.6 mm, including the signal layer, ground layer, and power layer. The layers from top to bottom are Top, Ground, Signal, Power (3.3 VD), Power (1.2 V, 2.5 V, 3.3 VA), Signal, Ground, and Bottom. The power layer and the ground layer are designed in pairs and are continuous and complete to achieve efficient signal isolation and stable power distribution. Signal routing is arranged on the inner layer as much as possible, and the electrical layer adjacent to the signal layer is set as the power or ground layer to provide a complete reference plane. Such a design reduces EMI. In addition, the complete reference plane makes it easy for the signal's continuous impedance control (50 ohms) to reduce the possibility of signal reflection, thereby improving the reliable transmission of signals and system performance. Critical signal paths are carefully considered to make the path length as short

as possible, especially for single-ended signals. A large number of signals are implemented as LVDS, which is known for its excellent noise immunity and signal integrity. Figure 4.9 shows the layout and routing of the MBEE.

Table 4.3 presents the key parameters and constraint rules considered during the design and manufacturing stages of the MBEE.

Table 4.3: Key Parameters during the MBEE Design and Manufacturing Process

Parameter	Description	Value
Trace width	Width of the traces, which is critical for current-carrying capacity and signal integrity	0.10 mm (signal) 0.15 mm (power)
Differential pair configuration	Width, gap of differential pair	0.10 mm (width), 0.10 mm (gap)
Copper thickness	Thickness of the copper layers	35 µm (1 oz)
PCB thickness	Total thickness of PCB	1.6 mm
Impedance control	Precise impedance settings for high-speed signal lines to minimize signal reflection and improve integrity.	50 ohms
Number of layers	Total number of PCB layers, balancing signal isolation and board complexity.	8 layers
Layer assignment	Electrical layer stacking structure	Top-Ground-Signal-Power(3.3 VD)-Power(Other)-Signal-Ground-Bottom
Power and Ground plane design	Design of power and ground planes for stable power distribution and noise reduction.	Paired, complete and continuous
Via size and type	Diameter and type (through-hole, blind, or buried) of vias	Through-hole Normal: 0.4 mm (diameter), 0.2 mm (hole) Power: 0.5 mm (diameter), 0.3 mm (hole)

Continued on next page

Table 4.3 – *Continued from previous page*

Parameter	Description	Value
Dielectric constant of materials	Dielectric properties of insulating materials between layers, affecting signal propagation speed.	4.2 (FR4)
Trace spacing	Minimum spacing between traces	0.125 mm

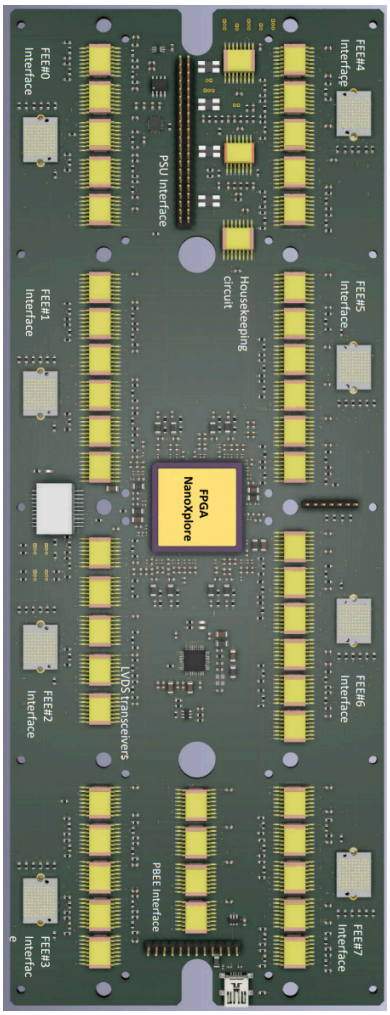

Figure 4.10: The 3D model of the LAD MBEE.

Figure 4.10 shows the 3D model of the MBEE PCB after layout and routing.

4.2 MBEE VHDL Design

4.2.1 Overview

The MBEE performs multiple functions and serves as the central processing unit of the detector module. Figure 4.11 illustrates the architecture of the FPGA program, broadly divided into two major parts: the configuration and control of the detection module's electronics, and the generation and acquisition of science data. The configuration and control of the detection module's electronics mainly includes the MBEE configuration, MPSU configuration, acquisition of housekeeping data, ASICs on FEE configuration, and so on. These operations are typically managed through remote control telecommands issued by the ICU through the PBEE. Once a telecommand from the PBEE is received, the MBEE decodes it and executes the corresponding operation. If the command requires return data, the data is generated on the MBEE and then transmitted back to the PBEE. In cases where no return data is needed, the MBEE sends a response to the PBEE, indicating the successful execution of the operation. These data, generated only after receiving a remote control telecommand, are stored in a dedicated FIFO buffer named "output FIFO for response and HK data" before transmission to the PBEE, which is shown in Figure 4.11. Conversely, science data is generated independently from the telecommand. Instead, they are produced when a valid X-ray event is detected and processed. A separate FIFO named "output FIFO for science data" is exclusively dedicated to science data, as shown in Figure 4.11, isolated from other types of data. The following sections will introduce the implementation of the FPGA program.

4.2.2 Clock System

The clock system is distributed via the PBEE interface, providing two LVDS clocks with different frequencies: a 1 Hz Pulse Per Second (PPS) signal and a 10 MHz clock. The PPS is synchronized with GNSS time for a precise absolute time recording, while the 10 MHz clock operates in conjunction with the PLL of the FPGA to generate the system clock and improve the accuracy of time recording.

Here we introduce the specific process of time recording. Two counters are applied: one to track seconds and the other to measure microseconds. The second counter increments with each new PPS signal, and the microsecond counter increments every ten periods of the 10 MHz clock (1 μs), and resets upon each new PPS signal. For a system base frequency of 10 MHz, a 20-bit counter is required to record the microsecond value (the maximum value of the microsecond counter is 999,999). Figure 4.12 illustrates the two clocks and how they generate the second counter and microsecond counter.

The accuracy of the two clocks determines the accuracy of the timestamp. Since the PPS is synchronized with GNSS time and exhibits high stability, the overall timing accuracy is primarily influenced by the 10 MHz clock. Upon each microsecond counter reset, the MBEE calculates the deviation between the current microsecond counter value

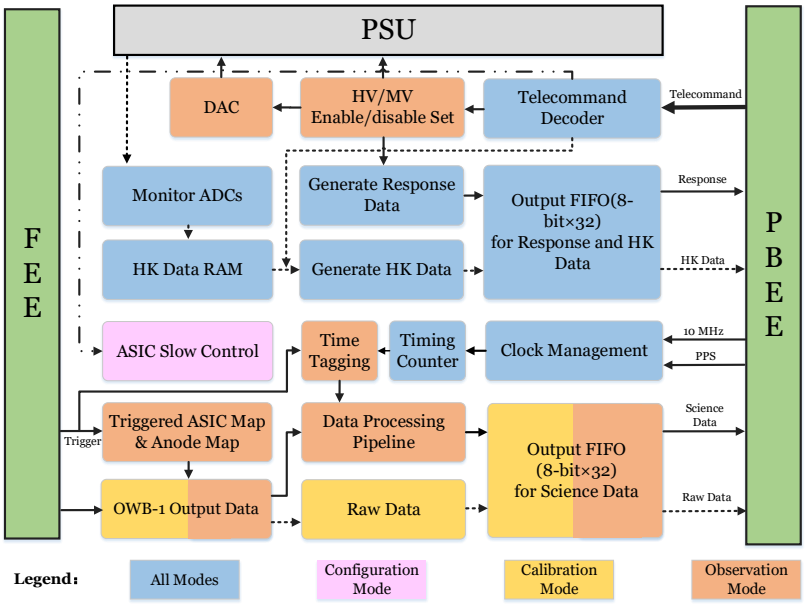

Figure 4.11: FPGA program architecture of the LAD MBEE (Xiong *et al.*, 2025).

and the expected number of cycles in one second (1,000,000). This deviation, stored in the housekeeping data packet, reflects the system's time error and is used for the timing calibration discussed in Section 4.3 in this chapter.

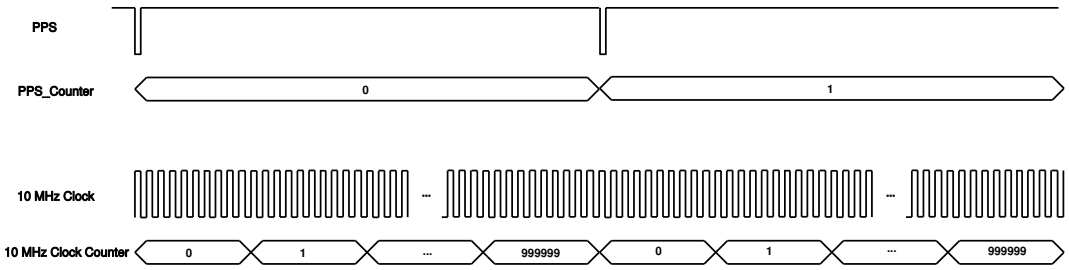

Figure 4.12: The clock system and its working principle for recording time information. The PPS counter provides the absolute time, while the 10 MHz counter increases time accuracy.

4.2.3 Communication Protocol Definition

Since the LAD's back-end electronics hardware design follows a layered architecture, the communication protocol also follows the layered design. This protocol includes two

types: communication between the ICU and PBEE via SpaceWire, and communication between the PBEE and MBEE via UART. In this section, we focus on the communication protocol between the PBEE and MBEE over UART, covering the transmission of the telecommand and the response. The baud rate is adjustable, allowing for flexibility in data transmission. A detailed analysis of the relationship between baud rate, X-ray flux, and system dead time will be presented in Section 4.3 of this chapter.

Telecommand Packet Structure

Figure 4.13 illustrates the structure of the telecommand packet, which is divided into several fields, each with a specific purpose and defined length.

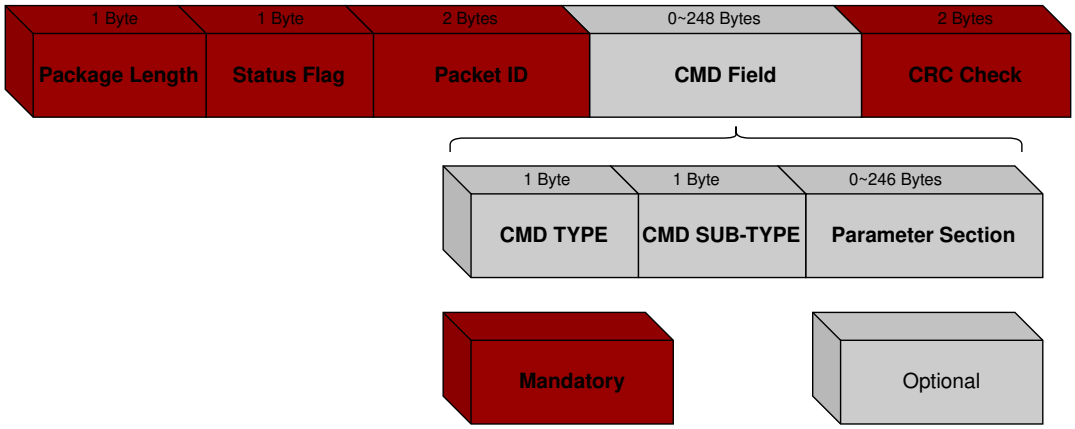

Figure 4.13: The structure of the telecommand.

The **Packet Length** field (1 byte) indicates the total length of the packet, while the **Status Flag** (1 byte) identifies the packet's status. The **Packet ID** consists of two bytes, as a unique identifier for the packet. The **CMD Field**, which is variable in length (0 to 246 bytes), contains the command-specific information and is the only optional field in the packet. Within the CMD Field, the CMD TYPE defines the type of telecommand, and the CMD SUB-TYPE refines the telecommand into subtypes. The Parameter Section describes the specific details and requirements of the telecommand. The mapping between type/subtype and telecommand operation will be introduced when the MBEE implements specific functions. Finally, the **CRC Check** field, 2 bytes in length, performs a cyclic redundancy check to ensure the integrity of the packet during transmission. Except for the CMD Field, all other fields are mandatory and must be included in each telecommand.

- Packet Length: The variable length of the telecommand significantly enhances data transmission flexibility, allowing efficient and accurate transmission of different types of telecommands without unnecessary resource consumption.

- Status Flag: This byte describes the type of telecommand, as shown in Table 4.4.

Table 4.4: Bit Description of Status Flag Byte

Bit	Name	Explanation
0	ICU CMD flag	Indicates packet is a telecommand from PC to ICU.
1	ALERT bit	Indicates an event originating from MBEE, PBEE, or ICU might be a scheduled event or unexpected.
2	"Get" answer bit	Indicates the package is an answer to a "get" CMD, which usually refers to obtaining the parameters of the module electronics.
3	MBEE HK bit	Indicates the package contains MBEE housekeeping data.
4	PBEE HK bit	Indicates the package contains PBEE housekeeping data.
5	ACK bit	Indicates the telecommand executed by the electronics successfully.
6	ERROR bit	Indicates that the telecommand is not applicable or there is no such telecommand.
7	Data type bit	Indicates what type of package: telecommand or science data transmission. (0b: telecommand / 1b: Science data)

- Packet ID: A unique identifier for the packet, for the response packet, these two bytes are the same as those of the telecommand being responded to.

- CRC Check: This information serves to check the correct transmission of the telecommand, its response, and other types of data.

Responses Frame Definition

There are four types of responses sent through the PBEE-MBEE interface to the PBEE:

(1) The first response is used to confirm that a given telecommand was successfully executed;

(2) The second response is a negative acknowledgment, sent when a transmission error occurs or to indicate an error;

(3) The third response is the answer to the "get" function, in which the requested parameters or housekeeping data are returned.

(4) The fourth type involves the transmission of science data.

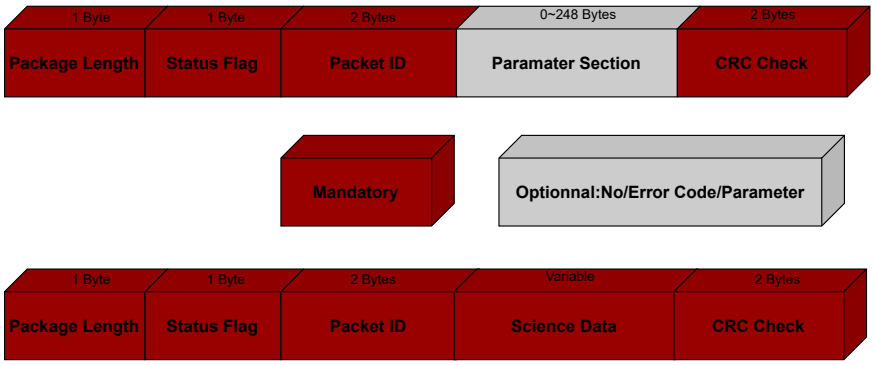

Figure 4.14: The response packet frame.

The upper part of Figure 4.14 represents the structure of the first three types of responses, which includes the data **Packet Length**, **Status Flag**, **Packet ID**, **Parameter Section**, and two bytes for **CRC Check**. The Parameter Section varies depending on the type of response: for the first type of response, there is no Parameter Section; if the response indicates an error, the parameter contains an error code (see Table 4.5); and the data involve the parameter or housekeeping data are included in this part in the third type of the response. The lower part of Figure 4.14 shows the structure of the science data, which consists of the **Packet Length**, **Status Flag**, **Packet ID**, **Science Data**, and **CRC Check** fields.

Table 4.5: Error Codes

Error type	**Code**
Reserved	0x00
General error	0x01
Invalid packet CRC	0x03
Error packet length	0x04
Empty telecommand	0x05
Invalid telecommand TYPE	0x06
Invalid telecommand SUB-TYPE	0x07
Invalid telecommand	0x08
Illegal telecommand (*)	0x09

* It means this telecommand is correct, but it cannot give the expected response in the current scenario.

4.2.4 MBEE Operation Modes

MBEE has different operation modes to adapt to its diverse functional requirements. Figure 4.15 presents the modes and their switching of the MBEE operation modes. In each mode, the MBEE is responsible for carrying out specific tasks in the following modes:

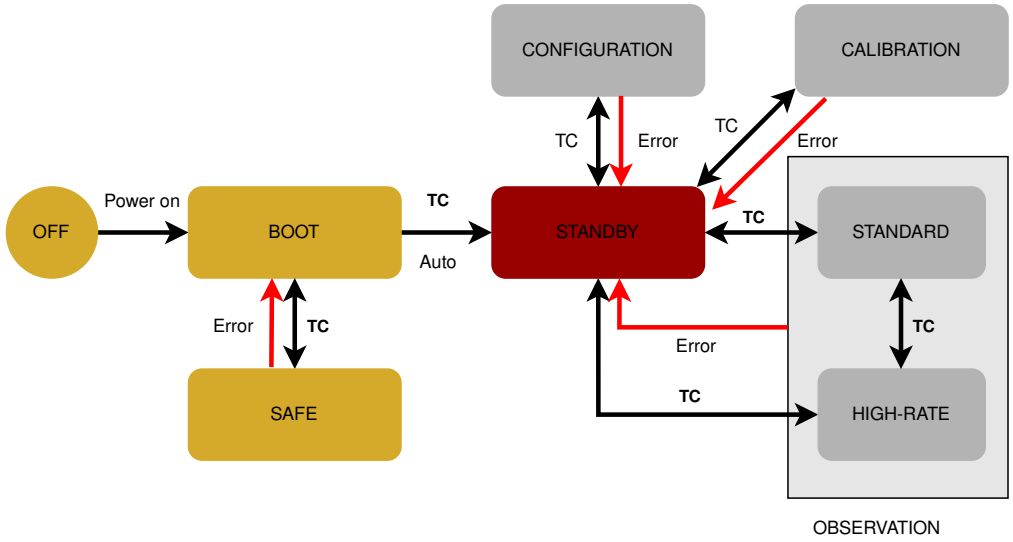

Figure 4.15: Modes and their switching in the MBEE. Boot mode is a transitory operation mode after a correct power-on sequence, before entering standby mode. When the MBEE is in modes such as calibration, configuration, or observation, if an error occurs, like an excessive current caused by a circuit malfunction, the MBEE will automatically enter safe mode, shutting down most functions to protect the system circuitry as much as possible.

- Standby mode: Following a correct power-on sequence, if there is no error in the instrument, the MBEE enters standby mode through a transitory operation mode — boot mode. In standby mode, in terms of transmissible data, only the acquisition of housekeeping data can be operated, and switching to other modes will be based on this primary mode.
- Safe mode: Safe mode holds the highest priority. When the MBEE experiences some errors, such as the voltage or current exceeding the safety range, the MBEE will enter this mode directly from any other operation mode. In this mode, the MBEE's functionalities are limited, permitting only fundamental operations via telecommand control, such as obtaining housekeeping data. Exiting from safe mode to standby mode necessitates explicit telecommand intervention.

- Configuration mode: Configuration mode is isolated from other modes to ensure coherent functionality and data uniformity during operation. This mode allows us to modify the registers of IDeF-X HDBD and OWB-1 and the parameters stored in the RAM of the MBEE by telecommand to accommodate different engineering operation requirements, such as the parameters related to energy reconstruction (e.g. pedestal, threshold, gain value for each readout channel) and the mask register to activate/deactivate read channels.

- Calibration mode: Calibration mode offers transparency by facilitating extensive access to information concerning detector anodes and electronic readout channels. The most important thing is to acquire the actual pedestal value, gain value for each channel, and update them in the dedicated memory device. Specifically, this is achieved by injecting a programmable amount of charge (including the injected charge amount of 0) into each channel using the V-Test circuit, and the gain can be calculated by the input of the V-Test circuit and the corresponding amplitude value of the output signal. And the pedestal is the amplitude value of the output signal with an injected charge amount of 0.

- Observation mode: This mode serves as the primary mode for event detection, offering two different observation modes according to the event rate: standard mode and high-rate mode. Once the X-ray photons hit the large area multi-channel SDD, an automatic procedure is performed to process the data based on the concept of the data processing pipeline to reconstruct the X-ray event. Then, a packet containing event energy, time tagging, the trigger anode number, and other information will be compiled and stored in the MBEE, where it waits to be transmitted to the PBEE.

Table 4.6: CMD Field of Setting and Switching of the MBEE Operation Modes

CMD Field			**Description**
TYPE	**SUB-TYPE**	**Parameter Section**	
0x19	0x01	-	Stand-by mode
0x19	0x02	-	Safe mode
0x19	0x03	-	Configuration mode
0x19	0x04	-	Calibration mode
0x19	0x05	-	Observation Standard mode
0x19	0x06	-	Observation High-rate mode
0x19	0x07	-	Get current mode

Table 4.6 shows the CMD Field definition of setting and switching the MBEE operation modes. The length of this telecommand is 8 bytes without the Parameter Section. If the mode is set or switched successfully, the MBEE will return an “executed” response;

otherwise, it will provide an "error" response containing the error code. The telecommand corresponding to SUB-TYPE 0x07 is used to obtain the current operation mode of the MBEE.

4.2.5 Connection Test

This operation is conducted to test the connection state of the MBEE-PBEE interface, and the telecommand can be sent in any MBEE operation mode. If the connection works correctly, an "executed" response will be returned. Otherwise, a response containing specific error information will be given.

Table 4.7: CMD Field of Performing Connection Test

CMD Field			Description
TYPE	**SUB-TYPE**	**Parameter Section**	
0x11	0x01	-	Perform Connection Test

4.2.6 High Voltage and Medium Voltage Operation

Both HV and MV are used for the detector's work; consequently, for the MBEE, HV and MV operations are restricted to the observation mode. In all other operation modes, both these two kinds of voltages remain disabled, and any attempt to execute related telecommands will result in an error response.

The control of the MV involves enabling and disabling MV, while the control of HV encompasses both enabling and disabling HV, as well as adjusting its value. To implement the ramp-up and ramp-down process to increase and decrease the voltage gradually, a counter is implemented in the program. The rate at which the counter increments by one is used to regulate the rate of change in the DAC's value, thereby enabling a controlled voltage adjustment process.

It is important to note that, to ensure maximum protection of the module electronics, the HV can only be activated when the MV is already enabled. If the MV is not enabled, any attempt to operate the HV will be regarded as an invalid operation. This dependency safeguards the system by preventing improper voltage configurations.

Table 4.8 shows the CMD Field part of the telecommands involving the HV and MV operations. Equation (4.5) shows the setting method of the HV. *Data* in Equation (4.5) is a 2-byte hexadecimal value, and V is the HV value set with the unit of volt.

$$Data = \frac{V \times 2^{12}}{2440} \tag{4.5}$$

For example, if we want to set the HV0 to 1300 V, then the data can be calculated by Equation (4.6):

$$Data = \frac{1300 \times 2^{12}}{2440} = 2182(\mathrm{d}) = 0\mathrm{x}0886 \tag{4.6}$$

Table 4.8: CMD Field of High Voltage and Medium Voltage Operation

CMD Field				Description
TYPE	**SUB-TYPE**	**Operation Type**	**Data(2 byte)**	
0x14	0x04	0x11	-	HV0 Enable
0x14	0x04	0x10	-	HV0 Disable
0x14	0x04	0x13	Equation (4.5)	HV0 Set
0x14	0x04	0x21	-	HV1 Enable
0x14	0x04	0x20	-	HV1 Disable
0x14	0x04	0x23	Equation (4.5)	HV1 Set
0x14	0x04	0x30	-	MV Enable
0x14	0x04	0x31	-	MV Disable

4.2.7 Housekeeping Data

CMD Field Definition of Housekeeping Data

The housekeeping data is derived from the ADC within the MBEE's housekeeping circuit. After powering on, the ADC continuously samples the voltages associated with various operational parameters of the module's electronics. Once "Housekeeping Report Generation" is enabled, the RAM allocated for storing housekeeping data is periodically updated at a predetermined time interval. When the MBEE receives a "Get Housekeeping" command, it generates a housekeeping data packet. This packet includes the current operation mode of the MBEE, interval time, time error, HV values, MV value, LV values, the corresponding current value associated with each LV, and temperature values (in the next version). This set of housekeeping data is then transmitted to the PBEE.

Answer Frame of Housekeeping Data

Figure 4.16 shows the format of the Parameter Section for the housekeeping data packet. Each parameter occupies 2 bytes and provides information on the current operation mode, time error, housekeeping data interval time, four LVs and their currents, two HVs, and one MV. In the next version of the MBEE, the temperature sensor will be integrated, and FEE temperature data will be transmitted to the MBEE, allowing temperature readings of the module's electronics to be included in the housekeeping data packet. These temperature measurements will be used for calibration during the X-ray energy reconstruction process. Additionally, in the situation of a short circuit in the electronics, a

Table 4.9: CMD Field of Housekeeping Data

CMD Field			Description
TYPE	**SUB-TYPE**	**Parameter Section**	
0x03	0x05	-	Enable Housekeeping Parameter Report Generation
0x03	0x06	-	Disable Housekeeping Parameter Report Generation
0x03	0x1F	-	Define Housekeeping Parameter Report Collection Interval
0x03	0x21	-	Get Housekeeping Interval Time
0x03	0x80	-	Get a Housekeeping Data Packet

rapid increase in local temperature can be detected, making the temperature sensor an indirect method for monitoring the status of the electronics.

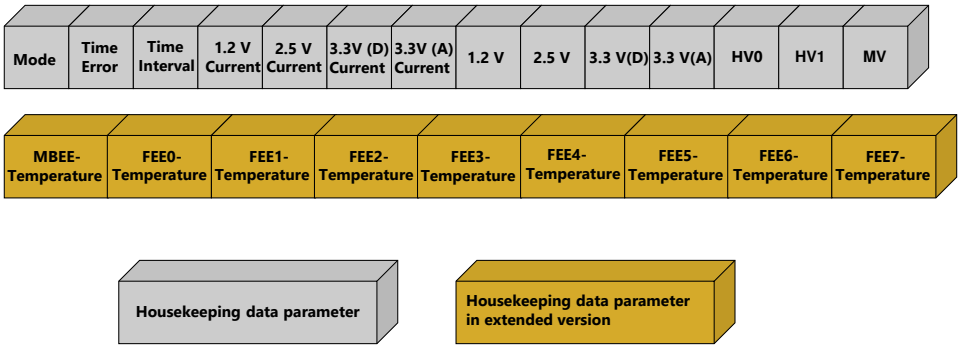

Figure 4.16: Housekeeping data frame. Each parameter takes up 2 bytes. The parameters in the gold boxes are the temperatures of the MBEE and the FEEs interfacing with the same MBEE, which will be introduced in the next version of the MBEE.

4.2.8 ASICs and DAC on FEE Configuration

After the system is powered on, configuring all the necessary parameters is essential for ensuring proper operation. These configurations involve setting the parameters of the hardware components, such as ASICs and DACs. To configure the ASICs and DACs in the FEE, the MBEE must first enter the configuration mode. This section will discuss the distinct configuration processes for the IDeF-X HDBD, OWB-1, and DAC.

IDeF-X HDBD Configuration

Table 4.10 defines the CMD Field of the telecommand about how to configure IDeF-X HDBD and get the current parameters of the IDeF-X HDBD. The Parameter Section consists of 9 bytes. In the byte Type and Address, configuration type and address information are encoded: Bits 7 to 5 of the byte Type and Address (001) indicate that the command is designated for IDeF-X HDBD configuration; Bits 4 to 2 represent the FEE ID (000 to 111), which specifies one of the eight FEEs in a single MBEE, and Bits 1 to 0 indicate the Group ID (00 to 11), identifying one of the four groups of IDeF-X HDBD within a given FEE.

Table 4.10: CMD Field of IDeF-X HDBD Configuration

CMD Field										
TYPE	**SUB-TYPE**	**Parameter Section**								
		Type and Address								**8-Byte CMD**
0x14	0x03	**IDeF-X**			**FEE ID**			**Group ID**		
		0	0	1	*	*	*	*	*	

The 8-byte CMD plays a critical role in determining the specific operation that a telecommand will carry out for the IDeF-X HDBD. It defines whether the telecommand is intended to configure or obtain parameters. For the configuration, the telecommand will write values to a register, changing the operational parameters of the IDeF-X HDBD, while for the latter, the telecommand is used to read the contents of a register to retrieve current operational values in order to get the status information. Additionally, the 8-byte CMD contains an IDeF-X HDBD address to distinguish the seven IDeF-X HDBDs that share the same slow control signals; the register's address to specify the particular register that the command will interact with; and the register value needs to be written to the specified register. For details about the 8-byte CMD Field of IDeF-X HDBD, please refer to IDeF-X Readout Core User Guide prepared by Samuel Pliego Caballero of IAAT.

OWB-1 Configuration

Table 4.11 defines the CMD Field of the telecommand about how to configure OWB-1 and get the current parameters of the OWB-1. The principle is the same as that of IDeF-X HDBD. In the byte Type and Address, Bits 7 to 5 (010) indicate that the command is designated for OWB-1 configuration; Bits 4 to 2 represent the FEE ID (000 to 111), which specifies one of the eight FEEs in a single MBEE; and Bits 1 to 0 make no sense because only two OWB-1 ASICs in the same group in each FEE.

For details about the 8-byte CMD Field of the OWB-1, please refer to OWB-1 Readout Core User Guide prepared by Samuel Pliego Caballero of IAAT.

Table 4.11: CMD Field of OWB-1 Configuration

CMD Field									
TYPE	SUB-TYPE	Parameter Section							
		Type and Address							8-Byte CMD
0x14	0x03	OWB-1			FEE			N/A	
		0	1	0	*	*	*	-	-

DAC for OWB-1 Configuration

The OWB-1 requires specific voltages for its normal operation. The DAC on the FEE supplies these voltages; therefore, the DAC must be configured to generate the appropriate voltages that power and bias the various analog and digital components within the OWB-1. Table 4.12 shows the CMD Field of the telecommand for DAC configuration. The relationship between the output voltage and the 12-bit code in the telecommand can be calculated by Equation (4.7).

Table 4.12: CMD Field of DAC for OWB-1 Configuration

CMD Field					Description
TYPE	SUB-TYPE	Operation Type	Data (2 byte)		
0x14	0x05	0x01	12-bit code	N/A	Channel 1
0x14	0x05	0x02	12-bit code	N/A	Channel 2
0x14	0x05	0x04	12-bit code	N/A	Channel 3
0x14	0x05	0x08	12-bit code	N/A	Channel 4

$$V_{out} = \frac{12\ bit\ code}{4096} \times V_{Ref}, \quad V_{Ref} = +2.44V \tag{4.7}$$

4.2.9 Science Data Packet

To handle the generation and transmission of science data, the MBEE must be operated in observation mode. While in observation mode, MBEE reads the digital signals from the FEEs, reconstructs the energy of each X-ray event, and timestamps the events before packaging the information for transmission to PBEE.

Science Data Packet Definition

The recording of X-ray event arrival time and the reconstruction of their energy are central to the MBEE's core functions. These X-ray event data are packaged into a science data packet, which is first transmitted to the PBEE and subsequently relayed to the ICU. The MBEE operates in two distinct observation modes, each optimized for observing different ranges of X-ray flux. Each observation mode generates a unique science data packet format that reflects the mode's data handling and processing needs. Figure 4.17 illustrates the structural differences between the science data packets in these two observation modes.

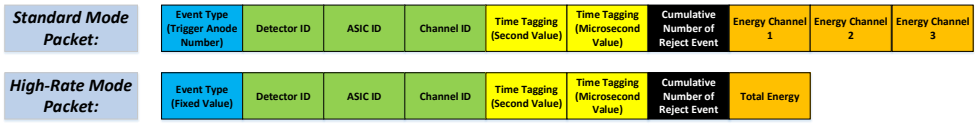

Figure 4.17: The structure of two different science data packets in different observation modes (Xiong *et al.*, 2025).

- **Event type**: In the standard observation mode, the event type indicates the number of anodes that are effectively triggered for an X-ray event. As previously mentioned, an X-ray event is considered valid when no more than three adjacent anodes are triggered simultaneously. Based on this criterion, three distinct event types are defined: 3'b001, 3'b010, and 3'b011, corresponding to different numbers of adjacent anodes triggered. In contrast, under the high-rate observation mode, the system no longer differentiates between event types. All events, regardless of the specific triggering pattern, are categorized uniformly as 3'b100.

- **Event ID**: As detailed in Chapter 3, each MBEE is connected to eight detectors, and each detector is equipped with 224 anodes. To precisely identify which anode has been triggered during an event, various identification (ID) codes must be recorded. The **detector ID** is represented by a 3-bit binary code, ranging from 3'b000 to 3'b111, with each ID corresponding to a different detector.

  In each detector, four groups of 28 IDeF-X HDBD ASICs are responsible for reading signals from the 224 anodes. To accurately identify which IDeF-X HDBD processed the signal from a triggered anode, a 5-bit binary code from 5'b00000 to 5'b11011 is used to generate an **ASIC ID** specific to the IDeF-X HDBD.

  Furthermore, each IDeF-X HDBD manages signals from 8 anodes. Thus, the **channel ID** with 3-bit binary code from 3'b000 to 3'b111 is used to specify which channel(s) within an IDeF-X HDBD was/were triggered. Since multiple adjacent

channels may be triggered simultaneously, it is stipulated that the channel with the smallest ID will be recorded as the Channel ID in the event packet. This identifies the location of the triggered anode.

- **Time tagging**: A 2-byte data field and a 2.5-byte data field are allocated to record the time information (second value and microsecond value) of an X-ray event. As explained in Section 4.2.2, the time is continuously tracked by two counters that are updated with the system clock—one counting in seconds and the other in microseconds. When an event trigger signal is detected, the current values of these two counters are captured immediately. These captured values represent the time of the event, with one providing the timestamp in the unit of seconds and the other offering microsecond resolution.

- **Number of reject events**: Not all trigger signals correspond to valid X-ray events. For instance, false triggers caused by noise or events that do not meet the predefined event criteria are considered invalid and subsequently rejected. To track these occurrences, a single-byte field is dedicated to counting the number of rejected events since the system was powered on. This counter provides a cumulative total of invalid triggers and can be reset to zero and recalculated as needed, allowing for continuous monitoring of the probability of false event detections.

- **Energy value**: This part is dedicated to recording the energy value of X-ray events. The detailed process of energy reconstruction will be discussed in Section 4.2.10. Here, we focus on the data structure used for storing the energy values. A key distinction between the science data packets in the two different observation modes lies in how the energy data is presented. In the standard observation mode, the energy values for each individual channel are provided in detail. This allows for not only a calculation of the total energy but also a clear understanding of the energy distribution across the channels. These separate data help us characterize the event accurately. In the high-rate observation mode, only the total energy of the event is recorded, without detailed energy distribution information for each channel. This simplified approach is necessary to handle the higher data throughput in this mode. Each energy value is stored in a 9-bit field, which represents energy levels in the range from 2 keV to 30 keV. The scaling that 60 eV per digit is used in this energy range, which means that 1 bit represents the energy of 60 eV. It is worth noting that when transmitting raw science data, this part is also compatible with 13 bits of raw energy data for each channel in standard observation mode.

CMD Field of Get Science Data Packet

Once the science data packet is generated, it is stored in the FIFO memory dedicated to science data. To retrieve the science data from the FIFO, a specific telecommand, as shown in Table 4.13, must be issued.

Table 4.13: CMD Field of Get Science Data Packet

CMD Field			Description
TYPE	**SUB-TYPE**	**Parameter Section**	
0x18	0x04	-	Get Science Data Packet

Generate Dummy Science Data Packet

A series of specialized telecommands is used to generate corresponding science data packets, designed for testing purposes. Although these packets do not contain actual science data, their structure mirrors that of real science data packets. This design is particularly useful for verifying and evaluating the data transmission capabilities of the MBEE-PBEE interface. By simulating the transmission of science data, this approach enables thorough testing of communication protocols, ensuring reliable data handling and system performance before actual data collection begins. Table 4.14 shows the CMD Field of Generate Dummy Science Data Packet.

Table 4.14: CMD Field of Generate Dummy Science Data Packet

CMD Field			Description
TYPE	**SUB-TYPE**	**Parameter Section**	
0x1E	0x01	-	One-Channel Event
0x1E	0x02	-	Two-Channel Event
0x1E	0x03	-	Three-Channel Event
0x1E	0x04	-	A Rejected Event

4.2.10 Data Processing Pipeline

In observation mode, the FPGA firmware in the MBEE uses a pipeline concept for data processing, as shown in Figure 4.18. This pipeline concept allows for real-time processing for X-ray events, therefore, the "long" processing phase in the MBEE hardly introduces the dead time to the overall system, minimizing the impact of the event processing time on the system's ability to detect and handle subsequent events, significantly enhancing the system's capability to detect high-flux sources.

When a signal from a readout channel exceeds the pre-set low threshold, a trigger signal is immediately generated and sent to the MBEE. A timestamp is recorded to get the values in the second counter and the microsecond value in Section 4.2.2 to obtain the exact time of the X-ray event. At the same time, a 'frozen' signal halts all readout channels in this detector half. Crucially, the data processing pipeline of the two detector halves operates independently. The 'frozen' signal only affects the specific detector half

where the event occurred, allowing the other half to continue processing signals without interruption.

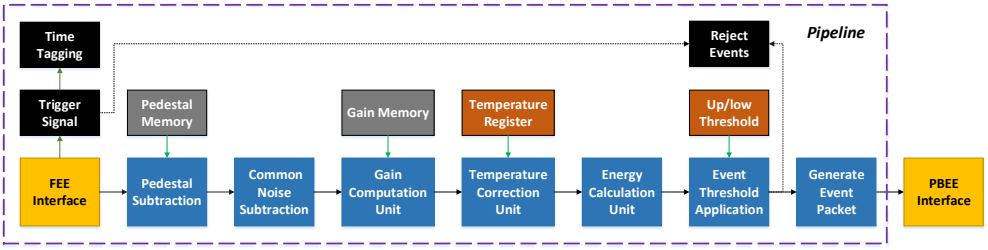

Figure 4.18: The structure of the data processing pipeline (Xiong *et al.*, 2025).

Immediately following the trigger signal, the IDeF-X HDBD generates both the triggered ASIC map and the triggered anode map, which provide detailed identification of the specific ASICs and anodes activated in this X-ray event. The MBEE then applies a filtering process to determine valid events, adhering to the identification criteria described in Chapter 3 to ensure that only meaningful events are processed. According to the triggered ASIC map and triggered anode map, the event type and event ID can be immediately acquired: the detector ID can be acquired because each detector and its FEE use a FEE interface; the ASIC ID and the channel ID can be obtained based on the triggered ASIC map and triggered anode map.

Subsequently, the MBEE signals the OWB-1 to initiate the analog-to-digital (A/D) conversion process. During this phase, OWB-1 converts the peak values of the analog signals from the 112 anode channels into digital values. Let's review the 112 anodes in one detector half and the FEE that reads these signals. Every eight anodes share one IDeF-X HDBD, and each IDeF-X HDBD only has a single analog signal output. This output is connected to a differential input of the OWB-1. Furthermore, two groups of 14 IDeF-X HDBD are connected to a single OWB-1. During each conversion cycle, the OWB-1 concurrently digitizes the analog signals from 14 IDeF-X HDBD ASICs, with this process repeated eight times to complete the analog-to-digital conversion for all 112 anode channels. Given that the maximum time for a single analog-to-digital conversion is 2.56 µs, however, there is only one analog output port on one IDeF-X HDBD, therefore, the analog-to-digital conversion of the signals on 8 anode readout channels on each IDeF-X HDBD should be conducted in sequence, making the total conversion time equal to 8 times the single conversion time $T_{\text{single conversion}}$, then the total conversion time is approximately 20.48 µs. The total dead time of the detector assembly consists of two primary components: total conversion time and data transmission time, as described by Equation (4.8):

$$Dead\ Time_{\text{DA}} \approx 8 \times T_{\text{single conversion}} + T_{\text{transmission}} \tag{4.8}$$

The transmission time is calculated based on the amount of data transmitted and the transmission rate (25 Mbps), which is about 115.20 µs. Therefore, the total dead time of the detector assembly can be calculated by the sum of the total conversion time, 20.48 µs, and the transmission time, 115.20 µs, which equals 135.68 µs.

In the future version of OWB-1, the implementation of analog-to-digital conversion will be restricted exclusively to the IDeF-X HDBD associated with the triggered anode channels, which will markedly reduce the volume of data transmitted, thereby significantly minimizing the system's dead time. Section 4.3 will provide a detailed analysis of the components contributing to system dead time and explore its relationship with data transmission speed and X-ray flux.

Once the A/D conversion is completed, and all the channel data have been successfully transmitted to the MBEE, the MBEE sends a signal to both the detector and the FEE, indicating that the 'frozen' state can now be exited. This allows the system to resume normal operations and receive new X-ray events. Then, the MBEE processes the acquired data to construct the science data packet introduced in Section 4.2.9 for each valid X-ray event. The general idea of the pipeline concept is to be able to receive new events while the processing of the old events is not yet completed, which will reduce the dead time. This section will present the working principle and the structure of the data processing pipeline.

Since a valid event involves a maximum of three adjacent anode channels, only one or two IDeF-X HDBDs are engaged in the energy reconstruction process. These are referred to as active IDeF-X HDBDs, whose channels will be used in the data processing. When two IDeF-X HDBDs are active, both are fully used in the reconstruction; however, when only one IDeF-X HDBD is active, this IDeF-X HDBD, along with the closest IDEF-X HDBD to the triggered channel, is engaged to ensure accurate signal processing. Therefore, only the data from two IDeF-X HDBDs are dealt with in the data processing pipeline during energy reconstruction.

Before entering the pipeline, data from each channel in the active IDeF-X HDBDs undergoes a conversion from Gray code to a 13-bit binary format. All subsequent processing in the data pipeline is performed on this 13-bit binary data.

- **Pedestal subtraction** is the first step in the data processing pipeline, designed to address manufacturing inconsistencies that result in unique pedestal values for each anode within the detector. As the initial stage of data processing, the MBEE retrieves a predefined set of pedestal values, each uniquely associated with a specific anode channel. These pedestal values, stored within the MBEE's memory, are subtracted from the incoming measured signals for each anode channel. By accurately calibrating the baseline, pedestal subtraction ensures that each anode's output is centered around a uniform zero-point, thus improving the accuracy of energy measurements and the consistency of signal processing across all channels.
- **Common mode noise subtraction** is a step that mitigates baseline shifts resulting from inherent noise, electronic fluctuations, and environmental variations, which

can collectively impact measurement accuracy across all channels. This noise arises from factors such as electronic noise and statistical fluctuations in the system, if not corrected, can skew the data and lead to inaccuracies in detecting and measuring signals from X-ray events. To isolate and correct this common mode noise, the MBEE calculates an average noise value by sampling channels that are not directly involved in the electron cloud absorption for each IDeF-X HDBD. The average baseline noise from these non-active channels is then subtracted from the measured signals in the active channels, thereby normalizing the data and improving the signal-to-noise ratio.

- **Energy reconstruction**: Gain and temperature correction are required during energy reconstruction. The total energy of an event is determined by summing the contributions from the triggered channels, with each contribution multiplied by an individual gain factor stored within the MBEE. Additionally, energy values must be corrected to account for environmental temperature variations. However, in the prototype development phase of the MBEE, temperature calibration has not yet been implemented.

- **Event threshold application**: The reconstructed energy is compared with upper and lower thresholds. If the energy value falls outside the valid energy range defined by these thresholds, the event is considered invalid and discarded, and the count of rejected events is incremented by one. Conversely, if the energy falls within the threshold range, it is labeled as a valid event. The energy value is then digitized, with a 9-bit digital word for an energy value in the range from 2 keV to 30 keV. In the digitization process, each bit corresponds to an energy value of 60 eV.

- **Generate event packet**: Different types of event packets are generated depending on the observation mode and are subsequently transmitted to the PBEE. The energy formats differ between standard and high-rate observation modes. In standard observation mode, the energy of each triggered channel is provided, while in high-rate observation mode, only the total energy is presented to reduce the amount of data transmitted.

4.3 MBEE Preliminary Test and Analysis

The preliminary test and analysis of the MBEE is a critical step in the verification and debugging of the system, including the measurement of the power supply and the verification of the basic functions of the FPGA program. Power supply measurement focuses on evaluating power supply values, noise level, and stability for long-term operation to ensure the reliability and consistency of system power supply. In terms of verification of basic FPGA program functions, the MBEE-PBEE interface must be implemented for

testing, which is an interface based on the UART protocol. Since the MBEE is currently in the preliminary design phase, it is necessary to reduce variables as much as possible. Therefore, the MBEE-PBEE interface is simulated by using the FT232H chip from FTDI® and directly connected to the PC. Telecommands are sent through this interface, and responses from the MBEE are transmitted to the PC. In this section, some basic operations mentioned in Section 4.2 will be conducted to verify the interface connectivity and basic functionality of the FPGA circuit on the MBEE. The analysis of the circuit mainly includes the selection and evaluation of the baud rate of the MBEE-PBEE interface during the data transmission, as well as the calculation and calibration of the time error. For the baud rate of the data transmission, it is necessary to focus on analyzing the relationship between the baud rate, the system dead time, and the event rate (the average flux of X-ray photons). To ensure stable system operation and controllable power consumption, it is essential to select an appropriate baud rate that minimizes the event loss rate. Time error is the critical component of the housekeeping data, which is used for the precise calibration of the event time tagging. A thorough analysis of the error sources of the system clock enables high-precision time marking and effective error compensation.

4.3.1 Low Voltage Power Supply System

The MBEE requires four specific voltages for operation: 1.2 V, 2.5 V, 3.3 V (Analog), and 3.3 V (Digital). To supply these voltages for the MBEE, a dedicated power supply circuit was designed specifically for the preliminary circuit measurement and testing. This power supply circuit takes a +5 V input as its power source and uses the LMZ10504TZ-ADJ/NOPB voltage converter from Texas Instruments® to generate the required output voltages. Figure 4.19 provides a 3D model of the power supply circuit, compatible with the MPSU interface on the MBEE. This figure also illustrates the power-on sequence, confirming that all necessary output voltages are directly generated by the power supply circuit.

Table 4.15 shows the measured values of the four voltages, the corresponding current values, and the level of voltage noise after turning on and downloading the FPGA program. The noise is evaluated using the RMS value calculated after removing the DC component. Long-term testing revealed no significant heating issues in the circuit, effectively ruling out short-circuit problems.

4.3.2 PBEE-MBEE Interface Simulation Test and Analysis

As mentioned in Section 4.1, the PBEE-MBEE interface involves both data transmission and clock distribution. During the preliminary testing phase, the clock signal was generated internally using the FPGA's internal clock module combined with the PLL, and a UART interface based on FT232H was designed for the telecommands and data transmission between the MBEE and the external device. We will estimate the event loss

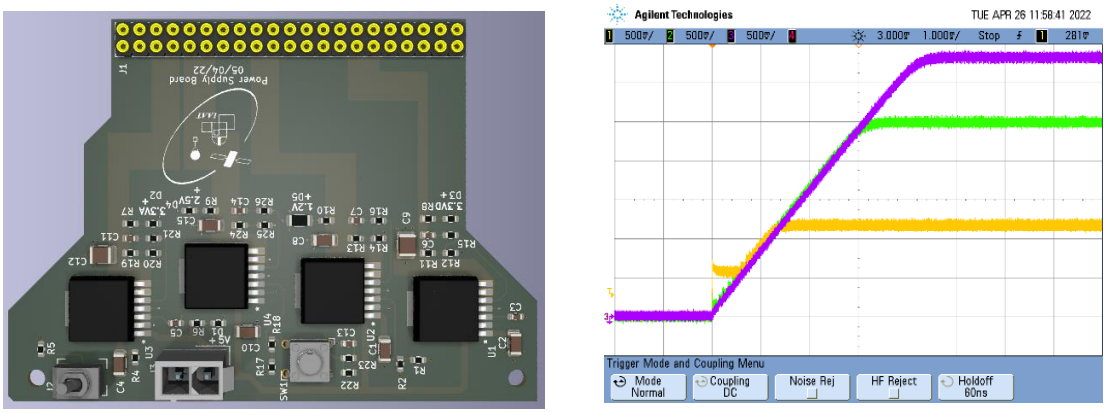

Figure 4.19: The 3D model of the power supply board and the power-on sequence test result.

Table 4.15: Measured Values of MBEE Power Supply Voltages

Voltage (V)	Measured Voltage (V)	Current (mA)	Noise level RMS (V)
1.2 V	1.160	422.3	0.0182
2.5 V	2.468	128.2	0.0199
3.3 V (Analog)	3.250	9.835	0.0192
3.3 V (Digital)	3.258	233.8	0.0134

rate during the transmission of event packets at a baud rate of 2 Mbps, which is determined based on the event rate and the required speed of the PBEE to poll the MBEE. The analysis emphasizes a comparison between the system dead time and the X-ray flux. In standard observation mode, the length of the data packet generated by an event involving three anodes reaches a maximum length of 18 bytes. At a baud rate of 2 Mbps, the transmission time is 90 µs, which is less than the dead time of the detector assembly 135.68 µs calculated by Equation (4.8) in Section 4.2.10. In the current mode of OWB-1 data conversion and transmission to the MBEE, even if no additional memory is allocated for storing science data packets, these will not be lost due to communication rate limitations. This is because during the dead time after the detector completes an event, the last data transmission has already been completed, and the communication interface has already been in an idle state. Only the first stage of the pipeline contributes to the system's dead time because the pipeline concept was applied in the data processing. Therefore, the system's dead time is determined predominantly by the detector assembly's dead time.

Each anode channel of the LAD detects approximately 1 count per second, even during the observation of a bright source such as the Crab Nebula (Feroci *et al.*, 2018). The num-

ber of events occurring in one channel within the detector assembly's dead time follows a Poisson distribution: $X \sim \text{Poisson}(\lambda)$, where λ can be calculated by the detector assembly's dead time $Dead\ Time_{\text{DA}}$ and the event rate in each channel $Event\ Rate_{\text{one\_channel}}$ through Equation (4.9):

$$\lambda = \frac{Dead\ Time_{\text{DA}}}{Event\ Rate_{\text{one\_channel}}} = 1.36 \times 10^{-4}\ \text{count} \tag{4.9}$$

The probability $P(0)$ that no event occurs in one channel during the dead time is given by:

$$P(0) = e^{-\lambda} \tag{4.10}$$

For all 112 channels in one detector half, the probability that no event occurs in any of the channels during the dead time is:

$$P_{\text{all}}(0) = (P(0))^{112} = e^{-112\times\lambda} \tag{4.11}$$

Therefore, the probability that at least one event occurs in any of the 112 channels during the detector component's dead time is:

$$P_{\text{at least one}} = 1 - P_{\text{all}}(0) \approx 1 - 0.985 = 0.015 = 1.5\% \tag{4.12}$$

This analysis of event rate and dead time indicated that there is a 1.5 % event loss probability at a baud rate of 2 Mbps, which is worse than the requirement of 0.5 % as Table 2.1. Therefore, in the future, we must improve the way OWB-1 transmits data to MBEE. In the new version of OWB-1, only the data generated by the triggered channel is transmitted. Take three channels being triggered as an example. Under the same conditions, the dead time can be calculated in Equation (4.13). The new transmission time is calculated based on the amount of data transmitted and the transmission rate (25 Mbps), which is about 3 µs. Now, the new dead time is 23.48 µs.

$$Dead\ Time_{\text{DA new}} \approx 8 \times T_{\text{single conversion}} + T_{\text{transmission new}} \tag{4.13}$$

According to the above probability model, the probability of event loss corresponding to the current dead time is approximately 0.26 %. However, in this case, the transmission time for each event from the MBEE to PBEE will be much longer than the dead time of the detector assembly. Therefore, while improving the transmission speed of the MBEE-PBEE interface, an external data storage unit with a certain depth must be equipped to temporarily store science data packets. In particular, considering that the PBEE interface needs to process data from 8 detectors in one MBEE, more research and optimization are still required in the future for the transmission rate, storage depth, and system carrying capacity under common X-ray flux conditions. A unique capability of eXTP, particularly the LAD, is achieving high-throughput observations up to 15 Crab (Minervini *et al.*, 2024), which places higher requirements on data storage and transmission. Therefore,

the optimization of data storage and transmission will be the focus of the next research on the MBEE-PBEE interface. However, when LAD is working normally, we will not allow the transmission rate of the PBEE interface to become a bottleneck that limits the high-throughput observation capability of the system. Therefore, by improving the data output transmission mode of OWB-1 (transmitting only the trigger channel data), the performance requirements of LAD in terms of dead time can be effectively met.

4.3.3 Basic Functional Test

The connection test, MBEE operation mode switching test, and the generation of dummy science data packets represent three fundamental functions, as detailed in Section 4.2.5, Section 4.2.4, and Section 4.2.9. This is because these three tests operate independently of other MBEE components, such as the FEE interface, MPSU interface, and housekeeping circuits, only relying on the FPGA part and PBEE interface. Here we will conduct these fundamental tests.

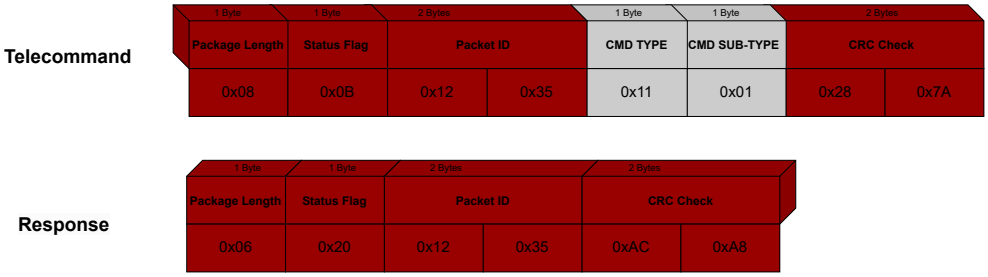

Figure 4.20: The telecommand and its response to the connection test.

Connection Test

After powering on and the program is downloaded, the telecommand displayed in the upper part of Figure 4.20 is sent, and the response is received as expected, confirming a successful connection.

MBEE Operation Mode Switching Test

After powering on and downloading the program, the MBEE defaults to standby mode. Sending the telecommand shown in the upper part of Figure 4.21 switches its operation mode to the standard observation mode. The lower part of Figure 4.21 illustrates the expected response, confirming the successful mode switching.

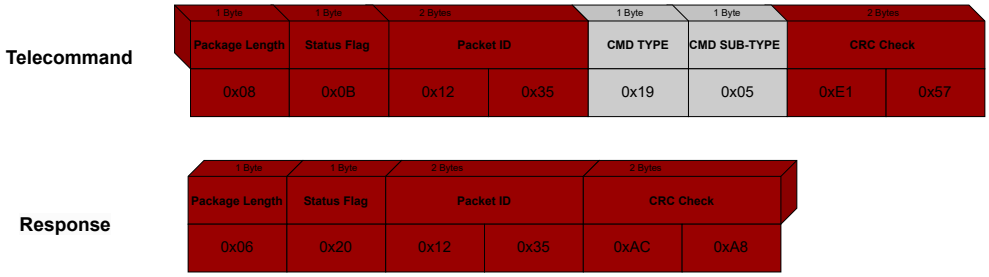

Figure 4.21: The telecommand and its response for switching the MBEE from standby mode to standard observation mode.

Next, a telecommand is sent to switch the operation mode to the configuration mode. An error message, as shown in Figure 4.22 indicating an invalid command was received, as expected, since switching to other modes is only available after first returning to the standby mode.

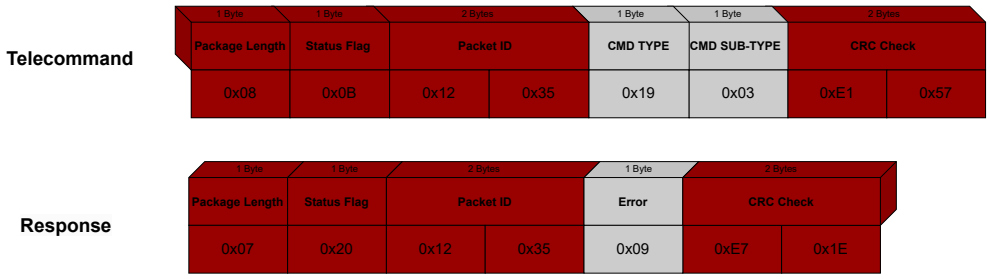

Figure 4.22: The telecommand and its error message for switching the MBEE from standard observation mode to configuration mode directly.

Generate Dummy Science Data Packet Test

Generating dummy science data packets through an external trigger signal is crucial for assessing the stability and reliability of the PBEE interface in transmitting science data. After powering on and downloading the FPGA program, switch the MBEE operation mode to the standard observation mode. First, use the external trigger button to simulate generating an unacceptable event, which will be rejected, then simulate generating a one-channel event, send a telecommand to obtain science data, and an event packet shown in Figure 4.23 will be received.

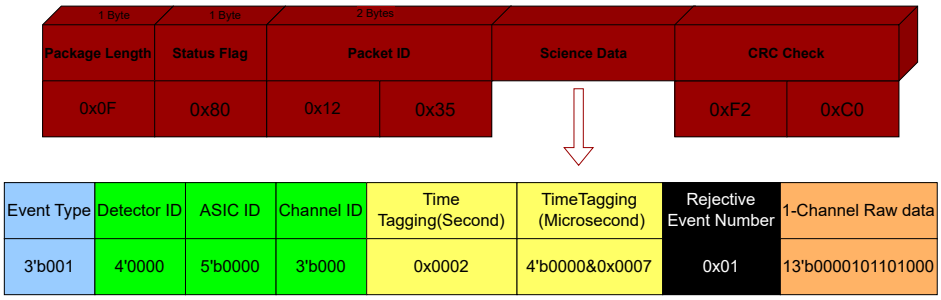

Figure 4.23: An event science data packet is generated with the following characteristics: the event type is identified as a one-channel event, with a time tag of 1.000007 s. The packet also records one rejected event, corresponding to the simulated unacceptable event. Additionally, the raw energy value is reported as 360 (decimal).

4.3.4 Time Tagging Calibration

The accuracy of the timestamp is determined by the accuracy of the two clocks. Since the PPS is synchronized with the GNSS time and has high stability, the timing accuracy is predominantly influenced by the 10 MHz clock.

Assuming that the actual frequency of the 10 MHz clock is f_{actual}, and the ideal frequency is 10 MHz ($f_{\text{ideal}} = 10$ MHz), the deviation is calculated using Equation (4.14):

$$\varepsilon = \frac{\Delta f}{f_{\text{ideal}}} = \frac{f_{\text{actual}} - 10\ \text{MHz}}{10\ \text{MHz}} \tag{4.14}$$

Upon receiving the trigger signal, record the second counter value N_{second} and the microsecond counter value $N_{\text{microsecond}}$ mentioned in Section 4.2.2. Then the calibrated time can be calculated by Equation (4.15):

$$t_{\text{calibrated}} = N_{\text{second}} + \frac{10 \times N_{\text{microsecond}}}{10\ \text{MHz} \times (1+\varepsilon)} \tag{4.15}$$

In this chapter, we have introduced the design and implementation process of the MBEE in detail, including the selection of its chips, structural design, layout and routing, and manufacturing processes. In addition, we have introduced the FPGA program architecture and its implementation, especially its working mechanism in terms of control functions and time-energy reconstruction of X-ray events. Through a series of basic tests, the working ability of the MBEE as a core component of back-end electronics has been verified.

Chapter 5

System Joint Test

5.1 Module Back End Electronics Interfaces Establishment

5.1.1 MPSU Simulator

The MPSU simulator is used in the early phase of the MBEE development to build the MPSU interface and verify MPSU-related programs. The MPSU simulator is designed based on a circuit development module equipped with ADC, DAC, and multiple I/O ports. These I/O ports are used to simulate the real input and output signals of the MPSU, and they are connected to the MPSU interface on the MBEE. As previously mentioned, the MBEE handles voltage monitoring and configuration via its onboard ADC and DAC. This implies that the MPSU interface operates entirely at low voltage levels, with all high voltage (HV) and medium voltage (MV) conversions being managed internally by the MPSU. Consequently, this module can effectively simulate the behavior of the MPSU interface, and the "implementation" of these voltage operations can be visualized through the software interface.

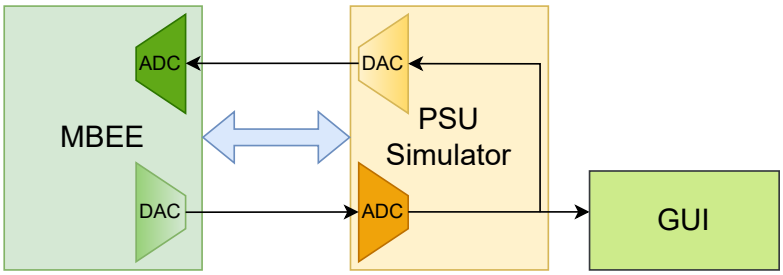

Figure 5.1: The working principle of the MPSU simulator and its interface with MBEE.

Figure 5.1 shows the working principle of the MPSU simulator and its interface with MBEE. The MBEE controls the voltage change of the DAC in the MBEE to set the

relevant voltages for the MPSU interface. This voltage is simultaneously captured by the ADC on the MPSU simulator, which acquires the corresponding value and digitizes the voltage value. The digitalized value is then processed by the software interface, which calculates and outputs the change of the voltage on the Graphical User Interface (GUI). The DAC on the MPSU will get the digitized output of the ADC in the MPSU directly and then the DAC generates the voltage corresponding to the digital output, and the ADC on the MBEE samples the voltage, thereby completing the monitoring of the MPSU voltage. This closed-loop process ensures accurate voltage configuration and monitoring simulation.

MPSU Voltage Configuration

First, we configure the MBEE to observation mode, as this is the only mode in which the HV and MV settings can be operated. Then, a series of voltage-related operations can be performed based on the telecommands introduced in Section 4.2.6 in Chapter 4. Initially, we enable the MV, which leads to the gradual increase according to the predefined ramp-up slope until it reaches 130 V. Next, we send the appropriate telecommands to enable the HV, and set the HV to 1500 V, as Figure 5.2 showing the structure of the telecommand to set the HV to 1500 V and its response of the HV setting.

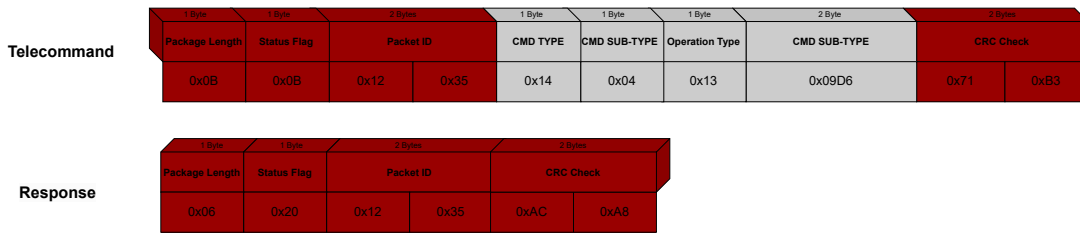

Figure 5.2: The HV setting telecommand and its response.

Similarly, the HV will rise gradually according to the specified ramp-up slope. After maintaining the HV for a certain duration, turn the HV off, observing that the HV decreases slowly. Once the HV is completely disabled, we then disable the MV, which also decreases gradually until it returns to zero. As shown in Figure 5.3, the blue curve presents the change of the MV, while the red curve presents the HV change. The HV can only be enabled and set when the MV is enabled. If the voltage-related telecommands are sent in the other operation mode rather than the observation mode, or to enable the HV during the MV is disabled, the MBEE will respond with an error.

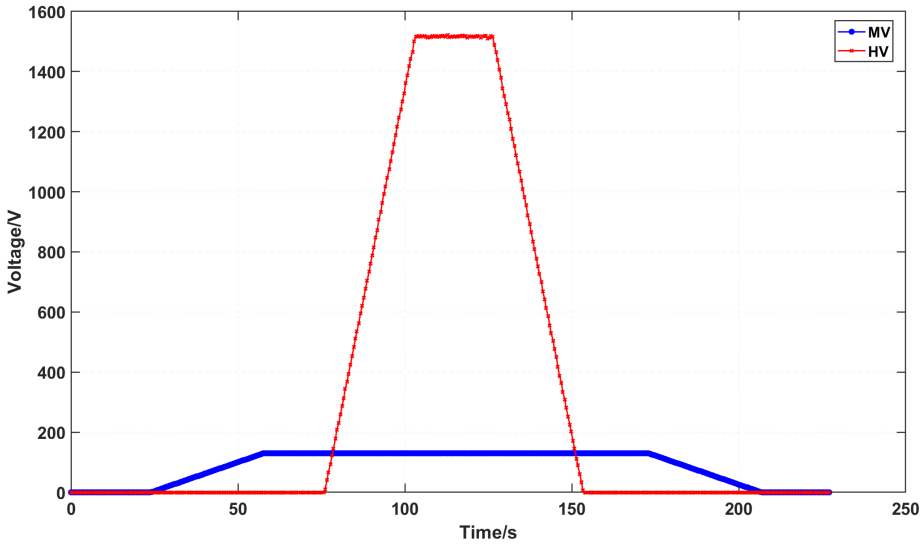

Figure 5.3: HV curve and MV curve. The HV is enabled and set to 1500 V when the MV is enabled, then reduced to 0 V.

Get Housekeeping data

To obtain all relevant parameters, we perform a housekeeping data acquisition test after both the MV and HV are enabled and configured. Table 5.1 presents the parameters we get, including the HV, MV, LVs, and their currents, as well as the current operation mode and time error.

Table 5.1: Housekeeping Data from a Single Measurement

Type	**Item**	**Test value**
Operation mode		Observation mode
LV	1.2 V	1.16 V
	2.5 V	2.47 V
	3.3 V (Digital)	3.25 V
	3.3 V (Analog)	3.26 V
MV	130 V	127.94 V
HV	1500 V	1487.46 V
Current	1.2 V	422.3 mA

Continued on next page

Table 5.1 – *Continued from previous page*

Type	Item	Test value
	2.5 V	128.2 mA
	3.3 V (Digital)	233.8 mA
	3.3 V (Analog)	9.8 mA
Time Error		-0.05 μs/1 μs

5.1.2 FEE Simulator

In this part, the FEE simulator will be introduced. The FEE simulator plays a critical role in the initial phase of the MBEE development, especially in establishing the FEE-MBEE interface and enabling the design of MBEE's data processing pipeline. During the early parallel development of the FEE and MBEE hardware and the FPGA program, the simulator serves as an essential provider of real detector signals. Specifically, it emulates the FEE's output when the detector interacts with X-ray photons. By processing these simulated signals, MBEE validates its algorithms for reconstructing the energy of the X-ray, thereby verifying the entire detection chain's functionality for X-ray event processing.

Figure 5.4 shows the schematic diagram and physical diagram of the detection chain based on the FEE simulator. The electronics system consists of the MBEE and FEE simulator, the latter based on the DevKit evaluation board, which is a demonstration board for the NG MEDIUM CLGA625 chip. In actual application scenarios, the connection between MBEE and FEE is through a flexible PCB as shown in Figure 5.4. However, when interfacing with the FEE simulator during the development and testing phases, an adapter board is necessary to connect the connector on the flexible board with the connector on the FEE simulator. In order to improve the mechanical stability of the system, especially to protect the flexible PCB, a special aluminum support platform was designed to fix the entire electronic system.

Figure 5.5 shows a GUI that basically plays the role of simulating a large area multi-channel SDD. The GUI is designed to generate the energy channel distribution of a single X-ray photon event, that is, to generate the output of the OWB-1 for the channels involved in this X-ray event. For this GUI, the energy button is used to generate the energy of the X-ray, and the position coordinates in the lower left corner are the coordinates of the X-ray incident point. Different energy distributions are generated based on the analysis of the detector in Chapter 3. Notably, this coordinate system corresponds to a detector half and aligns with Figure 3.4: the horizontal axis (0–1) represents the detector length along the anode distribution direction, while the vertical axis (0–1) corresponds to the vertical distance between the photon incident position and the edge of the anode distribution (1 corresponds to the maximum drift distance). After obtaining the distribution of

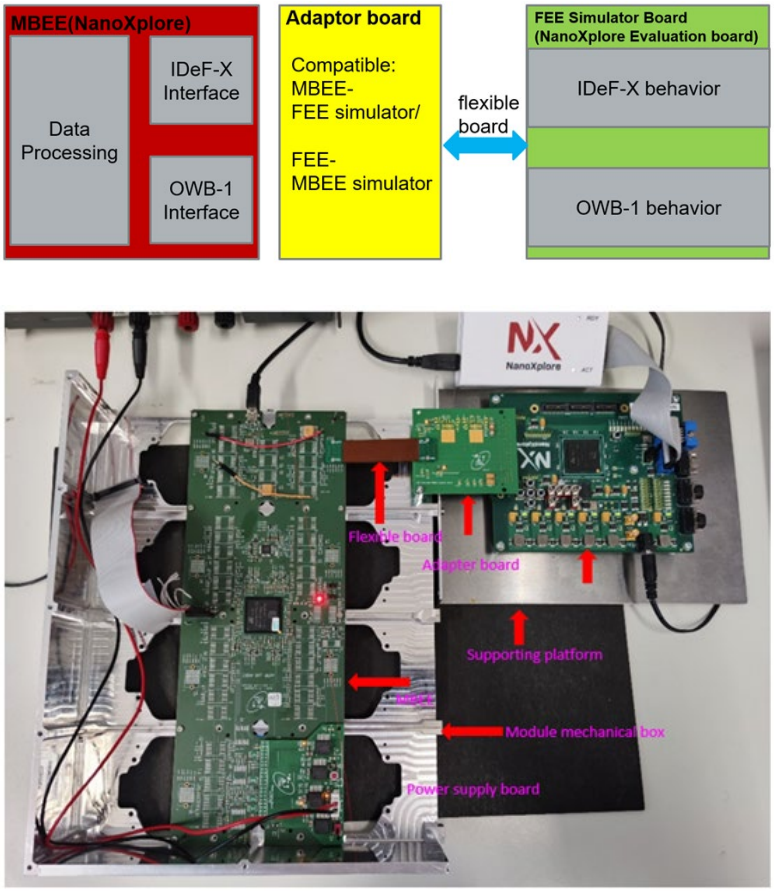

Figure 5.4: Schematic diagram and physical diagram of the electronics test system based on the FEE simulator.

total energy on the relevant channels, the software is required to complete the processes of energy deposition, charge generation, charge signal conversion to the voltage signal, signal amplification, peak extraction, and analog-to-digital conversion. Therefore, in the software, the OWB-1 output data corresponding to the triggered channels is generated based on the average ionization energy, the gain of the charge sensitive amplifier, the gain of the main amplifier, and the relationship between the OWB-1 input signal voltage and output data discussed in Chapter 3. The OWB-1 output data will be transmitted into the FEE simulator based on the UART interface. Besides, a series of parameters related to the energy reconstruction are also stored in the software for the conversion from the photon energy to the voltage signal, mainly including the gain of each electronic channel and the trigger threshold of each channel. These parameters are crucial for us to reconstruct the energy in the channels of one X-ray event. It is also worth noting that these parameters are actually IDeF-X HDBD parameters. Another data that should be gener-

ated and stored in software is a noise model, which will emulate common mode noise and be deducted in the data processing pipeline.

Figure 5.5: The GUI is used to simulate the large area multi-channel SDD in order to get the energy distribution on the channels of the detector half.

The implementation of the FEE simulator is based on the evaluation board and the FPGA program. Figure 5.6 shows the FPGA program architecture. In general, in order to reduce the complexity of the FEE simulator program as much as possible, we let the main calculation process be handled by the software mentioned above, and the FEE simulator is only responsible for interface establishment and data transmission. In addition, the FEE simulator also assumes the function of parameter storage. The first part of the parameters is the key parameters of IDeF-X HDBD (such as thresholds and gains of each channel). Each of these parameters has an initial value that is stored in the FEE simulator as well as the GUI mentioned above. The modification of these parameters will be conducted by sending telecommands to the MBEE. When the MBEE sends a telecommand to read these parameters, the FEE simulator can respond “directly and quickly”; when MBEE modifies the parameters, the FEE simulator can also “directly and quickly” update these parameters and notify the GUI through the UART interface, and the GUI will update these parameters synchronously. The second part of the parameters is each channel’s pedestal value. The pedestal values are stored in the FEE simulator and the MBEE, and they are usually not changed because they are a set of fixed values for a certain detector. If the pedestal value needs to be updated, the user should send the related telecommand to the MBEE in the configuration mode. The third part parameter is a set of noise data for the 112 channels. The common mode noise data are generated

on the GUI and sent and stored to the FEE simulator. If we don't generate and send them manually again, we use the same noise model for the different X-ray event simulations. If we want to update the noise model, we just update it using the GUI during the idle time through the UART interface. The reason why we distinguish the classification and storage location of parameters is that we want to reduce the transmission data volume as much as possible and improve transmission efficiency, only the number of the triggered channels (event type), position (the triggered channel with the smallest ID, which is from 0 to 111), and output data of the triggered channels (no more than three channels) will be transmitted from the GUI to the FEE simulator. The superposition of the pedestal and noise values is implemented in the FEE simulator, which means that only a maximum of six addition operations need to be completed.

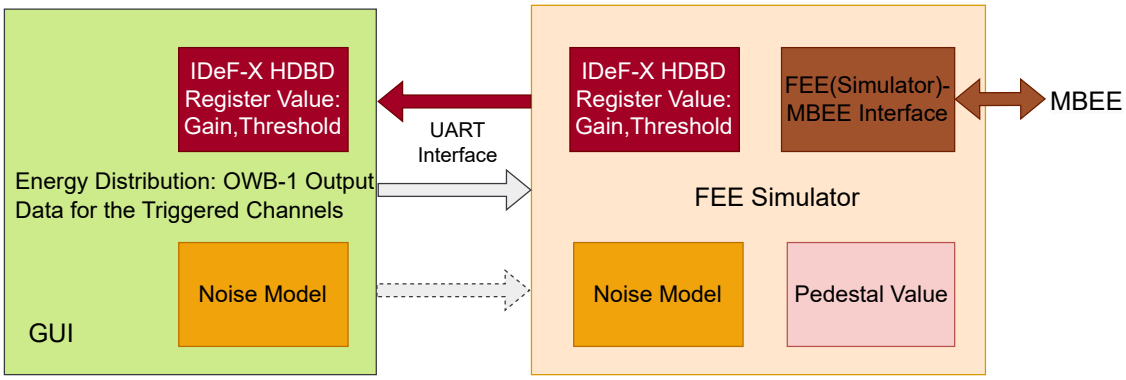

Figure 5.6: Schematic diagram of the FPGA program architecture. As a simulator based on the FPGA, to reduce the complexity of the program as much as possible, the calculation process is mostly handled in the GUI and its software. The FEE simulator board plays a more important role in data storage and interface establishment.

Here, we provide a brief overview of the simulation process for the first-phase FEE simulator. Since our primary goal is to validate the MBEE-FEE interface and develop the data processing pipeline, this phase focuses on simulating a single detector half, which consists of 112 anode channels. As each detector half operates independently, this setup is sufficient to accomplish both the interface test and data processing pipeline development.

Slow Control of FEE Simulator - MBEE Interface Test

In order to demonstrate the slow control part of the FEE simulator-MBEE interface, we use the waveform of the read and write of one of the registers to prove the successful establishment of this interface. According to the datasheet of IDeF-X HDBD, Register # 1 is a register for tuning the internal leakage current, which is used to compensate for

the internal current generated in IDeF-X HDBD when there is no detector to the input. Here we will use the FEE simulator and the MBEE to simulate the following process: first, get the default value of Register # 1, then modify the value of the register to another value, and read the value of the register again. To perform these operations, the MBEE should be entered into configuration mode.

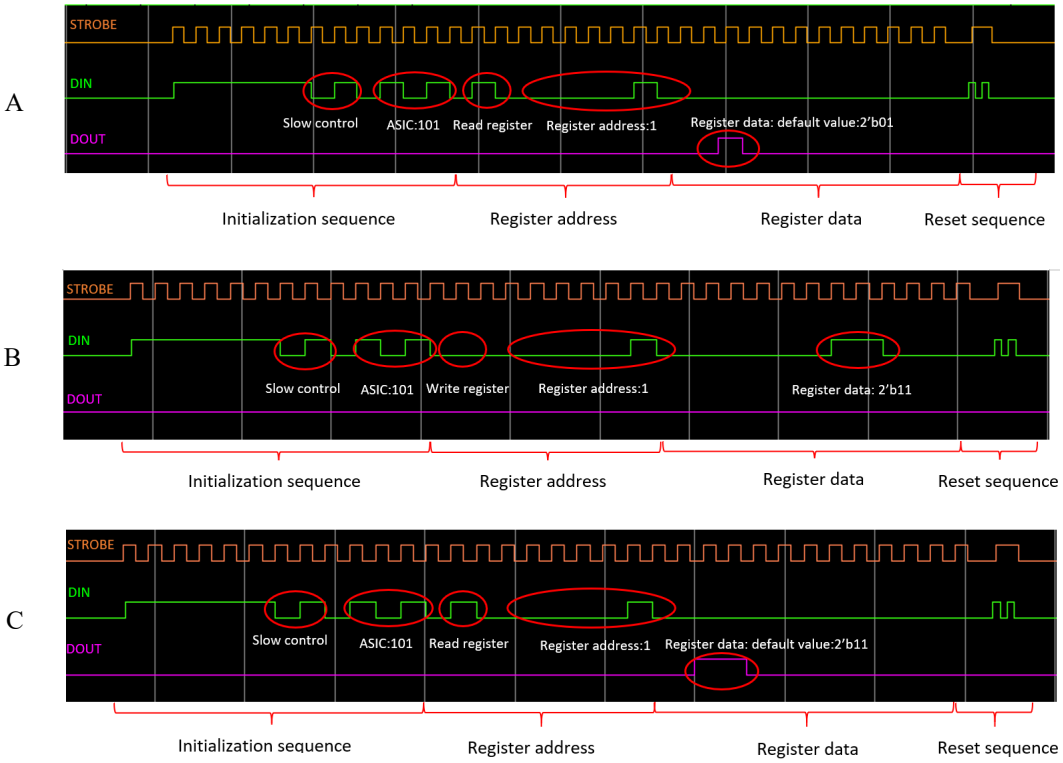

Figure 5.7: Timing diagram of the slow control process of IDeF-X HDBD, which is one of the important parts of the FEE simulator-MBEE interface. Here, use the configuration of Register # 1 to verify this process.

Figure 5.7 shows the timing diagram of the slow control process: Part A is the process to read out the default value (2'b01) of this register (address:7'b0000001) in IDeF-X HDBD # 5 (3'b101); Part B is the process to change the value from the default value to a new value of 2'b11; and Part C is the process to read out the new value of this register.

Although the configuration of OWB-1 is not the main focus of this simulation, however, since its configuration is also an important part of the MBEE in the configuration mode, we will also briefly verify the interface test of OWB-1's slow control process. Here we use Register #11 (6'b001011) to test, which is a register to control the PLL's mode of OWB-1, and the details of the register can be found in the datasheet of OWB-1

from the CEA team. Figure 5.8 presents this process: In Part A, write in Register #11 (4'b1011) of OWB-1 #4 (3'b100) with a data of 7'b1011010; and in Part B, read the value of this register in OWB-1.

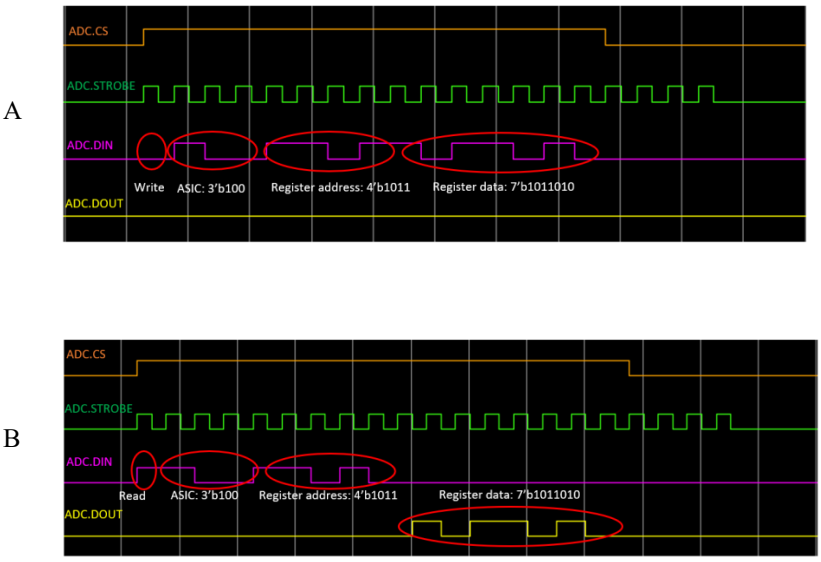

Figure 5.8: Timing diagram of the slow control process of OWB-1, which is one of the important parts of the FEE simulator-MBEE interface. Here, use the configuration of Register # 11 to verify this process.

Event Reading of FEE Simulator- MBEE Interface Test

In this part, we verify the event reading process of the FEE simulator-MBEE interface. As soon as a channel of at least one IDeF-X HDBD has been hit and the peak detector level is higher than the threshold, the chip will set the common TRIGGER signal to '1' and the bit corresponding to the hit channel number to '1' in the event register. Then the readout sequence begins to run, and the process will transfer the triggered ASIC map and the triggered anode map. After this, the energy of the channels of the triggered ASICs will be output according to different modes: automatic mode, all mode, and demand mode. For the FEE simulator, we will focus on the event reading. According to the pitch parameter of the large area multi-channel SDD used in the LAD and the size of the IDeF-X HDBD, only eight input channels of IDeF-X HDBD are used and connected to the anodes of SDD (IN0, IN4, IN8, IN12, IN18, IN23, IN27, IN31). Here we will use the FEE simulator to simulate one event that the 0th and 4th channels of IDeF-X HDBD #7 (1'b111) are triggered. Figure 5.9 shows the timing diagram of event reading, where

a two-channel event was simulated. It is worth noting that the event reading process happens when the MBEE enters into the observation mode.

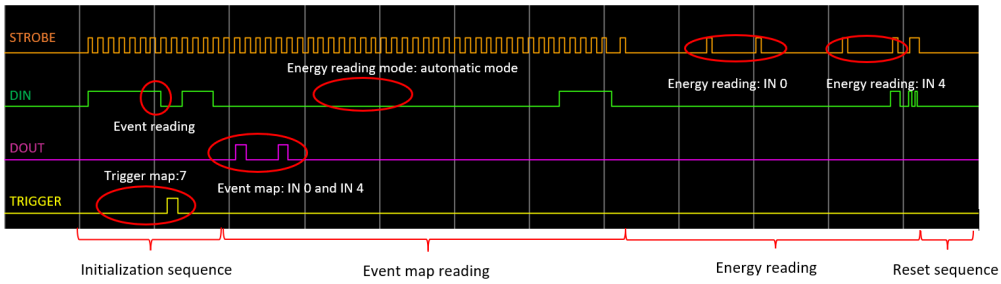

Figure 5.9: Timing diagram of the event reading process of IDeF-X HDBD, which is one of the important parts of the FEE simulator-MBEE interface.

5.2 System Joint Test

This section uses the proposed FEE simulator-MBEE system to simulate the full process of X-ray event detection, energy reconstruction, and science data packet generation. Through a systematic analysis of these processes, we demonstrate the system's ability to support the fundamental operations of a detector half. We will further extend this system to a complete FEE interface and evaluate the feasibility of fully implementing the FEE simulator-MBEE FPGA program for all eight FEE interfaces on a single MBEE in the future.

Energy Distribution in the Detector Channels

We use the GUI and the algorithm mentioned in the previous section. ^{55}Fe is an artificial radionuclide that decays into ^{55}Mn primarily through electron capture. At the same time, characteristic X-rays are released, with the main characteristic energies of 5.9 keV (Fe-K$_\alpha$) and 6.49 keV (Fe-K$_\beta$). Among them, the 5.9 keV K$_\alpha$ line accounts for the main proportion, around 88 %. It does not emit beta particles during this process, so its decay process is relatively "clean" and is often used to calibrate low-energy X-ray detectors. Here we use the 5.9 keV X-ray photons generated by ^{55}Mn for simulation, and the incident position coordinates are set to (0.55, 0.5). According to the description of the coordinate system in the previous section of this chapter and the calculation program embedded in the GUI and software, the energy distribution can be obtained as shown in Figure 5.10, which shows the distribution of energy (charge) of a 5.9 keV photon interacting with the detector: the ratio of the energy in the two channels is approximately 1:4.

The calculation process of the total charge is introduced in Chapter 3. The total charge is calculated by the following equations, which is about 0.263 fC.

$$\text{Number of electron-hole pairs} = \frac{5.9\,\text{keV}}{3.6\,\text{eV/pair}} \approx 1644\,\text{pairs} \tag{5.1}$$

Consequently, the total charge generated is:

$$\text{Total charge} = 1644\,\text{pairs} \times 1.602 \times 10^{-19}\,\text{C/pair} \approx 2.63 \times 10^{-16}\,\text{C} = 0.263\,\text{fC} \tag{5.2}$$

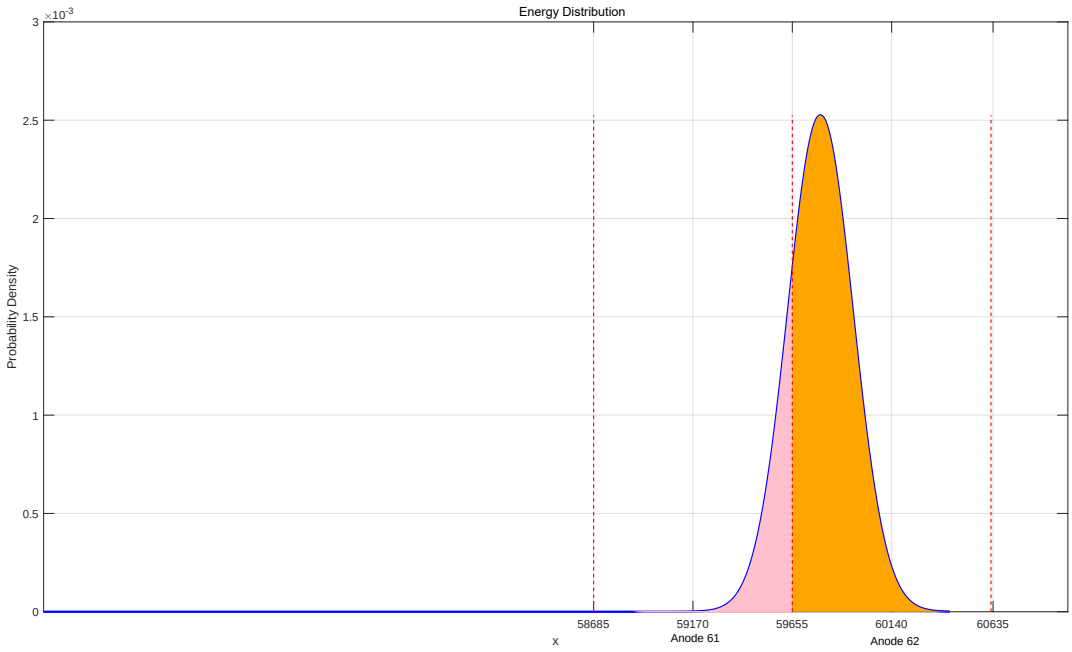

Figure 5.10: Energy distribution on the anodes after a 5.9 keV photon, generated by ^{55}Fe (^{55}Mn), interacts with the detector and drifts from the set incident coordinates.

Voltage Peak Acquirement

The GUI and software will calculate the peak value of the output signal based on the charge, which is introduced in Chapter 3. The upper part of Figure 5.11 presents the process of the voltage peak acquisition based on the charge distribution, while the lower part of Figure 5.11 includes the pedestal value of the anode channels and the baseline with noise data.

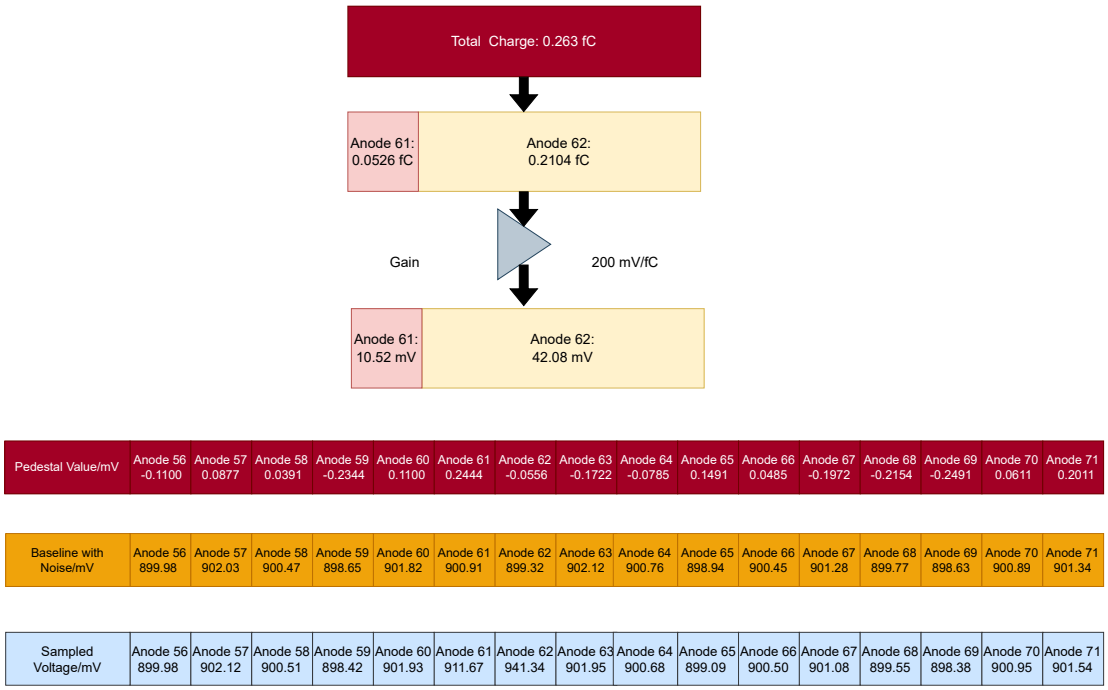

Pedestal Value/mV	Anode 56 -0.1100	Anode 57 0.0877	Anode 58 0.0391	Anode 59 -0.2344	Anode 60 0.1100	Anode 61 0.2444	Anode 62 -0.0556	Anode 63 -0.1722	Anode 64 -0.0785	Anode 65 0.1491	Anode 66 0.0485	Anode 67 -0.1972	Anode 68 -0.2154	Anode 69 -0.2491	Anode 70 0.0611	Anode 71 0.2011
Baseline with Noise/mV	Anode 56 899.98	Anode 57 902.03	Anode 58 900.47	Anode 59 898.65	Anode 60 901.82	Anode 61 900.91	Anode 62 899.32	Anode 63 902.12	Anode 64 900.76	Anode 65 898.94	Anode 66 900.45	Anode 67 901.28	Anode 68 899.77	Anode 69 898.63	Anode 70 900.89	Anode 71 901.34
Sampled Voltage/mV	Anode 56 899.98	Anode 57 902.12	Anode 58 900.51	Anode 59 898.42	Anode 60 901.93	Anode 61 911.67	Anode 62 941.34	Anode 63 901.95	Anode 64 900.68	Anode 65 899.09	Anode 66 900.50	Anode 67 901.08	Anode 68 899.55	Anode 69 898.38	Anode 70 900.95	Anode 71 901.54

Figure 5.11: The process of the voltage peak acquisition based on the charge distribution, which includes pedestal offset and common mode noise.

Location, Event Type and Analog-Digital Conversion

The dynamic range of OWB-1 is from 0.84 V to 2.84 V, a total of 2 V, and the resolution of OWB-1 is 13 bits. Therefore, it can be calculated that each bit of OWB-1 corresponds to a voltage of 0.244 mV. Based on the noise level and taking the pedestal value into consideration, an appropriate threshold is set to determine which anode channels are triggered. Following the standard of the valid event in Chapter 3, we know this event is a valid event and then get the event type and the location of the event: the event type is a 2-channel event, and the location of the event is channel #5 (3'b101) and channel #6 (3'b110) of IDeF-X HDBD #7 (5'b00111). According to the datasheet of OWB-1, there are two registers to store the value of each channel, which has been discussed in Chapter 3. Figure 5.12 shows these registers for the two triggered channels, whose original voltages are calculated based on Figure 5.11, and they are 911.67 mV and 941.34 mV, respectively. The DLL encoder value and the Gray code of the PLL value represent the 13 bits of the voltage. The channel address means the input channel of OWB-1. According to the instruction of the OWB-1 in Chapter 3, there are 16 differential input channels that are connected to 14 IDeF-X HDBD analog outputs, and the remaining two differential channels are left floating. So the anodes sharing the same IDeF-X HDBD

use the same input OWB-1 channel, which is why the two parts of Channel Address in Figure 5.12 are the same.

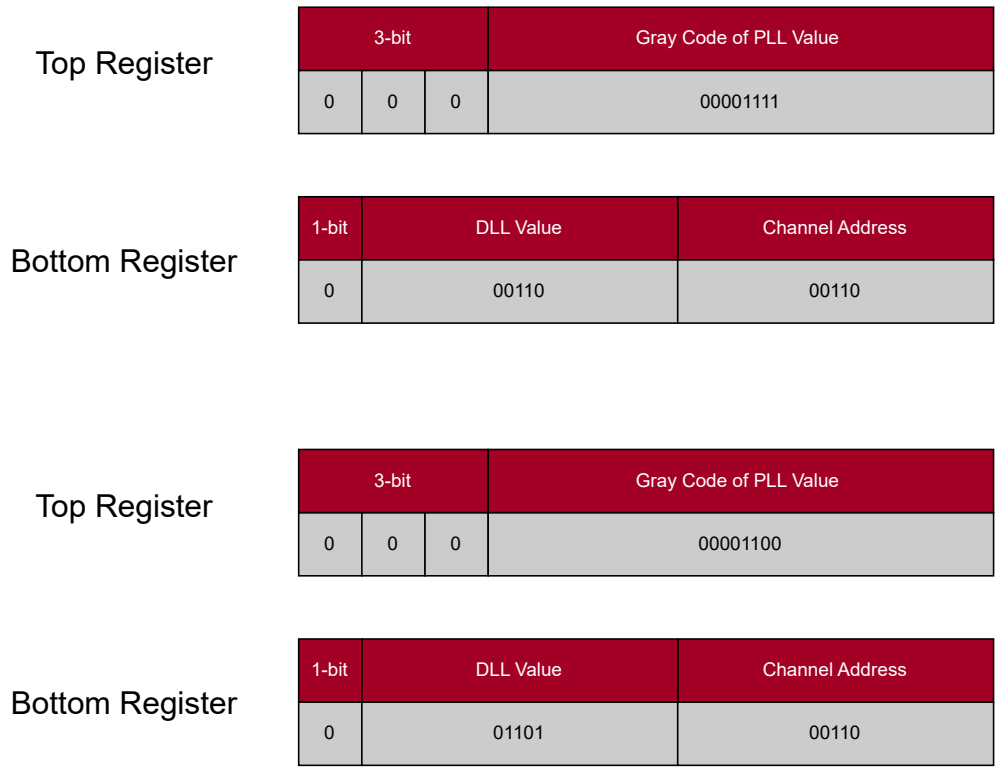

Figure 5.12: Two sets of registers to store the sampled data for the two triggered anodes. The upper two registers present the value of Anode 61, while the lower two registers show the value of Anode 62.

Sampled Data Transmission

After 8 cycles, 112 anode voltage values are stored in registers, and are serially output in sequence with a frequency of 25 MHz. This configuration is set by OWB-1 at this stage. Future research and development will optimize the analog-to-digital conversion that only the channels at the IDEF-X HDBD where the triggered channel is located will be converted to a digital signal to improve efficiency. The transmission process and the transmission time are mentioned in Section 4.2.10 of Chapter 4.

Data Processing Pipeline Implementation

Consider an extreme case where the event occurs on two edge channels of two adjacent IDeF-X HDBDs, as shown in Part A of Figure 5.13. In this case, processing data from two IDeF-X HDBDs is necessary. Therefore, in order to ensure the universality of the event processing program, we should consider at least two adjacent IDeF-X HDBDs when processing data. In this case, based on the energy distribution, we selected the IDeF-X HDBD responsible for Anode 56 - Anode 63 and the IDeF-X HDBD responsible for the channel Anode 64 - Anode 71. In the data processing, the data from these 16 channels should be processed. Figure 5.13 shows the three scenarios that describe how to choose the target IDeF-X HDBDs for the data processing pipeline.

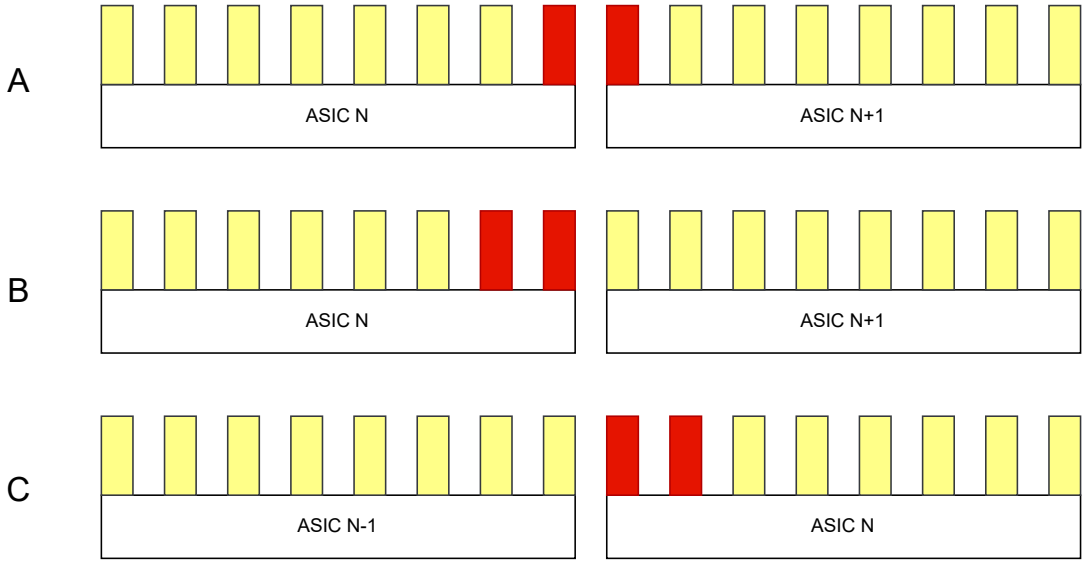

Figure 5.13: Three different situations for choosing the target IDeF-X HDBDs, and the selection method follows the principle of proximity: besides the IDeF-X HDBD that contains the triggered channel, another IDeF-X HDBD is selected that is closer to the triggered channel.

After selecting the 16 channels of data from the two appropriate IDeF-X HDBDs, we sort them out and restore them to 13-bit sampling data to facilitate our subsequent processing.

- **Pedestal subtraction**: In this step, we aim to correct the inconsistency in the anode pedestal caused by manufacturing process errors. Specifically, we will subtract the pedestal values stored in the MBEE from the sampled voltages of all 16 channels, as illustrated in Figure 5.11. For this specific example, after subtracting the

pedestal values, the actual values of these two triggered channels are 911.43 mV and 941.40 mV, respectively. It is important to note that this subtraction operation is performed on the digitized signals, rather than the analog voltage. The reason why the real voltage value is used to explain is to make it easier for readers to understand.

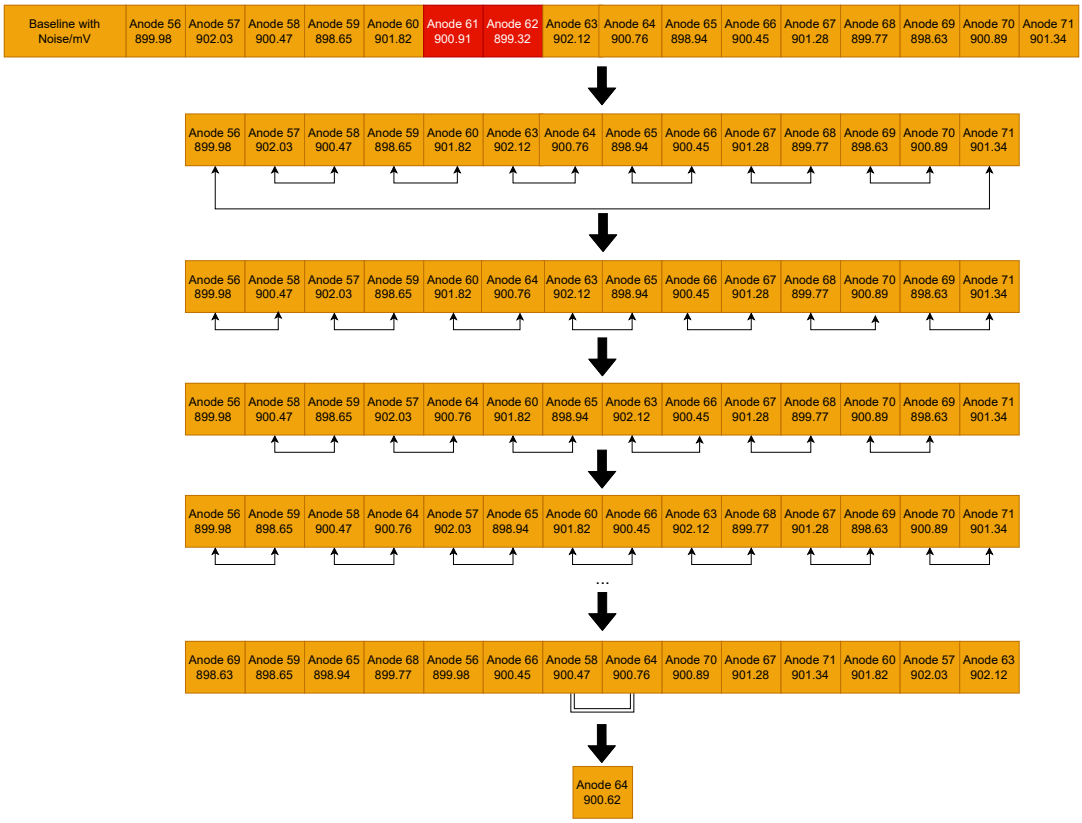

Figure 5.14: Working principle of the Odd-Even-Transportation-Sort (OETS) algorithm. There are several steps of comparing and swapping positions alternately. The first step is the odd bits, comparing and swapping 1 and 2, 3 and 4...; the second step is the even bits, comparing and swapping 0 and 1, 2 and 3...; repeat the above process until the middle value is obtained, which is regarded as the baseline level after deducting the common mode noise.

- **Common mode noise subtraction**: The common mode noise is calculated using the Odd-Even-Transportation-Sort (OETS) algorithm (Leighton, 1991) by using the untriggered channels of these 16 channels. We abandoned the method of summing and averaging these channels because it would consume more FPGA

resources. Figure 5.14 shows the principle of this algorithm. First, the triggered channel(s) should be excluded, then a series of parity comparisons and swaps. In the odd phase, compare all odd index pairs (such as index 1 and 2, 3 and 4, and so on), and if the first number is greater than the second, swap them. Then in the even phase, compare all even index pairs (such as index 0 and 1, 2 and 3, and so on). And repeat these operations several times, and the series of data will be arranged from small to large. We select the value in the middle (or the average of the two values in the middle) and regard it as common mode noise. For this example, the two values in the middle of the ranking are selected, and their average is calculated as the average baseline value after subtracting the common mode noise, whose value is 900.62 mV. The actual voltage of the two trigger channels can be obtained by subtracting the common mode noise from the sampled voltage values. Similarly, the operation is performed based on the digitized signals.

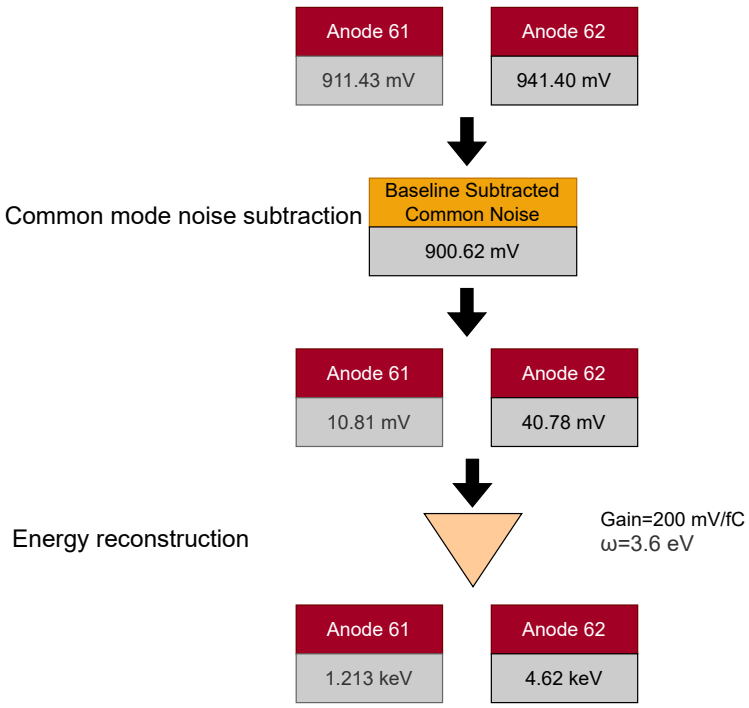

Figure 5.15: The process of common mode noise subtraction and energy reconstruction.

- **Energy reconstruction and Event threshold application**: Figure 5.15 presents the process of the common mode noise subtraction and energy reconstruction. The

energy range the LAD focuses on is between 2 keV and 30 keV, which is set as the lower threshold and upper threshold to identify the energy of the event.

- **Generate event packet**: According to the format definition in Section 4.2.9 of Chapter 4, now it is time to generate the science data packet. Figure 5.16 shows the science data packet in this simulation, the two orange boxes tell us the energies of the two channels, and the total energy of the incident X-ray photon is 5.82 keV. The error appears to originate mainly from noise and digitization effect for the energy.

Science Data Packet	Event Type	Detector ID	ASIC ID	Channel ID	Time Tagging (Second Value)	Time Tagging (Microsecond Value)	Reject Event	Energy Channel 1	Energy Channel 2
	3'b010	3'b000	5'b00111	3'b101	0x000A	0x001A9	0x00	9'b000010100	9'b001001101
Explanation	2-Channel Event	Event Location: Anode 61 and Anode 62 of the first Detector Half			Event Time Tagging:10.000425 s		0	20*60 eV=1.2 keV	77*60 eV=4.62 keV
								5.82 keV	

Figure 5.16: The science data packet in the simulation with an incident X-ray photon generated by ^{55}Fe (^{55}Mn).

The science data packet will be sent to the science data FIFO automatically, the PBEE side (now the PC through the FTDI circuit) then sends a telecommand to the MBEE, and the MBEE will transmit the packet to the PBEE (now the PC).

In this chapter, we have introduced in detail the establishment of the interfaces in the MBEE, which were established using some simulators. The system built based on these simulators was jointly tested to verify the MBEE's control functions, especially power control, and the ability to obtain X-ray event time and energy information in a detector half.

Chapter 6

Summary and Outlook

6.1 Summary

The complete process of the MBEE development has been described. As a new generation of X-ray observatory, the eXTP mission, or a similar mission like the STROBE-X mission, aims to detect X-rays generated in extreme environments of the universe and study the state and change mechanism of matter under extreme conditions. Among the multiple payloads of the eXTP mission, the LAD is responsible for time-varying energy spectrum measurements of X-rays in the range from 2 keV to 30 keV. Its outstanding features are a large effective detection area and good energy and time resolution capabilities. The good performance of the LAD relies on the application of a large number of large area multi-channel SDDs. Such a large number of detectors and signal read-out channels requires high performance and integration for the LAD's readout electronics. To meet this demand, LAD adopts the ASIC-based FEEs, combined with a modular design concept and a hierarchical digital circuit to improve the stability, flexibility, and scalability of the system.

In the electronics system of the LAD, the MBEE is its core control unit, responsible for managing the data processing flow of the LAD, and is also a key part of extracting X-ray event time information and energy information from digitized signals. The design and implementation process of the MBEE are presented, including the functions of the MBEE in the LAD system, hardware architecture, and design challenges and solutions. In addition, in view of the core role of the FPGA part in the MBEE system, we also introduce its program architecture, functions, and design ideas in detail, focusing on the analysis of the MBEE's FPGA algorithm for reconstructing the time and energy of X-ray events: a data processing method based on a pipeline concept.

In order to verify the design performance of the MBEE and its applicability in the LAD system, an MPSU simulator and an FEE simulator were built to simulate the interface interaction and data processing capabilities of the MBEE in an actual working scenario. Through the complete system joint test, the core functions of the MBEE in the LAD electronics system, especially in voltage control, data transmission, and X-ray event time and energy reconstruction, were verified.

6.2 Outlook

After completing the simulation of one detector half and its data processing pipeline, the next natural step is to extend the simulation to a complete detector, including two independent data processing pipelines. Further, the simulation can be extended to 8 detectors and their data processing pipelines running on the MBEE. This extension poses new challenges to various parts of the system: firstly, for the GUI and its internal software, it is necessary to be able to quickly generate continuous events; however, the speed of transmitting these events to the FEE simulator through the serial port such as UART interface is too slow, which can easily lead to loss of synchronicity. Secondly, as the number of detectors increases, the number of required FEE simulators will also increase.

Therefore, a more feasible solution is to focus on simulating a complete large area multi-channel SDD and its two independent data processing pipelines, and on this basis, add more realistic detection response simulations and consider the noise model of the electronic system. At the same time, the data transmission time from the GUI to the FEE simulator must be minimized. To deal with this problem, high-speed Gigabit networks can be considered for transmitting data. Such a relatively complete system will be manufactured that can reflect the physical process of the detector, the noise level of the circuit, and the interfaces between the MBEE with each part of the module's electronics, which will be beneficial for us to take the next step in development. In addition, in order to further test the system performance extensively, the MBEE and its FEE-MBEE interface, an actual FEE board is necessary for the joint test of the LAD module's electronics.

Acknowledgments

I would like to express my sincere gratitude to the Institut für Astronomie und Astrophysik Tübingen (IAAT) and every colleague who has supported me in my research, studies, and daily life. Working with you and growing together has been an incredibly rewarding experience. I would especially like to express my deepest appreciation to:

Prof. Dott. Andrea Santangelo: Words cannot fully express my gratitude. During moments of doubt and confusion, you always give me strength and endless support. Professor, thank you for choosing me to participate in such a meaningful project-the eXTP mission and for supporting me and leading me into the fascinating world of astronomical research.

Dr. Jörg Bayer: Thank you for your invaluable guidance in my research—whether in circuit design, FPGA program architecture, system design, or joint testing, your insights have been instrumental. No matter how many questions I had, you were always patient and willing to help. It is worth mentioning that the design of the MPSU simulator were completed by Dr. Jörg Bayer.

Dr. Chris Tenzer: Thank you for your help in research, especially your guidance in detection physics. Your coordination within the hardware team has been important in fostering effective collaboration, which enables us to work closely together and complete the task together.

IAAT Hardware Team: I would like to express my sincere gratitude to every colleague in the hardware team of the institute. Thank you for your support in my work.

Sabine Lauer: Thank you for your support in both work and daily life. As the institute's secretary, your dedication and responsibility have greatly contributed to a smoother research environment.

To my friends in Germany, thank you for the wonderful time we shared in both study and

play. You have made this journey more colorful and beautiful.

I would like to thank my family. Your unwavering support has given and will always give me the courage and strength to keep moving forward.
Thank you—for being there, for your companionship, and for giving me endless courage. To me, that means everything.

Abbreviations

eXTP	enhanced X-ray Timing and Polarimetry
XTP	X-ray Timing and Polarimetry
LOFT	Large Observatory for X-ray Timing
IHEP	Institute of High Energy Physics
CAS	Chinese Academy of Science
LAD	Large Area Detector
SDD	Silicon Drift Detector
FEE	Front-End Electronics
MBEE	Module Back-End Electronics
VHDL	Very High-Speed Integrated Circuit Hardware Description Language
FPGA	Field-Programmable Gate Array
GUI	Graphical User Interface
MPSU	Module Power Supply Unit
SFA	Spectroscopic Focusing Array
PFA	Polarimetry Focusing Array
WFM	Wide Field Monitor
STROBE-X	Spectroscopic Time-Resolving Observatory for Broadband Energy X-rays
PBEE	Panel Back-End Electronics
ICU	Instrument Control Unit
UV	Ultraviolet
HM-NSXRB	High-Mass Neutron Star X-ray Binary
LM-BHXRB	Low-Mass Black Hole X-ray Binary
QPO	Quasi-Periodic Oscillation
FWHM	Full Width at Half Maximum
FoV	Field of View
SNR	Signal-to-Noise Ratio
GRB	Gamma-Ray Bursts
PSD	Power Spectral Density
HEW	Half Energy Width

PSF	Point Spread Function
HPD	Half Power Diameter
SiPM	Silicon photomultiplier
PMT	photomultiplier tube
PD	photodiode
GPD	Gas Pixel Detector
GEM	Gas Electron Multiplier
EOS	Equation of State
LMXB	Low-Mass X-ray Binary
ISCO	Innermost Stable Circular Orbit
AGN	Active Galactic Nucleus
XRB	X-ray Binary
AXP	Anomalous X-ray Pulsar
SGR	Soft Gamma-Ray Repeater
QED	Quantum Electrodynamics
RXTE	Rossi X-ray Timing Explorer
Chandra	Chandra X-ray Observatory
XMM-Newton	X-ray Multi-Mirror Mission
eROSITA	Extended Roentgen Survey with an Imaging Telescope Array
HXMT	Hard X-ray Modulation Telescope
NICER	Neutron star Interior Composition Explorer
SEXTANT	Station Explorer for X-ray Timing and Navigation Technology
ISS	International Space Station
IAAT	Institut für Astronomie und Astrophysik
XRCA	X-ray Concentrator Array
XRC	X-ray Concentrator
I/O	Input/Output
ASIC	Application Specific Integrated Circuit
ADC	Analog-to-Digital Converter
CEA	French Alternative Energies and Atomic Energy Commission
DLL	Delay-locked loop
PLL	Phase-locked loop
LVDS	Low-Voltage Differential Signaling
CMOS	Complementary Metal-Oxide-Semiconductor
HK	housekeeping
ITAR	International Traffic in Arms Regulations
LVCMOS	Low-Voltage Complementary Metal-Oxide-Semiconductor

SPI	Serial Peripheral Interface
TMR	Triple Modular Redundancy
HV	High Voltage
MV	Medium Voltage
LV	Low Voltage
MCU	Microcontroller Unit
UART	Universal Asynchronous Receiver Transmitter
PPS	Pulse Per Second
GNSS	Global Navigation Satellite System
GPS	Global Positioning System
EMI	Electromagnetic Interference
PCB	Printed Circuit Board
FIFO	First In First Out
A/D	Analog/Digital
RAM	Random Access Memory
OETS algorithm	Odd-Even-Transportation-Sort algorithm

List of Figures

List of Tables

Bibliography

3DFS128M01VS2728 (N.D). An embedded TMR 128 Mbit SPI NOR Flash. https://www.3d-plus.com/products/space-radiation-tolerant-spi-nor-flash/.

Akhiezer, A. I. and Berestetskii, V. B. (1953). *Quantum Electrodynamics*. US Atomic Energy Commission, Technical Information Service Extension.

Amptek (N.D). FAST SDD Ultra High Performance Silicon Drift Detector. https://www.amptek.com/products/x-ray-detectors/fastsdd-x-ray-detectors-for-xrf-eds/fastsdd-silicon-drift-detector.

Arnaud, K., Smith, R., and Siemiginowska, A. (2011). *Handbook of X-ray Astronomy*, volume 7. Cambridge University Press.

Arzoumanian, Z., Gendreau, K., Baker, C., Cazeau, T., Hestnes, P., Kellogg, J., Kenyon, S., Kozon, R., Liu, K.-C., Manthripragada, S., *et al.* (2014). The neutron star interior composition explorer (NICER): mission definition. In *Space telescopes and instrumentation 2014: Ultraviolet to gamma ray*, volume 9144, pages 579–587. SPIE.

Baudin, D., Altenmüller, K., Bausson, P., Coppolani, X., Gevin, O., Limousin, O., Maier, D., Meuris, A., and Passeron, C. (2018). IDeF-X HDBD: low-noise ASIC for Spectro-imaging with semiconductor detectors. In *2018 IEEE Nuclear Science Symposium and Medical Imaging Conference Proceedings (NSS/MIC)*, pages 1–2. IEEE.

Baudin, D., Limousin, O., Gevin, O., Meuris, A., Altenmüller, K., Bausson, P., Ceraudo, F., Coppolani, X., Maier, D., Passeron, C., *et al.* (2022). IDeF-X HDBD: low-noise ASIC for imaging spectroscopy with semiconductor detectors in space science applications. *IEEE Transactions on Nuclear Science*, **69**(3), 620–626.

Becker, P., Klochkov, D., Schönherr, G., Nishimura, O., Ferrigno, C., Caballero, I., Kretschmar, P., Wolff, M., Wilms, J., and Staubert, R. (2012). Spectral formation in accreting X-ray pulsars: bimodal variation of the cyclotron energy with luminosity. *Astronomy & Astrophysics*, **544**, A123.

Bellazzini, R., Spandre, G., Minuti, M., Baldini, L., Brez, A., Cavalca, F., Latronico, L., Omodei, N., Massai, M., Sgro, C., *et al.* (2006). Direct reading of charge multipliers with a self-triggering CMOS analog chip with 105 k pixels at 50 μm pitch. *Nuclear Instruments and Methods in Physics Research Section A: Accelerators, Spectrometers, Detectors and Associated Equipment*, **566**(2), 552–562.

Bellazzini, R., Spandre, G., Minuti, M., Baldini, L., Brez, A., Latronico, L., Omodei, N., Razzano, M., Massai, M., Pesce-Rollins, M., *et al.* (2007). A sealed Gas Pixel Detector for X-ray astronomy. *Nuclear Instruments and Methods in Physics Research Section A: Accelerators, Spectrometers, Detectors and Associated Equipment*, **579**(2), 853–858.

Belloni, T. M. and Motta, S. E. (2016). Transient black hole binaries. *Astrophysics of Black Holes: From Fundamental Aspects to Latest Developments*, pages 61–97.

Bhattacharyya, S. (2011). Ways to constrain neutron star equation of state models using relativistic disc lines. *Monthly Notices of the Royal Astronomical Society*, **415**(4), 3247–3252.

Bogatin, E. (2004). *Signal integrity: simplified*. Prentice Hall Professional.

Bouyjou, F., Gevin, O., Limousin, O., and Delagnes, E. (2017). A 32-channel 13-b ADC for space applications. *IEEE Transactions on Nuclear Science*, **64**(4), 1071–1079.

Bradt, H., Levine, A., Morgan, E., Remillard, R., Swank, J., Dingus, B., Holt, S., Jahoda, K., Rothschild, R., Gruber, D., *et al.* (1990). The X-ray timing explorer. In *International Astronomical Union Colloquium*, volume 123, pages 89–110. Cambridge University Press.

Brussaard, P. and Van de Hulst, H. (1962). Approximation formulas for nonrelativistic bremsstrahlung and average Gaunt factors for a Maxwellian electron gas. *Reviews of Modern Physics*, **34**(3), 507.

Caballero, I. and Wilms, J. (2012). X-ray pulsars: a review. *arXiv preprint arXiv:1206.3124*.

Campana, R., Zampa, G., Feroci, M., Vacchi, A., Bonvicini, V., Del Monte, E., Evangelista, Y., Fuschino, F., Labanti, C., Marisaldi, M., *et al.* (2011). Imaging performance of a large-area Silicon Drift Detector for X-ray astronomy. *Nucl. Instr. and Meth. A*, **633**(1), 22–30.

Cardall, C. Y., Prakash, M., and Lattimer, J. M. (2001). Effects of strong magnetic fields on neutron star structure. *The Astrophysical Journal*, **554**(1), 322.

Ceraudo, F., Della Casa, G., Bertuccio, G., Bonvicini, W., Campana, R., Cirrincione, D., Del Monte, E., Evangelista, Y., Feroci, M., Ficorella, F., *et al.* (2024a). Imaging and spectroscopic performances of the silicon drift detector of the wide field monitor. In *Space Telescopes and Instrumentation 2024: Ultraviolet to Gamma Ray*, volume 13093, pages 1918–1926. SPIE.

Ceraudo, F., Nuti, A., Bertuccio, G., Campana, R., Cirrincione, D., Della Casa, G., Del Monte, E., Dilillo, G., Evangelista, Y., Feroci, M., *et al.* (2024b). The Detector Assembly of the cameras of the Lunar Electromagnetic Monitor in X-rays (LEM-X). In *Space Telescopes and Instrumentation 2024: Ultraviolet to Gamma Ray*, volume 13093, pages 2070–2079. SPIE.

Costa, E., Soffitta, P., Bellazzini, R., Brez, A., Lumb, N., and Spandre, G. (2001). An efficient photoelectric X-ray polarimeter for the study of black holes and neutron stars. *Nature*, **411**(6838), 662–665.

Crescio, E. and Nouais, D. (2006). Electron cloud size measurement in silicon drift detectors and spatial resolution improvement. *Nuclear Instruments and Methods in Physics Research Section A: Accelerators, Spectrometers, Detectors and Associated Equipment*, **564**(1), 475–481.

DevKit (N.D). The Development Kit is a demonstration board for NG-MEDIUM CLGA625 chip. https://nanoxplore-wiki.atlassian.net/wiki/spaces/NAN/pages/34537502/DevKits+NG-MEDIUM.

Done, C., Gierliński, M., and Kubota, A. (2007). Modelling the behaviour of accretion flows in X-ray binaries: Everything you always wanted to know about accretion but were afraid to ask. *The Astronomy and Astrophysics Review*, **15**, 1–66.

Ertugrul, M., Şimşek, Ö., Dogan, O., Öz, E., Sögüt, Ö., and Turgut, Ü. (2001). Measurement of the Kα and Kβ X-rays polarization degree and polarization effect on the Kβ/Kα intensity ratio. *Nuclear Instruments and Methods in Physics Research Section B: Beam Interactions with Materials and Atoms*, **179**(4), 465–468.

eXTP Collaboration (2024). eXTP. https://ihep.cas.cn/dkxzz/HEPS/kxpj/kpwz/202401/t20240101_6932655.html.

eXTP Collaboration (N.D). eXTP. https://www.ice.csic.es/research/missions-experiments?view=article&id=72&catid=2.

Fabian, A., Iwasawa, K., Reynolds, C., and Young, A. (2000). Broad iron lines in active galactic nuclei. *Publications of the Astronomical Society of the Pacific*, **112**(775), 1145.

Fano, U. (1947). Ionization yield of radiations. II. The fluctuations of the number of ions. *Physical Review*, **72**(1), 26.

Feroci, M., Stella, L., Van der Klis, M., Courvoisier, T. L., Hernanz, M., Hudec, R., Santangelo, A., Walton, D., Zdziarski, A., Barret, D., *et al.* (2012). The large observatory for X-ray timing (LOFT). *Experimental Astronomy*, **34**, 415–444.

Feroci, M., Bozzo, E., Brandt, S., Hernanz, M., Van Der Klis, M., Liu, L.-P., Orleanski, P., Pohl, M., Santangelo, A., Schanne, S., *et al.* (2016). The LOFT mission concept: a status update. In *Space Telescopes and Instrumentation 2016: Ultraviolet to Gamma Ray*, volume 9905, pages 505–524. SPIE.

Feroci, M., Ahangarianabhari, M., Ambrosi, G., Ambrosino, F., Argan, A., Barbera, M., Bayer, J., Bellutti, P., Bertucci, B., Bertuccio, G., *et al.* (2018). The large area detector onboard the eXTP mission. In *Space Telescopes and Instrumentation 2018: Ultraviolet to Gamma Ray*, volume 10699, pages 281–295. SPIE.

Fischer, P. (2011). Exploring nanoscale magnetism in advanced materials with polarized X-rays. *Materials Science and Engineering: R: Reports*, **72**(5), 81–95.

Fortov, V. E. and Fortov, V. E. (2016). High Energy Densities in Planets and Stars. *Extreme States of Matter: High Energy Density Physics*, pages 505–590.

FT232H (N.D). Single Channel HiSpeed USB to Multipurpose UART/FIFO IC. https://ftdichip.com/wp-content/uploads/2020/07/DS_FT232H.pdf.

Gale, M. T., Gimkiewicz, C., Obi, S., Schnieper, M., Söchtig, J., Thiele, H., and Westenhöfer, S. (2005). Replication technology for optical microsystems. *Optics and Lasers in Engineering*, **43**(3-5), 373–386.

Gendreau, K. C., Arzoumanian, Z., and Okajima, T. (2012). The Neutron star Interior Composition ExploreR (NICER): an Explorer mission of opportunity for soft X-ray timing spectroscopy. In *Space telescopes and instrumentation 2012: ultraviolet to gamma ray*, volume 8443, pages 322–329. SPIE.

Geuther, J. A. and Danon, Y. (2005). Electron and positive ion acceleration with pyroelectric crystals. *Journal of applied physics*, **97**(7).

Gevin, O., Lemaire, O., Lugiez, F., Michalowska, A., Baron, P., Limousin, O., and Delagnes, E. (2012). Imaging X-ray detector front-end with high dynamic range: IDeF-X HD. *Nuclear Instruments and Methods in Physics Research Section A: Accelerators, Spectrometers, Detectors and Associated Equipment*, **695**, 415–419.

Hattori, K. and Itakura, K. (2013). Vacuum birefringence in strong magnetic fields:(I) Photon polarization tensor with all the Landau levels. *Annals of Physics*, **330**, 23–54.

Hernanz, M., Brandt, S., Feroci, M., Orleansky, P., Santangelo, A., Schanne, S., Wu, X., Zhang, S., Xu, Y., Bozzo, E., *et al.* (2018). The wide field monitor onboard the eXTP mission. In *Space Telescopes and Instrumentation 2018: Ultraviolet to Gamma Ray*, volume 10699, pages 1044–1059. SPIE.

Hill, J., Black, J., Deines-Jones, P., Jahoda, K., Bellazzini, R., Brez, A., Costa, E., Kaaret, P., Minuti, M., Spandre, G., *et al.* (2006). X-ray Polarisation Measurements with a Micro-pattern Gas Polarimeter. In *American Astronomical Society Meeting Abstracts# 207*, volume 207, pages 211–03.

Hutcheson, A. L., Feroci, M., Argan, A., Antonelli, M., Barbera, M., Bayer, J., Bellutti, P., Bertuccio, G., Bonvicini, V., Cadoux, F., *et al.* (2024). Spectroscopic Time-Resolving Observatory for Broadband Energy X-ray high-energy modular array. *Journal of Astronomical Telescopes, Instruments, and Systems*, **10**(4), 042503–042503.

Inductiveload and NASA (2007). Electromagnetic Spectrum Diagram. https://commons.wikimedia.org/wiki/File:EM_Spectrum_Properties_ca.svg.

Ingram, A. R. and Motta, S. E. (2019). A review of quasi-periodic oscillations from black hole X-ray binaries: observation and theory. *New Astronomy Reviews*, **85**, 101524.

in't Zand, J. J., Bozzo, E., Qu, J., Li, X.-D., Amati, L., Chen, Y., Donnarumma, I., Doroshenko, V., Drake, S. A., Hernanz, M., *et al.* (2019). Observatory science with eXTP. *Science China Physics, Mechanics & Astronomy*, **62**, 1–42.

Jansen, F., Lumb, D., Altieri, B., Clavel, J., Ehle, M., Erd, C., Gabriel, C., Guainazzi, M., Gondoin, P., Much, R., *et al.* (2001). XMM-Newton observatory. I. The spacecraft and operations. *Astronomy & Astrophysics*, **365**, L1–L6.

Jeremy Sanders and Hermann Brunner and the eSASS team (MPE) and Eugene Churazov and Marat Gilfanov (on behalf of IKI) (2020). Image of the X-ray binary system. Max Planck Institute for Extraterrestrial Physics (MPE).

Joensen, K. D., Christensen, F. E., Schnopper, H. W., Gorenstein, P., Susini, J., Hoghoj, P., Hustache, R., Wood, J. L., and Parker, K. (1993). Medium-sized grazing incidence high-energy x-ray telescopes employing continuously graded multilayers. In *X-Ray Detector Physics and Applications*, volume 1736, pages 239–248. SPIE.

Jovanović, P. (2012). The broad Fe Kα line and supermassive black holes. *New Astronomy Reviews*, **56**(2-3), 37–48.

Kaaret, P. (2021). X-ray polarimetry. In *The WSPC Handbook of Astronomical Instrumentation: Volume 4: X-Ray Astronomical Instrumentation*, pages 281–300. World Scientific.

Knoll, G. F. (2010). *Radiation detection and measurement*. John Wiley & Sons.

Kule, D. (2010). Black-body Radiation Spectrum.

Lalit, S., Mamun, M., Constantinou, C., and Prakash, M. (2019). Dense matter equation of state for neutron star mergers. *The European Physical Journal A*, **55**(1), 10.

Lasota, J.-P. (2001). The disc instability model of dwarf novae and low-mass X-ray binary transients. *New Astronomy Reviews*, **45**(7), 449–508.

Lattimer, J. M. (2015). Introduction to neutron stars. In *AIP Conference Proceedings*, volume 1645, pages 61–78. American Institute of Physics.

Lechner, P., Fiorini, C., Hartmann, R., Kemmer, J., Krause, N., Leutenegger, P., Longoni, A., Soltau, H., Stötter, D., Stötter, R., *et al.* (2001). Silicon drift detectors for high count rate X-ray spectroscopy at room temperature. *Nucl. Instr. and Meth. A*, **458**(1-2), 281–287.

Leighton, F. T. (1991). *Introduction to Parallel Algorithms and Architectures: Arrays, Trees, Hypercubes*. Morgan Kaufmann Pub., 1st edition.

Li, H., Feng, H., Muleri, F., Bellazzini, R., Minuti, M., Soffitta, P., Brez, A., Spandre, G., Pinchera, M., Sgró, C., *et al.* (2015). Assembly and test of the gas pixel detector for X-ray polarimetry. *Nuclear Instruments and Methods in Physics Research Section A: Accelerators, Spectrometers, Detectors and Associated Equipment*, **804**, 155–162.

LMZ10504TZ-ADJ/NOPB (N.D.). 5.5V, 4A Power Module in Leaded Surface Mount TO Package. https://www.ti.com/product/LMZ10504/part-details/LMZ10504TZ-ADJ/NOPB.

Longair, M. S. (2011). *High energy astrophysics*. Cambridge University Press.

Lyons, R. E. and Vanderkulk, W. (1962). The use of triple-modular redundancy to improve computer reliability. *IBM journal of research and development*, **6**(2), 200–209.

Lyutikov, M. (2003). Explosive reconnection in magnetars. *Monthly Notices of the Royal Astronomical Society*, **346**(2), 540–554.

Mereghetti, S. (2008). The strongest cosmic magnets: soft gamma-ray repeaters and anomalous X-ray pulsars. *The Astronomy and Astrophysics Review*, **15**(4), 225–287.

Mereghetti, S., Pons, J. A., and Melatos, A. (2015). Magnetars: properties, origin and evolution. *Space Science Reviews*, **191**, 315–338.

Meszaros, P. (2006). Gamma-ray bursts. *Reports on Progress in Physics*, **69**(8), 2259.

Miller, M. C. and Miller, J. M. (2015). The masses and spins of neutron stars and stellar-mass black holes. *Physics Reports*, **548**, 1–34.

Minervini, G., Argan, A., Feroci, M., Trois, A., Del Monte, E., Brienza, D., Ambrosi, G., Antonelli, M., Barbera, M., Baudin, D., *et al.* (2024). Managing the mass production for the LAD instrument onboard eXTP. In *Modeling, Systems Engineering, and Project Management for Astronomy XI*, volume 13099, pages 466–480. SPIE.

Mobilio, S., Boscherini, F., Meneghini, C., *et al.* (2016). *Synchrotron Radiation*. Springer.

Molin, A., Clerc, N., Pointecouteau, E., Pajot, F., and Cucchetti, E. (2023). Observing gravitational redshift with X-ray emission in galaxy clusters with Athena X-IFU. *Astronomy & Astrophysics*, **679**, A24.

Moses, W. W. (2002). Current trends in scintillator detectors and materials. *Nuclear Instruments and Methods in Physics Research Section A: Accelerators, Spectrometers, Detectors and Associated Equipment*, **487**(1-2), 123–128.

Nelson, R. W., Salpeter, E., and Wasserman, I. (1993). Nonthermal cyclotron emission from low-luminosity accretion onto magnetic neutron stars. *Astrophysical Journal v. 418, p. 874*, **418**, 874.

NX1H35ASN (N.D). The first Radiation Hardened By Design (RHBD) SRAM-based FPGA developed by NanoXplore. https://nanoxplore-wiki.atlassian.net/wiki/spaces/NAN/pages/11075592/NG-MEDIUM.

O'Dell, S. L., Attinà, P., Baldini, L., Barbanera, M., Baumgartner, W. H., Bellazzini, R., Bladt, J., Bongiorno, S. D., Brez, A., Cavazzuti, E., *et al.* (2019). The imaging x-ray polarimetry explorer (IXPE): technical overview II. *UV, X-Ray, and Gamma-Ray Space Instrumentation for Astronomy XXI*, **11118**, 248–261.

Ott, C. D., Burrows, A., Thompson, T. A., Livne, E., and Walder, R. (2006). The spin periods and rotational profiles of neutron stars at birth. *The Astrophysical Journal Supplement Series*, **164**(1), 130.

Paul, B. (2017). Neutron Stars in X-ray Binaries and their Environments. *Journal of Astrophysics and Astronomy*, **38**, 1–12.

Poisson, E., Pound, A., and Vega, I. (2011). The motion of point particles in curved spacetime. *Living Reviews in Relativity*, **14**, 1–190.

Poutanen, J. (2006). Accretion-powered millisecond pulsars. *Advances in Space Research*, **38**(12), 2697–2703.

Predehl, P., Andritschke, R., Bornemann, W., Bräuninger, H., Briel, U., Brunner, H., Burkert, W., Dennerl, K., Eder, J., Freyberg, M., *et al.* (2007). eROSITA. In *UV, X-Ray, and Gamma-Ray Space Instrumentation for Astronomy XV*, volume 6686, pages 354–362. SPIE.

Rad, A. M., Azari, L. V., *et al.* (2014). Determining attitude and position in deep space missions using X-ray pulsars. *International Journal of Astronomy and Astrophysics*, **4**(04), 628.

Ray, P. S. *et al.* (2019). STROBE-X: X-ray Timing and Spectroscopy on Dynamical Timescales from Microseconds to Years: A Probe Class Mission Concept APC White Paper Submitted to Astro 2020 Decadal Survey. *American Astronomical Society. Bulletin (Online)*, **51**(7).

Ray, P. S., Arzoumanian, Z., Brandt, S., Burns, E., Chakrabarty, D., Feroci, M., Gendreau, K. C., Gevin, O., Hernanz, M., Jenke, P., *et al.* (2018). STROBE-X: a probe-class mission for X-ray spectroscopy and timing on timescales from microseconds to years. In *Space Telescopes and Instrumentation 2018: Ultraviolet to Gamma Ray*, volume 10699, pages 249–268. SPIE.

Ray, P. S., Roming, P. W., Argan, A., Arzoumanian, Z., Ballantyne, D. R., Bogdanov, S., Bonvicini, V., Brandt, T. J., Bursa, M., Cackett, E. M., *et al.* (2024). STROBE-X mission overview. *arXiv preprint arXiv:2410.08342*.

RHFAD128 (N.D). Rad-Hard 8-channel 12-bit A/D converter. https://www.st.com/en/space-products/rhfad128.html.

RHFLVDS31A (N.D). Rad-Hard quad LVDS driver. https://www.st.com/en/space-products/rhflvds31a.html.

RHFLVDS32A (N.D). Rad-Hard quad LVDS receiver. https://www.st.com/en/space-products/rhflvds32a.html.

Romani, R. W. (1990). A unified model of neutron-star magnetic fields. *Nature*, **347**(6295), 741–743.

Rosa, A. D., Uttley, P., Gou, L., Liu, Y., Bambi, C., Barret, D., Belloni, T., Berti, E., Bianchi, S., Caiazzo, I., *et al.* (2019). Accretion in strong field gravity with eXTP. *SCIENCE CHINA Physics, Mechanics & Astronomy*, **62**, 1–29.

Ruderman, M. (1972). Pulsars: structure and dynamics. *Annual Review of Astronomy and Astrophysics, vol. 10, p. 427*, **10**, 427.

Rybicki, G. B. and Lightman, A. P. (2024). *Radiative processes in astrophysics*. John Wiley & Sons.

Santangelo, A., Zane, S., Feng, H., Xu, R., Doroshenko, V., Bozzo, E., Caiazzo, I., Zelati, F. C., Esposito, P., González-Caniulef, D., *et al.* (2019). Physics and astrophysics of strong magnetic field systems with eXTP. *SCIENCE CHINA Physics, Mechanics & Astronomy*, **62**, 1–23.

Santangelo, A., Zhang, S.-N., Feroci, M., Hernanz, M., Lu, F., and Xu, Y. (2022). The Enhanced X-ray Timing and Polarimetry Mission: eXTP. In *Handbook of X-ray and Gamma-ray Astrophysics*, pages 1–29. Springer.

Sarazin, C. L. (1986). X-ray emission from clusters of galaxies. *Reviews of Modern Physics*, **58**(1), 1.

Sauli, F. (1998). Gas detectors: Recent developments and future perspectives. *Nuclear Instruments and Methods in Physics Research Section A: Accelerators, Spectrometers, Detectors and Associated Equipment*, **419**(2-3), 189–201.

Schumann, R. W. and McMahon, J. P. (1956). Argonne 256-Channel Pulse-Height Analyzer. *Review of Scientific Instruments*, **27**(9), 675–685.

Schwarm, F.-W., Schönherr, G., Falkner, S., Pottschmidt, K., Wolff, M., Becker, P., Sokolova-Lapa, E., Klochkov, D., Ferrigno, C., Fürst, F., *et al.* (2017). Cyclotron resonant scattering feature simulations-i. Thermally averaged cyclotron scattering cross sections, mean free photon-path tables, and electron momentum sampling. *Astronomy & Astrophysics*, **597**, A3.

Seward, F. D. and Charles, P. A. (2010). *Exploring the X-ray Universe*. Cambridge University Press.

Shakura, N. I. and Sunyaev, R. A. (1973). Black holes in binary systems. Observational appearance. *Astronomy and Astrophysics, Vol. 24, p. 337-355*, **24**, 337–355.

Spieler, H. (2005). *Semiconductor detector systems*, volume 12. Oxford university press.

Staubert, R., Trümper, J., Kendziorra, E., Klochkov, D., Postnov, K., Kretschmar, P., Pottschmidt, K., Haberl, F., Rothschild, R., Santangelo, A., *et al.* (2019). Cyclotron lines in highly magnetized neutron stars. *Astronomy & Astrophysics*, **622**, A61.

Steiner, A. W., Lattimer, J. M., and Brown, E. F. (2013). The neutron star mass–radius relation and the equation of state of dense matter. *The Astrophysical Journal Letters*, **765**(1), L5.

Strüder, L., Lechner, P., and Leutenegger, P. (1998). Silicon drift detector–the key to new experiments. *The Science of Nature*, **85**(11), 539–543.

Tanaka, Y., Nandra, K., Fabian, A., Inoue, H., Otani, C., Dotani, T., Hayashida, K., Iwasawa, K., Kii, T., Kunieda, H., *et al.* (1995). Gravitationally redshifted emission implying an accretion disk and massive black hole in the active galaxy MCG–6–30–15. *Nature*, **375**(6533), 659–661.

Tauris, T. and Manchester, R. (1998). On the evolution of pulsar beams. *Monthly Notices of the Royal Astronomical Society*, **298**(3), 625–636.

Ternov, I. M. (1995). Synchrotron radiation. *Physics-Uspekhi*, **38**(4), 409.

Thorsett, S. (1996). The Gravitational constant, the Chandrasekhar limit, and neutron star masses. *Physical Review Letters*, **77**(8), 1432.

Trümper, J., Pietsch, W., Reppin, C., Voges, W., Staubert, R., and Kendziorra, E. (1978). Evidence for strong cyclotron line emission in the hard X-ray spectrum of Hercules X-1. *Astrophysical Journal, Part 2-Letters to the Editor, vol. 219, Feb. 1, 1978, p. L105-L110. Deutsche Forschungsgemeinschaft*, **219**, L105–L110.

Tucker, W. (1975). Radiation processes in astrophysics. *The Harvard Books on Astronomy*.

Van der Klis, M. (2006). *Compact stellar X-ray sources*. Cambridge University Press.

Vortex (N.D). Vortex silicon drift X-ray detector. https://www.hitachi-hightech.com/us/en/products/analytical-systems/sdd/vortex.html?utm_source=chatgpt.com.

Wang, D., Gao, Y., Chen, W., Zhang, J., and Wang, S. (2021). Equivalent analysis of thermo-dynamic blow-off impulse under X-ray irradiation. *Applied Sciences*, **11**(19), 8853.

Watts, A., Xu, R., Espinoza, C., Andersson, N., Antoniadis, J., Antonopoulou, D., Buchner, S., Dai, S., Demorest, P., Freire, P., *et al.* (2014). Probing the neutron star interior and the Equation of State of cold dense matter with the SKA. *arXiv preprint arXiv:1501.00042*.

Watts, A. L., Yu, W., Poutanen, J., Zhang, S., Bhattacharyya, S., Bogdanov, S., Ji, L., Patruno, A., Riley, T. E., Bakala, P., *et al.* (2019). Dense matter with eXTP. *Science China Physics, Mechanics & Astronomy*, **62**, 1–17.

Weisskopf, M. C., Tananbaum, H. D., Van Speybroeck, L. P., and O'Dell, S. L. (2000). An Overview of the Performance and Scientific Results from the Chandra X-Ray Observatory. *Proceedings of the SPIE*, **4012**, 2–16.

Wilkinson, D. (1950). A stable ninety-nine channel pulse amplitude analyser for slow counting. In *Mathematical Proceedings of the Cambridge Philosophical Society*, volume 46, pages 508–518. Cambridge University Press.

Wilson, A. and Yang, Y. (2002). Chandra X-ray imaging and spectroscopy of the M87 jet and nucleus. *The Astrophysical Journal*, **568**(1), 133.

Xiong, H., Zhou, R., Chen, J., Li, Y., Yang, C., Bi, B., Zhang, J., Zhang, J., Cao, X., Zhang, S., *et al.* (2019). Design and performance of analog circuit for the wide field of view Cherenkov telescope array of LHAASO. *Nuclear Instruments and Methods in Physics Research Section A: Accelerators, Spectrometers, Detectors and Associated Equipment*, **925**, 156–163.

Xiong, H., Argan, A., Baudin, D., Bayer, J., Bouyjou, F., De Angelis, N., Del Monte, E., Evangelista, Y., Favre, Y., Feroci, M., *et al.* (2022). The digital data processing concepts of the large area detector and the wide field monitor onboard eXTP. In *Space Telescopes and Instrumentation 2022: Ultraviolet to Gamma Ray*, volume 12181, pages 1631–1639. SPIE.

Xiong, H., Bayer, J., Santangelo, A., Feroci, M., Del Monte, E., Guzman, A., Hedderman, P., Minervini, G., Pliego, S., Putz, A., *et al.* (2025). Preliminary design and development of the module back-end electronics for the large area detector onboard the eXTP . *Experimental Astronomy*, **59**(1), 1.

Youngworth, R. N., Gallagher, B. B., and Stamper, B. L. (2005). An overview of power spectral density (PSD) calculations. *Optical manufacturing and testing VI*, **5869**, 206–216.

Yu, W. and van der Klis, M. (2002). Kilohertz quasi-periodic oscillation frequency anticorrelated with millihertz quasi-periodic oscillation flux in 4U 1608–52. *The Astrophysical Journal*, **567**(1), L67.

ZA1-Micro-Array-Series (N.D). 1.00 mm Ultra-Low Profile Compression Interposer. https://www.samtec.com/products/za1-et-d.

Zane, S., Walton, D., Kennedy, T., Feroci, M., Den Herder, J.-W., Ahangarianabhari, M., Argan, A., Azzarello, P., Baldazzi, G., Barret, D., *et al.* (2012). A large area detector proposed for the Large Observatory for X-ray Timing (LOFT). In *Space Telescopes and Instrumentation 2012: Ultraviolet to Gamma Ray*, volume 8443, pages 706–720. SPIE.

Zhang, S., Feroci, M., Santangelo, A., Dong, Y., Feng, H., Lu, F., Nandra, K., Wang, Z., Zhang, S., Bozzo, E., *et al.* (2017). eXTP: Enhanced X-ray Timing and Polarization mission. In *Space telescopes and instrumentation 2016: ultraviolet to gamma ray*, volume 9905, pages 505–520. SPIE.

Zhang, S., Zhang, S., Lu, F., Li, T., Song, L., Xu, Y., Wang, H., Qu, J., Liu, C., Chen, Y., *et al.* (2018). The insight-HXMT mission and its recent progresses. In *Space Telescopes and Instrumentation 2018: Ultraviolet to Gamma Ray*, volume 10699, pages 434–455. SPIE.

Zhang, S., Santangelo, A., Feroci, M., Xu, Y., Lu, F., Chen, Y., Feng, H., Zhang, S., Brandt, S., Hernanz, M., *et al.* (2019). The enhanced X-ray Timing and Polarimetry mission—eXTP. *Science China Physics, Mechanics & Astronomy*, **62**, 1–25.

Zhang, S.-N., Li, T., Lu, F., Song, L., Xu, Y., Liu, C., Chen, Y., Cao, X., Bu, Q., Chang, Z., *et al.* (2020). Overview to the hard X-ray modulation telescope (Insight-HXMT) satellite. *Science China Physics, Mechanics & Astronomy*, **63**, 1–18.

Zhao, C., Zhu, B., Zhao, M., Chen, Q., Wang, Z., Zhou, R., and Yang, C. (2021). Development of a modular high-sensitivity high-uniformity gamma camera for radiation monitoring applications. *Nuclear Instruments and Methods in Physics Research Section A: Accelerators, Spectrometers, Detectors and Associated Equipment*, **1003**, 165340.

Zwart, F., Tacken, R., de la Rie, R., Limpens, M., Kochanowski, C., Aitink-Kroes, G., van Baren, C., Bayer, J., Baudin, D., Ceraudo, F., *et al.* (2022). The detector/readout-electronics assembly of the eXTP wide field monitor. In *Space Telescopes and Instrumentation 2022: Ultraviolet to Gamma Ray*, volume 12181, pages 1605–1621. SPIE.